Superconductivity in nanostructures: Andreev billiards and Josephson junction qubits

Marlies Goorden

Superconductivity in nanostructures: Andreev billiards and Josephson junction qubits

PROEFSCHRIFT

ter verkrijging van
de graad van Doctor aan de Universiteit Leiden,
op gezag van de Rector Magnificus Dr. D. D. Breimer,
hoogleraar in de faculteit der Wiskunde en
Natuurwetenschappen en die der Geneeskunde,
volgens besluit van het College voor Promoties
te verdedigen op 15 september 2005
te klokke 15.15 uur

door

Marlies Cornelia Goorden

geboren te Sittard op 26 december 1976

Promotiecommissie:

Promotor:	Prof. dr. C. W. J. Beenakker
Referent:	Prof. dr. ir. W. van Saarloos
Overige leden:	Prof. dr. M. Grifoni
	Prof. dr. Ph. Jacquod
	Prof. dr. P. H. Kes
	Prof. dr. ir. J. E. Mooij
	Dr. P. G. Silvestrov

Het onderzoek beschreven in dit proefschrift is onderdeel van het wetenschappelijke programma van de Stichting voor Fundamenteel Onderzoek der Materie (FOM) en de Nederlandse Organisatie voor Wetenschappelijk Onderzoek (NWO).
The research described in this thesis has been carried out as part of the scientific programme of the Foundation for Fundamental Research on Matter (FOM) and the Netherlands Organisation for Scientific Research (NWO).

I am happy that young physicist like Marlies still do very interesting physics based on this peculiar reflection mechanism.

07.06.05

Alexander V. Andreev

Contents

1 Introduction **1**
- 1.1 Andreev reflection . . . 2
  - 1.1.1 Reflection mechanism . . . 2
  - 1.1.2 Excitation gap . . . 5
  - 1.1.3 Josephson effect . . . 6
- 1.2 Andreev billiard . . . 6
  - 1.2.1 Chaotic vs. integrable billiard . . . 7
  - 1.2.2 Quantum-to-classical crossover . . . 9
- 1.3 Josephson junction qubit . . . 12
- 1.4 This thesis . . . 16

2 Adiabatic quantization of an Andreev billiard **27**
- 2.A Effective RMT . . . 36

3 Quasiclassical fluctuations of the superconductor proximity gap in a chaotic system **45**

4 Quantum-to-classical crossover for Andreev billiards in a magnetic field **57**
- 4.1 Introduction . . . 57
- 4.2 Adiabatic quantization . . . 58
  - 4.2.1 Classical mechanics . . . 58
  - 4.2.2 Adiabatic invariant . . . 60
  - 4.2.3 Quantization . . . 63
  - 4.2.4 Lowest adiabatic level . . . 64
  - 4.2.5 Density of states . . . 66
- 4.3 Effective random-matrix theory . . . 67
  - 4.3.1 Effective cavity . . . 67

4.3.2 Density of states 69
4.4 Comparison with quantum mechanical model 73
4.5 Conclusion 76
4.A Andreev kicked rotator in a magnetic field 78

5 Noiseless scattering states in a chaotic cavity **85**

6 Spectroscopy of a driven solid-state qubit coupled to a structured environment **97**
6.1 Introduction 97
6.2 The driven qubit coupled to a macroscopic detector 100
6.3 Weak coupling: Floquet-Born-Markov master equation 103
6.3.1 Floquet formalism and Floquet-Born-Markovian master equation 103
6.3.2 Van Vleck perturbation theory 105
6.3.3 Line shape of the resonant peak/dip 109
6.3.4 Example: The first blue sideband 109
6.3.5 Results and discussion 113
6.4 Strong coupling: NIBA 114
6.5 Limit $\Omega_p \gg \nu$ 117
6.6 Conclusions 120
6.A Symmetry properties for the dissipative rates for the first blue sideband 121
6.B Coefficients for the kernels $k_0^{\pm}(0)$ 123

Samenvatting **127**

List of publications **131**

Curriculum Vitæ **133**

Dankwoord **135**

Chapter 1

Introduction

Fundamental research on superconductivity can be broadly divided into two classes, each with its own motivation. The first class of research studies novel mechanisms of electron pairing, that might persist at higher temperatures than the conventional phonon-mediated pairing. The second class studies novel effects that occur when conventionally paired electrons are confined to structures of sub-micrometer dimensions (so-called nanostructures). The motivation here is not the search for higher transition temperatures, but the integration of superconducting elements in computer circuits. The research described in this thesis falls in the second class, the study of superconductivity in nanostructures.

Two types of nanostructures have been investigated, *Andreev billiards* and *Josephson junction qubits*. An Andreev billiard is an impurity-free region in a two-dimensional electron gas (a so-called quantum dot), coupled to a superconducting electrode via a point contact. The fundamental question that we have answered is how the excitation gap of the electron gas, caused by Andreev reflection at the superconductor, depends on the Ehrenfest time. This time scale governs the crossover from classical to quantum chaos in quantum dots.

A Josephson junction qubit is a superconducting ring in which the direction of the current is a quantum mechanical superposition of clockwise and counter-clockwise. Such a device is one of the possible building blocks of a quantum computer. To describe existing experiments we have developed a quantitative theory that takes into account both the time-dependent external magnetic field used to control the qubit and its cou-

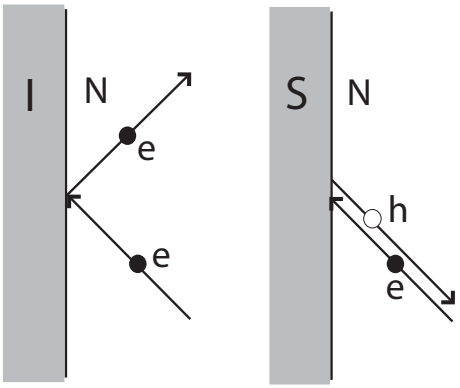

Figure 1.1: Normal reflection (left) vs. Andreev reflection. Upon normal reflection at the interface between an insulator (I) and a normal metal (N) only the component of the velocity normal to the interface changes sign and the charge is conserved. In the case of Andreev reflection at a normal-metal-superconductor (NS) interface all three components of the velocity change sign and the negatively charged electron is converted into a positively charged hole.

pling to a quantum measurement device.

In this introductory chapter we present some background material for the topics studied in the thesis.

1.1 Andreev reflection

The anomalous reflection at the interface between a normal metal (N) and a superconductor (S), discovered by Andreev in 1964 [1], plays a central role in this thesis. Andreev reflection, as this process is now called, explains the opening of an excitation gap in the billiard geometry and it explains the flow of a non-decaying current in the ring geometry (the so-called Josephson effect).

1.1.1 Reflection mechanism

The process of Andreev reflection is illustrated in Fig. 1.1. When a negatively charged electron in the normal metal hits the interface with the su-

perconductor (NS interface) it is converted into a positively charged hole. The hole retraces the path of the electron, so its velocity is reversed (so-called retroreflection). Because the hole has a negative mass, the total momentum is conserved. The charge difference of $2e$ between electron and hole is compensated by the creation of a Cooper pair with charge $2e$ in the superconductor. In contrast, specular reflection between a normal metal and an insulator (also shown in Fig. 1.1) conserves the charge, but not the momentum.

The velocity is only exactly reversed when electron and hole are both at the Fermi level. When the electron has an excitation energy E above the Fermi energy E_F it is converted into a hole with energy $-E$, and as a consequence there is a slight mismatch between their velocities: while the magnitude of the velocity parallel to the superconductor is conserved, the perpendicular velocity differs in magnitude by $\sqrt{4E/m}$.

A quantum mechanical description of Andreev reflection starts from a Schrödinger equation for the electron and hole components $u(\mathbf{r})$ and $v(\mathbf{r})$ of the wave function, coupled by the pair potential $\Delta(\mathbf{r})$. This so-called Bogoliubov-de Gennes (BdG) equation is given by [2]

$$\begin{pmatrix} H_0 & \Delta(\mathbf{r}) \\ \Delta^*(\mathbf{r}) & -H_0^* \end{pmatrix} \begin{pmatrix} u \\ v \end{pmatrix} = E \begin{pmatrix} u \\ v \end{pmatrix}. \tag{1.1}$$

It contains the Hamiltonian $H_0 = [\mathbf{p} + e\mathbf{A}(\mathbf{r})]^2/2m + V(\mathbf{r}) - E_F$ of a single electron moving with momentum $\mathbf{p}$ in an electrostatic potential V and vector potential $\mathbf{A}$. The pair potential $\Delta(\mathbf{r}) \equiv 0$ in the normal region while it recovers the bulk value $\Delta_0 e^{i\phi}$ of the superconductor at some distance l_c away from the interface. For the geometries considered in this thesis the step function

$$\Delta(\mathbf{r}) = \begin{cases} 0 & \text{if } \mathbf{r} \in N \\ \Delta_0 e^{i\phi} & \text{if } \mathbf{r} \in S \end{cases} \tag{1.2}$$

is sufficiently accurate (because l_c is much smaller than the superconducting coherence length $\hbar v_F/\Delta_0$). The excitation spectrum consists of the solution of Eq. (1.1) with $E \geq 0$.

Referring to the geometry of Fig. 1.2 the eigenfunctions of the BdG

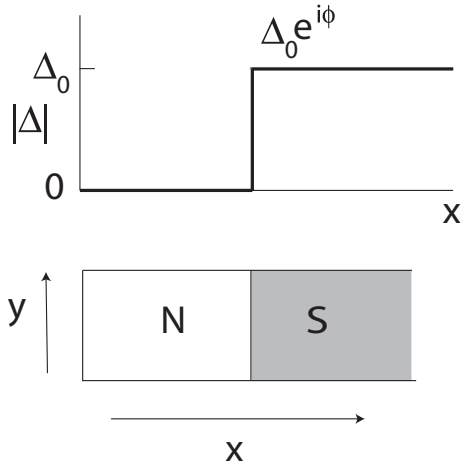

Figure 1.2: Geometry of an NS junction (bottom) and plot of the absolute value of the pair potential (top), in the step function model of Eq. (1.2).

equation in the normal metal can be written as

$$\psi^{\pm}_{n,e} = \begin{pmatrix} 1 \\ 0 \end{pmatrix} \frac{1}{\sqrt{k^e_n}} \Phi_n(y,z) \exp(\pm i k^e_n x), \tag{1.3}$$

$$\psi^{\pm}_{n,h} = \begin{pmatrix} 0 \\ 1 \end{pmatrix} \frac{1}{\sqrt{k^h_n}} \Phi_n(y,z) \exp(\pm i k^h_n x), \tag{1.4}$$

$$k^{e,h}_n = (2m/\hbar^2)^{1/2} (E_F - E_n + \sigma^{e,h} E)^{1/2}, \tag{1.5}$$

with $\sigma^e = 1$ and $\sigma^h = -1$. The discrete wave numbers $k^{e,h}_n$ originate from the confinement in y and z direction, with the index n labeling the different modes. The n-th mode has transverse wave function $\Phi_n(y,z)$ and threshold energy E_n. The wavefunctions are normalized to carry the same amount of quasiparticle current if the functions $\Phi_n(y,z)$ are normalized to unity.

In the superconductor the solutions of the BdG equation give decaying eigenfunctions for $E < \Delta_0$, indicating that there are no propagating modes in the superconductor for these energies. Matching the eigenfunctions in the normal metal and superconductor at the NS boundary determines the scattering at the superconductor. For $\Delta_0 \ll E_F$ and in the absence of a barrier at the NS interface there is no normal reflection, only

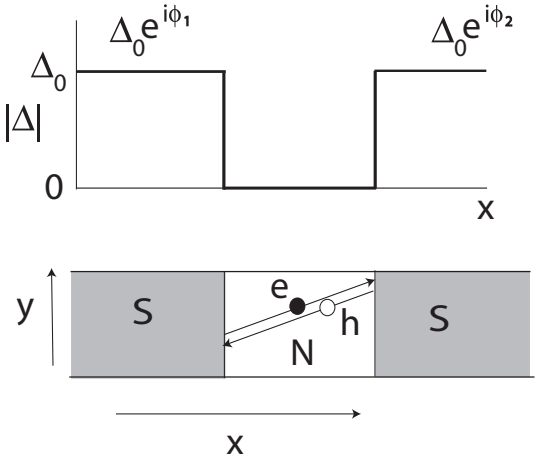

Figure 1.3: Geometry of an SNS junction. The superconducting pair potentials have phase difference $\delta\phi = \phi_1 - \phi_2$. An Andreev level consists of an electron and a hole traveling in opposite directions. This bound state carries a non-zero electrical current.

Andreev reflection. It transforms an electron into a hole without changing the mode index. The transformation is accompanied by a phase shift $-\arccos(E/\Delta_0) \mp \phi$. The factor $-\arccos(E/\Delta_0)$ is due to the penetration of the wavefunction into the superconductor, while the shift $\mp\phi$ is equal to the phase of the pair potential. (The minus sign is for reflection from electron to hole, the plus sign for the reverse process.) Note that this phase shift equals $-\pi/2 \mp \phi$ at the Fermi level.

1.1.2 Excitation gap

Electrons and holes with energies $E < \Delta_0$ cannot leave the normal metal since there are no propagating modes for them in the superconductor. This means that the normal metal has a discrete spectrum for $E < \Delta_0$. The discrete spectrum consists of bound states, called Andreev levels [3, 4]. The lowest Andreev level cannot be at the Fermi level for the following reason: all phase shifts accumulated by the electron in the normal metal are canceled by the Andreev reflected hole, which is its exact time reverse at the Fermi level. What remains is the phase shift of $2\times -\pi/2 = -\pi$ from the penetration of the wavefunction in the superconductor (the phase shifts

$\mp\phi$ cancel as well). So electron and hole interfere destructively at the Fermi level and the lowest excited state must be separated by some energy $E_{\rm gap}$ from E_F. The calculation of $E_{\rm gap}$ is the problem of the Andreev billiard, introduced in Sec. 1.2.

1.1.3 Josephson effect

Now consider an SNS junction having two NS interfaces with a phase difference $\delta\phi = \phi_1 - \phi_2$ of the pair potentials (Fig. 1.3). An Andreev level corresponds to an electron moving towards one superconductor, where it is converted into a hole which goes to the other superconductor to be retroreflected again as an electron.

The excitation gap $E_{\rm gap}$ closes when $\delta\phi = \pi$, because then the electron and hole at the Fermi level interfere constructively rather than destructively (as they do when $\delta\phi = 0$). Not only $E_{\rm gap}$ depends on $\delta\phi$, but the total energy U of the SNS junction is $\delta\phi$-dependent. The current I which flows from one superconductor to the other is related to $U(\delta\phi)$ by

$$I = \frac{2e}{\hbar}\frac{dU}{d\delta\phi}. \tag{1.6}$$

This current is present in the SNS junction in equilibrium, so it cannot decay. Since I depends periodically on $\delta\phi \in (0, 2\pi)$, it reaches a maximum for some $\delta\phi$ at a value called the critical current I_c.

The original discovery by Josephson of this effect [5] was done for the case that the normal metal is a tunnel junction (relevant for our Josephson junction qubit). Then $U = E_J(1 - \cos\delta\phi)$, where $E_J = \pi\Delta_0 G\hbar/4e^2$ [6] is determined by the tunnel conductance G. The current-phase relationship becomes

$$I = I_c \sin\delta\phi, \qquad I_c = \frac{2e}{\hbar}E_J \tag{1.7}$$

The connection between the Josephson effect and Andreev reflection in ballistic SNS junctions was made by Kulik [7].

1.2 Andreev billiard

An electro-micrograph of an Andreev billiard is shown in Fig. 1.4. A confined region in a two-dimensional electron gas is created by means of gate

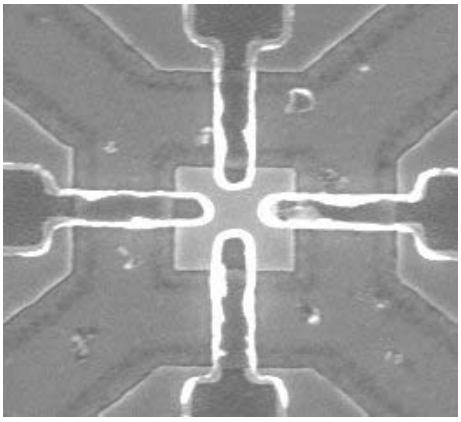

Figure 1.4: Quantum dot (central square of dimensions 500 nm × 500 nm) fabricated in a high-mobility InAs/AlSb heterostructure and contacted by four superconducting Nb electrodes. Device made by A. T. Filip, Groningen University (unpublished figure).

electrodes. These electrodes provide insulating barriers, at which normal specular reflection occurs. Four superconducting electrodes introduce Andreev reflection (retroreflection).

The density of states of two types of Andreev billiards is shown in Fig. 1.5. Depending on the shape, there is either a true excitation gap (solid lines) or a smoothly vanishing density of states without a true gap (dashed lines). The origin of this difference, discovered in Ref. [8], is chaotic vs. integrable dynamics. The density of states could be measured in the Andreev billiard of Fig. 1.4 by means of a scanning tunneling probe, but this experiment has not yet been performed.

1.2.1 Chaotic vs. integrable billiard

Depending on the shape of the billiard, uncoupled from the superconductor, its classical dynamics can be either chaotic or integrable [9–11]. We illustrate the difference for the two billiards in Fig. 1.6. In each billiard we show two trajectories, which are initially very close. In the circularly shaped billiard (left) the trajectories stay close, while in the stadium billiard (right) the two trajectories become very different after only a few collisions with the boundary. This sensitivity on initial conditions is a

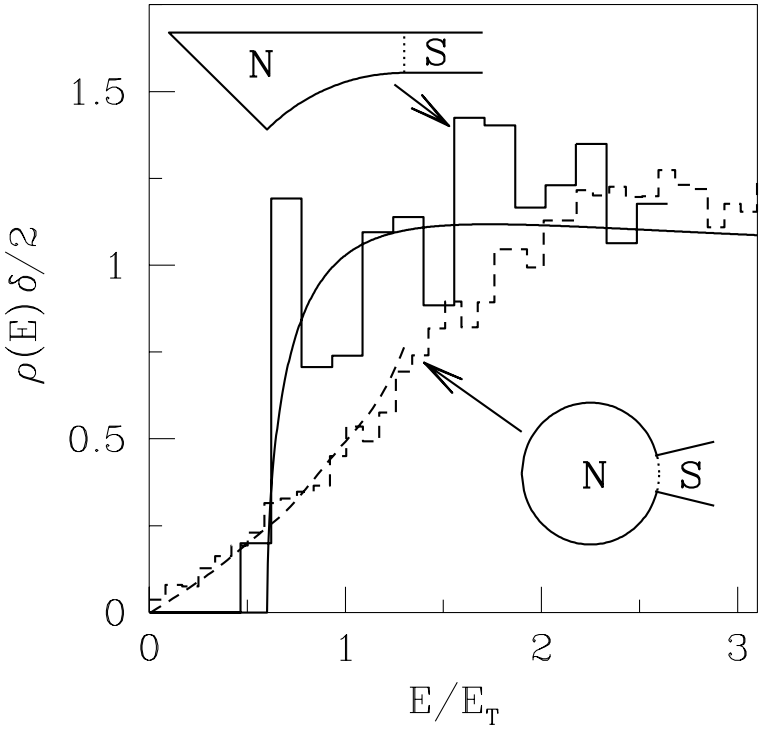

Figure 1.5: Mean density of states for a chaotic Andreev billiard (top inset) and an integrable Andreev billiard (bottom inset). The histograms are the exact quantum mechanical solution, obtained numerically. The smooth curves are the analytical predictions. From Ref. [15].

characteristic of chaotic dynamics: two trajectories which are initially at a distance $\delta(0)$, have diverged to $\delta(t) = \delta(0)\exp(\lambda t)$ after a time t. The Lyapunov exponent λ determines the strength of the divergence.

Quantum mechanical properties of chaotic systems are the subject of the field of quantum chaos [12–14]. A billiard is one of the most simple systems to study in this context. The properties of normal billiards (normal meaning that there is no superconducting segment in the boundary) have been studied extensively in the past. A universal description of chaotic systems is provided by random-matrix theory (RMT) [16], while a direct way of connecting classical and quantum mechanics is provided by periodic orbit theory [10]. The mean density of states of a normal bil-

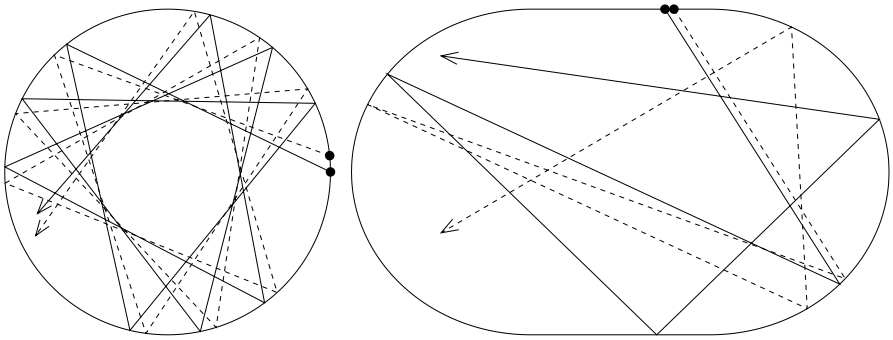

Figure 1.6: Trajectories in an integrable billiard (left) and a chaotic billiard (right). The solid and dashed lines denote two trajectories which are initially very close and either stay close together or diverge.

liard only depends on the area of the billiard, not on its shape, so it can not distinguish between chaotic and integrable dynamics. One needs to study the distribution of level spacings, rather than the mean spacing, to find quantum signatures of chaos. In an Andreev billiard, however, the mean density of states itself is already different for chaotic and integrable normal regions, cf. Fig. 1.5.

The origin of the difference is the absence of long dwell times in the chaotic billiard. The chaotic dynamics mixes the trajectories so well that the mean dwell time τ_D is representative of the actual dwell time of most electrons. A hard gap appears at [8]

$$E_{\rm gap} = \gamma^{5/2}\hbar/\tau_D \approx 0.3\,\hbar/\tau_D, \tag{1.8}$$

with $\gamma = \frac{1}{2}(\sqrt{5}-1)$ the golden number. In an integrable billiard, in contrast, the distribution of dwell times has a long tail, so that dwell times $\gg \tau_D$ have a substantial weight. These almost trapped electrons contribute to the spectral density at low energies, leading to a density of states vanishing with a power-law rather than a hard gap.

1.2.2 Quantum-to-classical crossover

In this thesis we consider chaotic billiards. As mentioned in the previous subsection, two methods to study the properties of chaotic billiards are

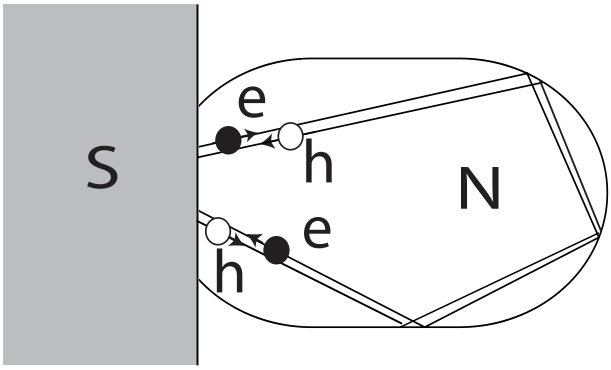

Figure 1.7: Periodic trajectory in an Andreev billiard consisting of an electron (e) and a retroreflected hole (h).

RMT and periodic orbit theory. RMT is based on the fact that the Hamiltonian of a chaotic system is well-described by a large Hermitian matrix with randomly chosen elements. The distribution of the matrix elements is usually taken to be a set of independent Gaussians, but the results are largely insensitive to the distribution if the matrix is large enough. RMT has been very successful in describing the properties of chaotic quantum dots [17, 18]. The spectrum of an Andreev billiard was calculated using RMT in Ref. [8]. RMT predicts a hard gap (1.8) in the mean density of states of the Andreev billiard, meaning that $\rho(E) = 0$ for $E < E_{\rm gap}$.

A closer connection to the classical dynamics is provided by periodic orbit theory. The retroreflection at the superconductor makes all trajectories in the Andreev billiard periodic near the Fermi level [19]. A periodic trajectory consists of an electron and a hole retracing each other's path (see Fig. 1.7). The phase accumulated in one period consists of two parts: the phase shifts of the two Andreev reflections, equal to $-\pi$ (for $E \ll \Delta_0$) and the phase $2ET$ acquired during the motion in the normal region. (The period of the trajectory is $2T$, with T the time between Andreev reflections, also referred to as the dwell time.) Summing the two phase contributions and requiring that the phase accumulated in one period is a multiple of 2π leads to the mean density of states

$$\rho_{\rm BS}(E) = N \int_0^\infty dT P(T) \sum_{n=0}^{\infty} \delta\left(E - (n + \frac{1}{2})\pi\hbar/T\right), \tag{1.9}$$

where $P(T)$ is the classical dwell time distribution and N is the number of modes in the point contact connecting the normal region with the superconductor. This result is the Bohr-Sommerfeld approximation of Ref. [8].

A chaotic billiard has an exponential dwell time distribution $P(T) = \exp(-T/\tau_D)\tau_D^{-1}$, with $\tau_D = 2\pi\hbar/N\delta$ the mean dwell time and δ the mean level spacing of the isolated billiard. Substitution of this distribution into Eq. (1.9) results in the density of states [20]

$$\rho_{\rm BS}(E) = \frac{2}{\delta}\frac{(\pi E_T/E)^2\cosh(\pi E_T/E)}{\sinh^2(\pi E_T/E)}, \tag{1.10}$$

with Thouless energy $E_T = \hbar/2\tau_D$. The Bohr-Sommerfeld density of states is compared with the RMT result in Fig. 1.8. In contrast to RMT, periodic orbit theory does not predict a hard gap in the density of states, although there is an exponential suppression for $E \ll E_T$. It was realized by Lodder and Nazarov [21] that the discrepancy between the two theories of Refs. [8] and [20] is not a short-coming in one of them, but indicates that both theories are correct in different limits. To explain this, the concept of the Ehrenfest time is needed.

The Ehrenfest time characterizes the crossover from classical to quantum mechanics. According to Ehrenfest's theorem [22] the propagation of a quantum mechanical wave packet is initially described by the classical equations of motion. If the classical motion is chaotic, the size of the wave packet will grow exponentially $\propto \exp(\lambda t)$. After some time the initial size λ_F (Fermi wavelength) of the wave packet has increased to the linear dimension L of the quantum dot. This time scale is the Ehrenfest time

$$\tau_E = \frac{1}{\lambda}\left[\ln(L/\lambda_F) + \mathcal{O}(1)\right]. \tag{1.11}$$

For times $t > \tau_E$ a description in terms of classical trajectories no longer applies.

Periodic orbit theory, since it is based on classical trajectories, requires a mean dwell time $\tau_D \ll \tau_E$. The Bohr-Sommerfeld result therefore applies in the limit $\tau_E/\tau_D \to \infty$. In the opposite limit $\tau_E/\tau_D \to 0$ the RMT result applies, with a hard gap given by Eq. (1.8), of order $\hbar/\tau_D$. For finite $\tau_E \gg \tau_D$ a hard gap appears at a value of order $\hbar/\tau_E$ [21].

The central result of this thesis is a quasiclassical theory which describes the crossover from the RMT regime $\tau_D \gg \tau_E$ to the periodic orbit

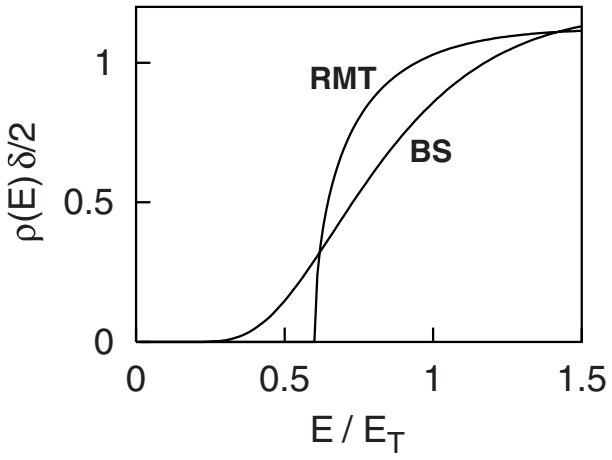

Figure 1.8: Comparison of the mean density of states $\rho(E)$ of a chaotic Andreev billiard, as it is predicted by random-matrix theory (RMT) and by periodic orbit theory (or Bohr-Sommerfeld quantization, labeled BS). While RMT (valid for $\tau_E \ll \tau_D$) predicts a hard gap, Bohr-Sommerfeld quantization (valid in the opposite limit $\tau_E \gg \tau_D$) gives an exponential suppression at low energies, without a hard gap. From Ref. [23].

regime $\tau_D \ll \tau_E$. Our approach is very simple in principle: for short classical trajectories $T < \tau_E$ we use periodic orbit theory while for long classical trajectories $T > \tau_E$ we use RMT with effective τ_E-dependent parameters (effective RMT). Since an experimental test is still lacking, we compare our theory with quantum mechanical simulations. The numerical model we use is the Andreev kicked rotator [24], which provides a stroboscopic description of an Andreev billiard. The model is very efficient and allows one to go to large enough system sizes to reach the regime $\tau_E \gtrsim \tau_D$.

1.3 Josephson junction qubit

Superconducting circuits with Josephson junctions can be designed to have states that carry circulating currents of opposite sign. This means that quantum mechanically the system can be in a macroscopic superposition of clockwise and counter-clockwise circulating currents [25]. The word “macroscopic” is used because a macroscopic number of Cooper

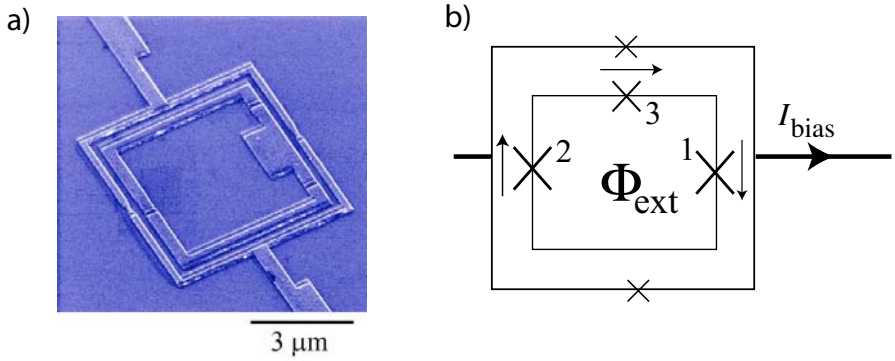

Figure 1.9: a). Scanning electron microscope image of the Josephson junction qubit. b). Schematic picture of the Josephson junction qubit (inner loop). The Josephson junctions are denoted by crosses and the arrows indicate the direction of the phase difference $\delta\phi_i$ in Eq. (1.12). Junction 3 has a critical current which is smaller by a factor α. The loop is inductively coupled to a Superconductor Quantum Interference Device (SQUID) (outer loop), which can be used as a magnetometer. From Ref. [36].

pairs is involved in a state. The interest in the quantum mechanical behaviour of these systems is motivated by the possibility of using them as the building blocks of a quantum computer [26–28]. While a classical computer has bits which are either 0 or 1, a quantum computer has quantum bits (qubits) which can be in superpositions of the states $|0\rangle$ and $|1\rangle$. The laws of quantum mechanics allow quantum computers to outperform classical computers for some tasks. Josephson junction circuits are promising candidates for realizing a quantum computer, because the technology to expand such systems to large-scale computers already exists. However, Josephson junction circuits are large on the scale of single atoms and are therefore hard to decouple from experimental noise. The coherent manipulation of only one qubit is already a huge experimental challenge, but there exist several superconducting Josephson circuits where it was achieved [29–34]. In this thesis we focus on one particular realization: a superconducting loop intersected by three Josephson junctions [35], shown in Fig. 1.9.

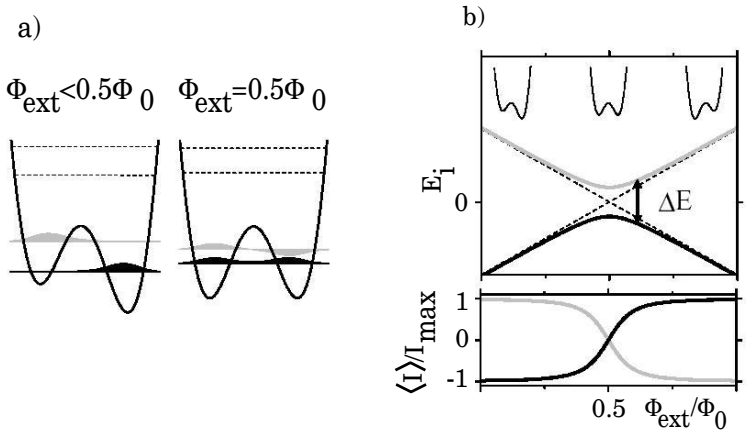

Figure 1.10: a). Schematical picture of the loop's double well potential for an applied flux $\Phi_{\text{ext}} \approx 0.5\Phi_0$. The quantum mechanical ground state and first excited state are shown, they are well separated from the higher levels (dotted lines). b). Energy and expectation value of the current as a function of the applied flux Φ_{ext} for the ground and first excited state. From Ref. [36].

The Josephson junctions are characterized by two energy scales: the Josephson energy E_J and the charging energy $E_C = e^2/2C$, where C is the capacitance of the Josephson junction. The three Josephson junctions divide the superconducting loop into islands. The phase (hence current) and the excess number of Cooper pairs on each island are quantum mechanical conjugate variables. Depending on the ratio E_J/E_C it is convenient to choose a basis where the charge (in the limit $E_J \ll E_C$) or the current (in the opposite limit $E_J \gg E_C$) is well defined. In the system shown in Fig. 1.9 $E_J/E_C \simeq 60$ and the eigenstates can be well described as superpositions of current states.

A description of the system starts with the current-phase relationship (1.7) of a Josephson junction. One of the three junctions in Fig. 1.9 has a critical current which is smaller by a factor α. The loop can be biased by an external magnetic field Φ_{ext}. The inductance of the loop is negligible, so the total flux is the external flux. Then flux quantization [6] requires that $\delta\phi_1 + \delta\phi_2 + \delta\phi_3 = 2\pi\Phi_{\text{ext}}/\Phi_0$. Here $\Phi_0 = h/2e$ is the superconducting flux quantum. The Josephson energy due to the i-th junction reads $E_{Ji}(1-$

$\cos\delta\phi_i$). Combining this with the flux quantization, the total Josephson energy U is given by

$$U = E_J\left[2+\alpha-\cos\delta\phi_1-\cos\delta\phi_2-\alpha\cos(2\pi\Phi_{\text{ext}}/\Phi_0-\delta\phi_1-\delta\phi_2)\right]. \tag{1.12}$$

It is a function of two phases. For a range of magnetic fields, this classical potential has two stable solutions: one corresponding to a current flowing clockwise, the other to a current flowing counter-clockwise. The magnitude I_{max} of both currents is equal and it is very close to the critical current of the weakest junction. By adding the charging energy and considering the circuit quantum mechanically, the quantum mechanical eigenstates can be determined [37]. For suitably chosen parameters ($\alpha \simeq 0.6-0.8, E_J/E_C \simeq 60$), the system can be well-described as a two-state quantum system, in the vicinity of $\Phi_{\text{ext}} = \frac{1}{2}\Phi_0$. The two eigenstates correspond to superpositions of states with opposite currents.

This is illustrated in Fig. 1.10. The classical double-well potential is shown, with the wells corresponding to currents of opposite sign. Quantum mechanically the qubit has two low-energy eigenstates (black and gray) which are well-separated from the higher lying levels. For $\Phi_{\text{ext}} = \frac{1}{2}\Phi_0$ the energies of the two wells are equal and the quantum mechanical states are symmetric and anti-symmetric superpositions of the two current states. For Φ_{ext} below or above $\frac{1}{2}\Phi_0$ the quantum states are more localized in one of the two wells. In Fig. 1.10 the expectation value of the current as a function of Φ_{ext} is also shown, both for the ground and excited state. The current produces a magnetic field, which can be detected by a Superconducting Quantum Interference Device (SQUID), shown in Fig. 1.9.

The Hamiltonian of the Josephson junction qubit can be written in the form of a spin $1/2$ particle,

$$H_Q = -\frac{\hbar W}{2}\sigma_x - \frac{\hbar F}{2}\sigma_z\,, \tag{1.13}$$

where σ_i are Pauli matrices. The tunnel splitting $\hbar W$ depends on the details of the junctions and it cannot be manipulated during the experiment. The static energy bias $\hbar F = 2I_{\text{max}}\left(\Phi_{\text{ext}} - \frac{1}{2}\Phi_0\right)$ can be tuned by changing the applied flux.

The state of the qubit can be controlled by applying a time-dependent magnetic field in the GHz range, introducing a time dependence in the

energy bias F. If the control field is resonant with the energy splitting of the ground and excited state, coherent oscillations between the two levels occur. These Rabi oscillations have been measured [33]. For a quantitative description of the experiment one has to take into account the presence of the quantum measurement device (the SQUID) and the fact that the system is periodically driven. In a recent experiment it has been found that the presence of the SQUID introduces extra resonances [38]. The last chapter of the thesis is devoted to a quantitative description of this experiment.

1.4 This thesis

Chapter 2: Adiabatic quantization of an Andreev billiard

Periodic orbit theory gives a reliable description of the energy levels and wave functions of a normal billiard, provided it is large compared to the electron wave length. In this chapter we apply this quasiclassical approach to Andreev billiards.

We start by studying the classical dynamics of electrons and holes. For finite excitation energies an Andreev reflected hole does not exactly retrace the path of the electron. The slow drift has an adiabatic invariant: the time T between Andreev reflections. The adiabatically invariant torus in phase space can be quantized, resulting in a ladder of Andreev levels. The adiabatic quantization breaks down for $T > \tau_E$. For this part of phase space we propose an effective RMT. The result is a quantitative prediction for the dependence of the excitation gap on the Ehrenfest time τ_E and the dwell time τ_D, which agrees well with computer simulations [24].

Chapter 3: Quasiclassical fluctuations of the superconductor proximity gap in a chaotic system

Mesoscopic systems have universal sample-to-sample fluctuations. Universal means that their size does not depend on the exact miscroscopic properties of the system. A well-known example are the universal conductance fluctuations, which occur both in disordered and chaotic ballistic systems. They can be described by RMT.

In this chapter we focus on the sample-to-sample fluctuations in the excitation gap of the Andreev billiard. In Ref. [39] the universal distribution

function of the gap is calculated using RMT. It has a standard deviation

$$\delta E_0^{\mathrm{RMT}} = 1.09\, E_T/N^{2/3}. \tag{1.14}$$

For $\tau_E \gtrsim \tau_D$ RMT breaks down. Since the Ehrenfest time scales only logarithmically with L/λ_F, a numerical investigation of the regime $\tau_E \gtrsim \tau_D$ demands a very effective numerical model. This is provided by the Andreev kicked rotator [24].

We use the Andreev kicked rotator to investigate the effect of the Ehrenfest time on the gap fluctuations. We find that in the quasiclasscial regime, the amplitude of the fluctuations is much larger than the RMT value (1.14). The effective RMT of chapter 2 gives a good description of the fluctuations.

Chapter 4: Quantum-to-classical crossover of Andreev billiards in a magnetic field

We continue our development of the periodic orbit theory of Andreev billiards by studying the effect of a perpendicular magnetic field. RMT predicts that the excitation gap of the Andreev billiard will be reduced with increasing field strength and that it will close at a critical magnetic field [15]

$$B_0 \simeq \frac{\hbar}{eL^2}\sqrt{\frac{L}{v_F \tau_D}}. \tag{1.15}$$

We extend the quasiclassical theory of chapter 2 to include a time-reversal-symmetry breaking magnetic field. The critical magnetic field is reduced with increasing τ_E. We compare our quasiclassical expressions with numerical results from the Andreev kicked rotator.

Chapter 5: Noiseless scattering states in a chaotic cavity

In this chapter we apply the effective RMT, developed in chapter 2 for the Andreev billiard to a different system: a quantum dot which is not attached to a superconductor, but to two electron reservoirs. Through such a system a current $I(t)$ can flow. Due to the discreteness of charge the current will fluctuate around its time averaged value $\bar{I}$, even for zero temperature. These fluctuations are known as shot noise. The shot noise

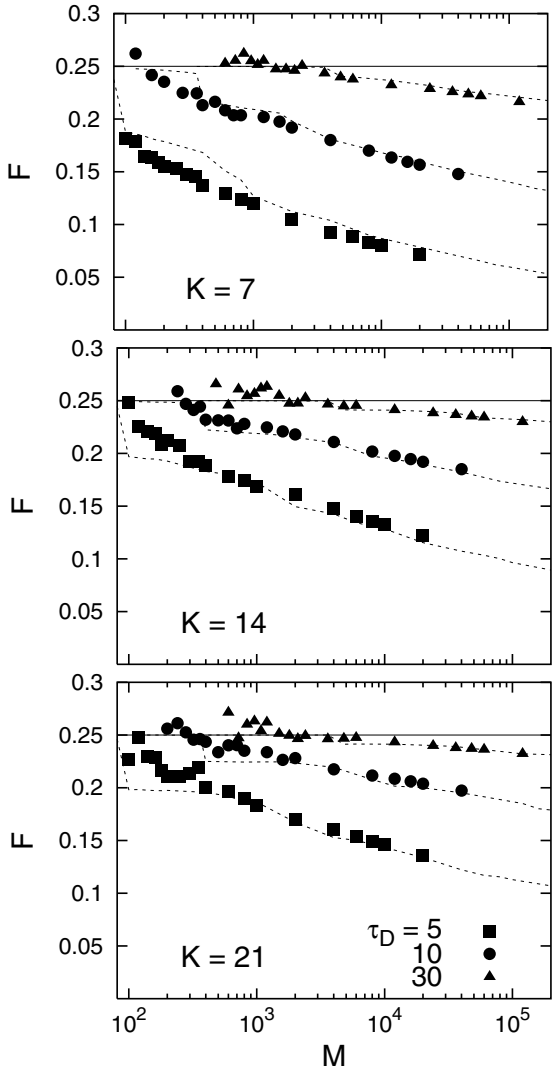

Figure 1.11: Dependence of the Fano factor F on the dimensionality of Hilbert space $M \simeq L/\lambda_F$, at fixed dwell time $\tau_D = (M/2N) \times \tau_0$. The data points are from a quantum mechanical simulation of the open kicked rotator with kicking strength K, Lyapunov exponent $\lambda \simeq \ln(K/2)$ and stroboscopic time τ_0. The dashed lines are the prediction from effective RMT. There are no fit parameters in the comparison. From Ref. [43].

power S can be quantified by the Fano factor $F = S/2e\bar{I}$. For a quantum dot RMT predicts the universal value $F = 1/4$ [40].

In the limit $L/\lambda_F \to \infty$ it was predicted that shot noise should vanish, due to the transition from stochastic wave dynamics to deterministic particle dynamics [41]. A more quantitative description was given in Ref. [42] and yields an exponential suppression of the Fano factor,

$$F = \frac{1}{4}\exp(-\tau_E/\tau_D). \tag{1.16}$$

The theory of Ref. [42] does not describe sample-specific deviations from the universal value. In this chapter we construct noiseless channels for transport through a chaotic quantum dot and relate the Fano factor to the classical details of the system. The noisy channels are described by effective RMT. We find qualitatively the same behaviour as predicted by Eq. (1.16), but we find that the suppression depends on the difference between τ_E and the ergodic time $\tau_{\rm erg}$, not on τ_E alone. The sample-specific results predicted by our theory agree well with computer simulations, as shown in Fig. 1.11.

Chapter 6: Spectroscopy of a driven solid-state qubit coupled to a structured environment

It is not realistic to describe a macroscopic quantum system as being completely isolated from its surroundings. In reality, the quantum system is an open system in contact with a heat bath. The most widely-used model for the bath is a thermal reservoir consisting of many uncoupled harmonic oscillators. It is assumed that the coupling between system and bath is linear in both the system and bath coordinates. When the quantum system is a two-state system, described by a spin $1/2$ Hamiltonian, this model is known as the spin-boson model [44].

The influence of the heat bath on the quantum system can be completely described by its spectral density $J(\omega)$. The linear form $J(\omega) \propto \omega$ represents the effect of an Ohmic electromagnetic environment. When the environment is a quantum measurement device, the simple Ohmic description is not always valid. In the experiment of the Josephson junction qubit the measurement device is a SQUID, shunted by an external capacitance. It can be modeled as a harmonic oscillator with frequency Ω_p. The whole

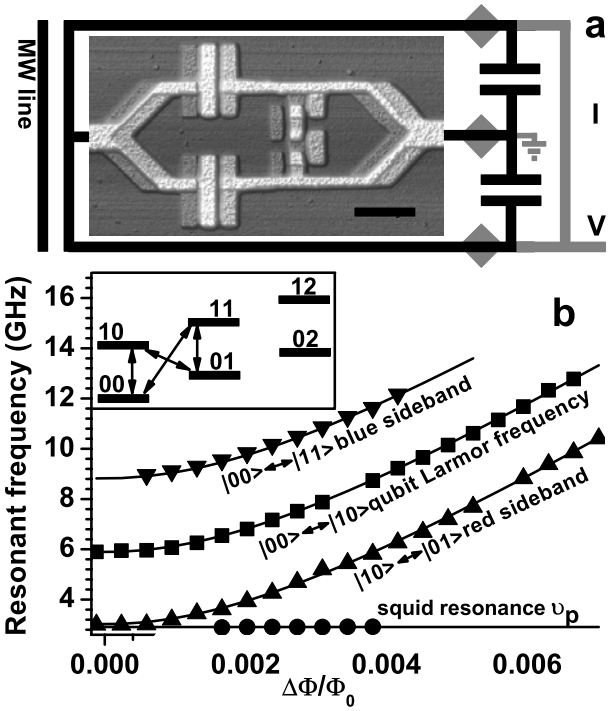

Figure 1.12: a). Josephson junction qubit (small loop on the right hand side) coupled to a SQUID (total loop), shunted by a capacitance. The qubit-SQUID coupling is realized by merging the two loops (different from the inductive coupling of Fig. 1.9). The time-dependent control field is provided by the MW (=microwave) line and couples inductively to the qubit. b). Resonant frequencies in the coupled qubit-SQUID system as a function of the bias $\Delta\Phi = \Phi_{\rm ext} - \frac{1}{2}\Phi_0$. Different symbols correspond to different transitions, shown in the inset. The states in the inset are described by two numbers, the first number characterizes the qubit state, while the second number refers to the state of the capacitively shunted SQUID. The solid lines are numerical fits. From Ref. [38].

set-up can be described as a qubit coupled to a heat bath, having a spectral density with a Lorentzian peak at Ω_p [45]. An equivalent description is that of a qubit coupled to a harmonic oscillator which itself is damped by an Ohmic heat bath.

In the experiment of Ref. [38], the coupled dynamics in the qubit-

oscillator system was investigated (cf. Fig. 1.12). In this chapter we give a quantitative description of the behaviour of the system, both in the experimentally relevant weak damping limit and in the limit of strong damping and/or high temperature. We find that the combination of the coupling to the SQUID and the time-dependent control field results in resonances in the long-time behaviour of the qubit, in agreement with the experiment. We give analytical formulas for their line-shapes. They compare well with the results of a numerical ab-initio calculation.

Bibliography

[1] A. F. Andreev, Zh. Eksp. Teor. Fiz. **46**, 1823 (1964) [Sov. Phys. JETP **19**, 1228 (1964)].

[2] P. G. de Gennes, *Superconductivity of Metals and Alloys* (Benjamin, New York, 1966).

[3] Y. Imry, *Introduction to Mesoscopic Physics* (Oxford University Press, Oxford, 1997).

[4] B. J. van Wees and H. Takayanagi, in *Mesoscopic Electron Transport*, edited by L. L. Sohn, L. P. Kouwenhoven, and G. Schön, NATO ASI Series E345 (Kluwer, Dordrecht, 1997).

[5] B. D. Josephson, Phys. Lett. **1**, 251 (1962).

[6] M. Tinkham, *Introduction to Superconductivity* (McGraw-Hill, New York, 1996).

[7] I. O. Kulik, Zh. Eksp. Teor. Fiz. **57**, 1745 (1969) [Sov. Phys. JETP **30**, 944 (1970)].

[8] J. A. Melsen, P. W. Brouwer, K. M. Frahm, and C. W. J. Beenakker, Europhys. Lett. **35**, 7 (1996).

[9] A. J. Lichtenberg and M. A. Lieberman, *Regular and Chaotic Dynamics* (Springer, New York, 1983).

[10] M. C. Gutzwiller, *Chaos in Classical and Quantum Mechanics* (Springer, Berlin, 1990).

[11] E. Ott, *Chaos in Dynamical Systems* (Cambridge University Press, Cambridge, 1993).

[12] G. Casati and B. V. Chirikov, *Quantum Chaos* (Cambridge University Press, Cambridge, 1995).

[13] H. -J. Stöckmann, *Quantum Chaos, An Introduction* (Cambridge University Press, Cambridge, 1999).

[14] F. Haake, *Quantum Signatures of Chaos* (Springer, Berlin, 2001).

[15] J. A. Melsen, P. W. Brouwer, K. M. Frahm, and C. W. J. Beenakker, Physica Scripta **T69**, 223 (1997).

[16] M. L. Mehta, *Random Matrices* (Academic Press, New York, 1991).

[17] C. W. J. Beenakker, Rev. Mod. Phys. **69**, 731 (1997).

[18] T. Guhr, A. Müller-Groeling, and H. A. Weidenmüller, Phys. Rep. **299**, 189 (1998).

[19] I. Kosztin, D. L. Maslov, and P. M. Goldbart, Phys. Rev. Lett. **75**, 1735 (1995).

[20] H. Schomerus and C. W. J. Beenakker, Phys. Rev. Lett. **82**, 2951 (1999).

[21] A. Lodder and Yu. V. Nazarov, Phys. Rev. B **58**, 5783 (1998).

[22] P. Ehrenfest, Z. Phys. **45**, 455 (1927).

[23] C. W. J. Beenakker, Lect. Notes Phys. **667**, 131 (2005); cond-mat/0406018.

[24] Ph. Jacquod, H. Schomerus, and C. W. J. Beenakker, Phys. Rev. Lett. **90**, 207004 (2003).

[25] A. J. Leggett and A. Garg, Phys. Rev. Lett. **54**, 857 (1985).

[26] M. A. Nielsen and I. L. Chuang, *Quantum Computation and Quantum Information* (Cambridge University Press, Cambridge, 2000).

[27] D. P. DiVincenzo, in *Mesoscopic Electron Transport*, edited by L. L. Sohn, L. P. Kouwenhoven, and G. Schön, NATO ASI Series E345 (Kluwer, Dordrecht, 1997); quant-ph/0002077.

[28] Y. Makhlin, G. Schön, and A. Shnirman, Rev. Mod. Phys. **73**, 357 (2001).

[29] Y. Nakamura, Yu. A. Pashkin, and J. S. Tsai, Nature **398**, 786 (1999).

[30] D. Vion, A. Aassime, A. Cottet, P. Joyez, H. Pothier, C. Urbina, D. Esteve, and M. H. Devoret, Science **296**, 886 (2002).

[31] Y. Yu, S. Y. Han, X. Chu, S. I. Chu, and Z. Wang, Science **296**, 889 (2002).

[32] J. M. Martinis, S. Nam, J. Aumentado, and C. Urbina, Phys. Rev. Lett. **89**, 117901 (2002).

[33] I. Chiorescu, Y. Nakamura, C. J. P. M. Harmans, and J. E Mooij, Science **299**, 1869 (2003).

[34] T. Duty, D. Gunnarsson, K. Bladh, and P. Delsing, Phys. Rev. B **69**, 140503(R) (2004).

[35] J. E. Mooij, T. P. Orlando, L. S. Levitov, L. Tian, C. H. van der Wal, and S. Lloyd, Science **285**, 1036 (1999).

[36] C. H. van der Wal, Ph. D. thesis (2001).

[37] T. P. Orlando, J. E. Mooij, L. Tian, C. H. van der Wal, L. S. Levitov, S. Lloyd, and J. J. Mazo, Phys. Rev. B **60**, 15398 (1999).

[38] I. Chiorescu, P. Bertet, K. Semba, Y. Nakamura, C. J. P. M. Harmans, and J. E. Mooij, Nature **431**, 159 (2004).

[39] M. G. Vavilov, P. W. Brouwer, V. Ambegaokar, and C. W. J. Beenakker, Phys. Rev. Lett. **86**, 874 (2001).

[40] R. A. Jalabert, J.-L. Pichard, and C. W. J. Beenakker, Europhys. Lett. **27**, 255 (1994).

[41] C. W. J. Beenakker and H. van Houten, Phys. Rev. B **43**, 12066 (1991).

[42] O. Agam, I. Aleiner, and A. Larkin, Phys. Rev. Lett. **85**, 3153 (2000).

[43] J. Tworzydło, A. Tajic, H. Schomerus, and C. W. J. Beenakker, Phys. Rev. B **68**, 115313 (2003).

[44] U. Weiss, *Quantum Dissipative Systems* (World Scienific, Singapore, 1999).

[45] L. Tian, S. Lloyd, and T. P. Orlando, Phys. Rev. B **65**, 144516 (2002).

Chapter 2

Adiabatic quantization of an Andreev billiard

The notion that quantized energy levels may be associated with classical adiabatic invariants goes back to Ehrenfest and the birth of quantum mechanics [1]. It was successful in providing a semiclassical quantization scheme for special integrable dynamical systems, but failed to describe the generic nonintegrable case. Adiabatic invariants play an interesting but minor role in the quantization of chaotic systems [2, 3].

Since the existence of an adiabatic invariant is the exception rather than the rule, the emergence of a new one quite often teaches us something useful about the system. An example from condensed matter physics is the quantum Hall effect, in which the semiclassical theory is based on two adiabatic invariants: the flux through a cyclotron orbit and the flux enclosed by the orbit center as it slowly drifts along an equipotential [4]. The strong magnetic field suppresses chaotic dynamics in a smooth potential landscape, rendering the motion quasi-integrable.

Some time ago it was realized that Andreev reflection has a similar effect on the chaotic motion in an electron billiard coupled to a superconductor [5]. An electron trajectory is retraced by the hole that is produced upon absorption of a Cooper pair by the superconductor. At the Fermi energy E_F the dynamics of the hole is precisely the time reverse of the electron dynamics, so that the motion is strictly periodic. The period from electron to hole and back to electron is twice the time T between Andreev reflections. For finite excitation energy E the electron (at energy $E_F + E$)

and the hole (at energy $E_F - E$) follow slightly different trajectories, so the orbit does not quite close and drifts around in phase space. This drift has been studied in a variety of contexts [5–9], but not in connection with adiabatic invariants and the associated quantization conditions. It is the purpose of this chapter to make that connection and point out a striking physical consequence: The wave functions of adiabatically quantized Andreev levels fill the cavity in a highly nonuniform "squeezed" way, which has no counterpart in normal state chaotic or regular billiards. In particular the squeezing is distinct from periodic orbit scarring [10] and entirely different from the random superposition of plane waves expected for a fully chaotic billiard [11].

Adiabatic quantization breaks down near the excitation gap, and we will argue that random-matrix theory [12] can be used to quantize the lowest-lying excitations above the gap. This will lead us to a formula for the gap that crosses over from the Thouless energy to the inverse Ehrenfest time as the number of modes in the point contact is increased.

To illustrate the problem we represent in Figs. 2.1 and 2.2 the quasiperiodic motion in a particular Andreev billiard. (It is similar to a Sinai billiard, but has a smooth potential V in the interior to favor adiabaticity.) Figure 2.1 shows a trajectory in real space while Fig. 2.2 is a section of phase space at the interface with the superconductor ($y = 0$). The tangential component p_x of the electron momentum is plotted as a function of the coordinate x along the interface. Each point in this Poincaré map corresponds to one collision of an electron with the interface. (The collisions of holes are not plotted.) The electron is retroreflected as a hole with the same p_x. At $E = 0$ the component p_y is also the same, and so the hole retraces the path of the electron (the hole velocity being opposite to its momentum). At non-zero E the retroreflection occurs with a slight change in p_y, because of the difference $2E$ in the kinetic energy of electrons and holes. The resulting slow drift of the periodic trajectory traces out a contour in the surface of section. The adiabatic invariant is the function of x, p_x that is constant on the contour. We have found numerically that the drift follows *isochronous* contours C_T of constant time $T(x, p_x)$ between Andreev reflections [13]. Let us now demonstrate analytically that T is an adiabatic invariant.

We consider the Poincaré map $C_T \to C(E, T)$ at energy E. If $E = 0$ the Poincaré map is the identity, so $C(0, T) = C_T$. For adiabatic invariance

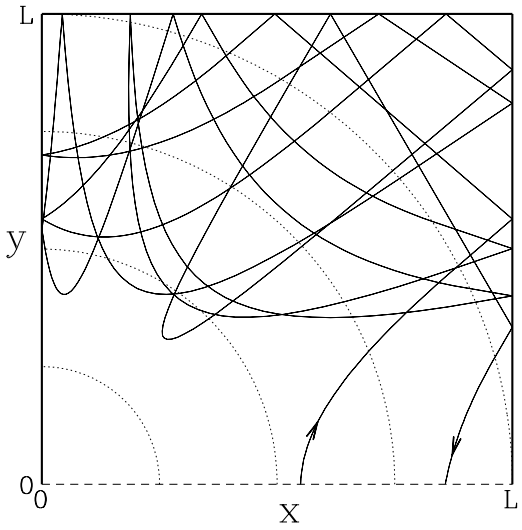

Figure 2.1: Classical trajectory in an Andreev billiard. Particles in a two-dimensional electron gas are deflected by the potential $V = [1-(r/L)^2]V_0$ for $r < L$, $V = 0$ for $r > L$. (The dotted circles are equipotentials.) There is specular reflection at the boundaries with an insulator (thick solid lines) and Andreev reflection at the boundary with a superconductor (dashed line). The trajectory follows the motion between two Andreev reflections of an electron near the Fermi energy $E_F = 0.84\,V_0$. The Andreev reflected hole retraces this trajectory in opposite direction.

we need to prove that $\lim_{E\to 0} dC/dE = 0$, so that the difference between $C(E,T)$ and C_T is of higher order than E [14]. Since the contour $C(E,T)$ can be locally represented by a function $p_x(x,E)$, we need to prove that $\lim_{E\to 0} \partial p_x(x,E)/\partial E = 0$.

In order to prove this, it is convenient to decompose the map $C_T \to C(E,T)$ into three separate stages, starting out as an electron (from C_T to C_+), followed by Andreev reflection ($C_+ \to C_-$), and then concluded as a hole [from C_- to $C(E,T)$]. Andreev reflection introduces a discontinuity in p_y but leaves p_x unchanged, so $C_+ = C_-$. The flow in phase space as electron (+) or hole (−) at energy E is described by the action $S_\pm(\mathbf{q},E)$, such that $\mathbf{p}^\pm(\mathbf{q},E) = \partial S_\pm/\partial\mathbf{q}$ gives the local dependence of (electron or hole)

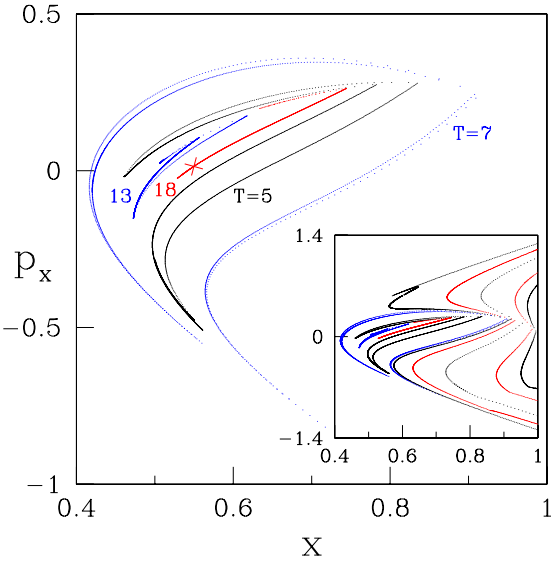

Figure 2.2: Poincaré map for the Andreev billiard of Fig. 2.1. Each dot represents a starting point of an electron trajectory, at position x (in units of L) along the interface $y = 0$ and with tangential momentum p_x (in units of $\sqrt{mV_0}$). The inset shows the full surface of section, while the main plot is an enlargement of the central region. The drifting quasiperiodic motion follows contours of constant time T between Andreev reflections. The cross marks the starting point of the trajectory shown in the previous figure, having $T = 18$ (in units of $\sqrt{mL^2/V_0}$).

momentum $\mathbf{p} = (p_x, p_y)$ on position $\mathbf{q} = (x, y)$. The derivative $\partial S_\pm/\partial E = t_\pm(\mathbf{q}, E)$ is the time elapsed since the previous Andreev reflection. Since by construction $t_\pm(x, y = 0, E = 0) = T$ is independent of the position x of the end of the trajectory, we find that $\lim_{E\to 0} \partial p_x^\pm(x, y = 0, E)/\partial E = 0$, completing the proof.

The drift $(\delta x, \delta p_x)$ of a point in the Poincaré map is perpendicular to the vector $(\partial T/\partial x, \partial T/\partial p_x)$. Using also that the map is area preserving, it follows that

$$(\delta x, \delta p_x) = Ef(T)(\partial T/\partial p_x, -\partial T/\partial x) + \mathcal{O}(E^2), \tag{2.1}$$

with a prefactor $f(T)$ that is the same along the entire contour.

The adiabatic invariance of isochronous contours may alternatively be obtained from the adiabatic invariance of the action integral I over the quasiperiodic motion from electron to hole and back to electron:

$$I = \oint p dq = E \oint \frac{dq}{\dot{q}} = 2ET. \tag{2.2}$$

Since E is a constant of the motion, adiabatic invariance of I implies adiabatic invariance of the time T between Andreev reflections. This is the way in which adiabatic invariance is usually proven in textbooks. Our proof explicitly takes into account the fact that phase space in the Andreev billiard consists of two sheets, joined in the constriction at the interface with the superconductor, with a discontinuity in the action on going from one sheet to the other.

The contours of large T enclose a very small area. This will play a crucial role when we quantize the billiard, so let us estimate the area. Electrons leaving the superconductor have transverse momenta in the range $(-p_W, p_W)$, with the value of p_W depending on the details of the potential near the superconductor. It is convenient for our estimate to measure p_x and x in units of p_W and the width W of the constriction to the superconductor [15]. The highly elongated shape evident in Fig. 2.2 is a consequence of the exponential divergence in time of nearby trajectories, characteristic of chaotic dynamics. The rate of divergence is the Lyapunov exponent λ. (We consider a fully chaotic phase space.) Since the Hamiltonian flow is area preserving, a stretching $\ell_+(t) = \ell_+(0)e^{\lambda t}$ of the dimension in one direction needs to be compensated by a squeezing $\ell_-(t) = \ell_-(0)e^{-\lambda t}$ of the dimension in the other direction. The area $O(t) \simeq \ell_+(t)\ell_-(t)$ is then time-independent. Initially, $\ell_\pm(0) < 1$. The constriction at the superconductor acts as a bottleneck, enforcing $\ell_\pm(T) < 1$. These two inequalities imply $\ell_+(t) < e^{\lambda(t-T)}$, $\ell_-(t) < e^{-\lambda t}$. Therefore, the enclosed area has upper bound

$$O_{\max} \simeq p_W W e^{-\lambda T} \simeq \hbar N e^{-\lambda T}, \tag{2.3}$$

where $N \simeq p_W W/\hbar \gg 1$ is the number of channels in the point contact.

We now continue with the quantization. The two invariants E and T define a two-dimensional torus in the four-dimensional phase space. Quantization of this adiabatically invariant torus proceeds following Einstein-Brillouin-Keller [3], by quantizing the area

$$\oint p dq = 2\pi\hbar(m + \nu/4), \quad m = 0, 1, 2, \ldots \tag{2.4}$$

enclosed by each of the two topologically independent contours on the torus. Equation (2.4) ensures that the wavefunctions are single valued. (See Ref. [16] for a derivation in a two-sheeted phase space.) The integer ν counts the number of caustics (Maslov index) and in our case should also include the number of Andreev reflections.

The first contour follows the quasiperiodic orbit of Eq. (2.2), leading to

$$ET = (m + \tfrac{1}{2})\pi\hbar, \quad m = 0, 1, 2, \ldots \tag{2.5}$$

The quantization condition (2.5) is sufficient to determine the smoothed density of states $\rho(E)$, using the classical probability distribution $P(T) \propto \exp(-TN\delta/h)$ [17] for the time between Andreev reflections. (We denote by δ the level spacing in the isolated billiard.) The density of states

$$\rho(E) = N \int_0^\infty dT\, P(T) \sum_{m=0}^{\infty} \delta(E - (m + \tfrac{1}{2})\pi\hbar/T) \tag{2.6}$$

has no gap, but vanishes smoothly $\propto \exp(-N\delta/4E)$ at energies below the Thouless energy $N\delta$. This "Bohr-Sommerfeld approximation" [12] has been quite successful [18–20], but it gives no information on the location of individual energy levels — nor can it be used to determine the wave functions.

To find these we need a second quantization condition, which is provided by the area $\oint_T p_x dx$ enclosed by the contours of constant $T(x, p_x)$,

$$\oint_T p_x dx = 2\pi\hbar(n + \nu/4), \quad n = 0, 1, 2, \ldots \tag{2.7}$$

Equation (2.7) amounts to a quantization of the time T, which together with Eq. (2.5) leads to a quantization of E. For each T_n there is a ladder of Andreev levels $E_{nm} = (m + \frac{1}{2})\pi\hbar/T_n$.

While the classical T can become arbitrarily large, the quantized T_n has a cutoff. The cutoff follows from the maximal area (2.3) enclosed by an isochronous contour. Since Eq. (2.7) requires $O_{\max} > \pi\hbar$, we find that the longest quantized time is $T_0 = \lambda^{-1}[\ln N + \mathcal{O}(1)]$. The lowest Andreev level associated with an adiabatically invariant torus is therefore

$$E_{00} = \frac{\pi\hbar}{2T_0} \simeq \frac{\pi\hbar\lambda}{2\ln N}. \tag{2.8}$$

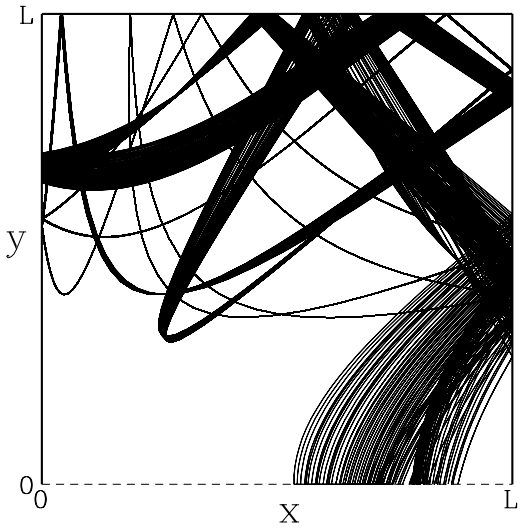

Figure 2.3: Projection onto the x-y plane of the invariant torus with $T = 18$, representing the support of the electron component of the wave function. The flux tube has a large width near the superconductor, which is squeezed to an indistinguishably small value after a few collisions with the boundaries.

The time scale $T_0 \equiv \tau_E \propto |\ln \hbar|$ represents the Ehrenfest time of the Andreev billiard, which sets the scale for the excitation gap in the semiclassical limit [21–23].

We now turn from the energy levels to the wave functions. The wave function has electron and hole components $\psi_{\pm}(x, y)$, corresponding to the two sheets of phase space. By projecting the invariant torus in a single sheet onto the x-y plane we obtain the support of the electron or hole wave function. This is shown in Fig. 2.3, for the same billiard presented in the previous figures. The curves are streamlines that follow the motion of individual electrons, all sharing the same time T between Andreev reflections. (A single one of these trajectories was shown in Fig. 2.1.)

Together the streamlines form a flux tube that represents the support of ψ_+. The width δW of the flux tube is of order W at the constriction, but becomes much smaller in the interior of the billiard. Since $\delta W/W <$

$\ell_+ + \ell_- < e^{\lambda(t-T)} + e^{-\lambda t}$ (with $0 < t < T$), we conclude that the flux tube is squeezed down to a width

$$\delta W_{\min} \simeq W e^{-\lambda T/2}. \tag{2.9}$$

The flux tube for the level E_{00} has a minimal width $\delta W_{\min} \simeq W/\sqrt{N}$. Particle conservation implies that $|\psi_+|^2 \propto 1/\delta W$, so that the squeezing of the flux tube is associated with an increase of the electron density by a factor of $\sqrt{N}$ as one moves away from the constriction.

Let us examine the range of validity of adiabatic quantization. The drift $\delta x, \delta p_x$ upon one iteration of the Poincaré map should be small compared to W, p_F. We estimate

$$\frac{\delta x}{W} \simeq \frac{\delta p_x}{p_W} \simeq \frac{E_{nm}}{\hbar\lambda N} e^{\lambda T_n} \simeq (m + \tfrac{1}{2}) \frac{e^{-\lambda(T_0 - T_n)}}{\lambda T_n}. \tag{2.10}$$

For low-lying levels ($m \sim 1$) the dimensionless drift is $\ll 1$ for $T_n < T_0$. Even for $T_n = T_0$ one has $\delta x/W \simeq 1/\ln N \ll 1$.

Semiclassical methods allow to quantize only the trajectories with times $T \leq T_0 = \tau_E$. We propose that the part of phase space with longer periods can be quantized by random-matrix theory (RMT). Since the RMT description is only valid for a reduced phase space, we call it an effective RMT.

Such an effective RMT calculation has been performed in Ref. [24] and it is summarized in Appendix 2.A. Here we just give the result for the excitation gap $E_{\rm gap}$. It is shown in Fig. 2.4 as a function of τ_E/τ_D (solid line), where the dwell time τ_D is the mean time between Andreev reflections. The two asymptotes (dotted lines) are

$$E_{\rm gap} = \frac{\gamma^{5/2}\hbar}{\tau_D}\left(1 - (2\gamma - 1)\frac{\tau_E}{\tau_D}\right), \quad \tau_E \ll \tau_D, \tag{2.11}$$

$$E_{\rm gap} = \frac{\pi\hbar}{2\tau_E}\left(1 - (3 + \sqrt{8})\frac{\tau_D}{\tau_E}\right), \quad \tau_E \gg \tau_D, \tag{2.12}$$

with $\gamma = \frac{1}{2}(\sqrt{5} - 1)$ the golden number. The results of effective RMT are compared with a calculation of Vavilov and Larkin [25] (dashed line), who use small-angle scattering by a smooth disorder potential to mimick the quantum diffraction of a wave packet in a chaotic billiard [26]. The results of both models are close.

Effective RMT describes the crossover from the Thouless regime where $E_{\rm gap} = 0.30\hbar/\tau_D$ (see Eq. (2.11)) to the Ehrenfest regime with $E_{\rm gap} =$

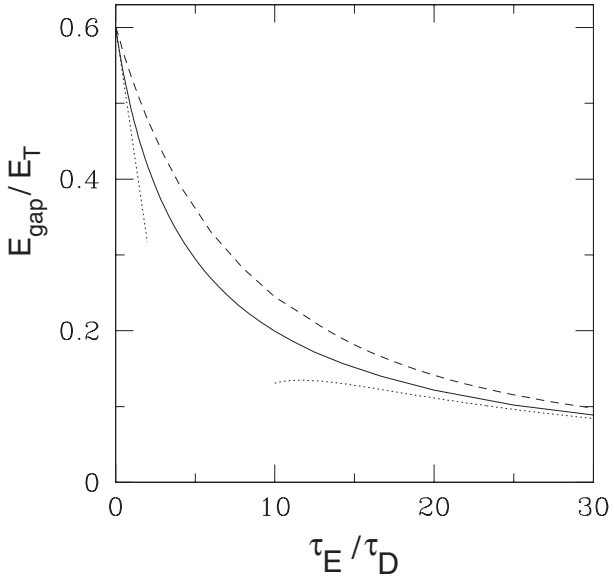

Figure 2.4: Excitation gap of the Andreev billiard in the crossover from Thouless to Ehrenfest regimes. The solid curve is the solution of the effective RMT, derived in App. 2.A. The dotted lines are the two asymptotes (2.11) and (2.12). The dashed curve is the result of the stochastic model of Ref. [25]. Adapted from Ref. [24].

$\pi\hbar/2\tau_E$ (Eq. (2.12)). The value $E_{\rm gap}$ is lower than the lowest adiabatic level $E_{00} = \pi\hbar/2\tau_E$ (they coincide in the limit $\tau_E \to \infty$), meaning that the excitation gap is always an effective RMT level.

Up to now we considered two-dimensional Andreev billiards. Adiabatic quantization may equally well be applied to three-dimensional systems, with the area enclosed by an isochronous contour as the second adiabatic invariant. For a fully chaotic phase space with two Lyapunov exponents λ_1, λ_2, the longest quantized period is $T_0 \simeq \frac{1}{2}(\lambda_1 + \lambda_2)^{-1} \ln N$. We expect interesting quantum size effects on the classical localization of Andreev levels discovered in Ref. [7], which should be measurable in a thin metal film on a superconducting substrate.

A numerical test of the dependence of $E_{\rm gap}$ on τ_E/τ_D was performed in Ref. [27] using a stroboscopic description for an Andreev billiard, the Andreev kicked rotator. The numerical results are in agreement with the

effective RMT prediction of $E_{\rm gap}$ (see Ref. [24] for a comparison). In the Andreev kicked rotator the drift due to a finite excitation energy E was not included and adiabatic levels were not considered. One important challenge for future research is to test the adiabatic quantization of Andreev levels numerically, by solving the Bogoliubov-De Gennes equation on a computer. The characteristic signature of the adiabatic invariant that we have discovered, a narrow region of enhanced intensity in a chaotic region that is squeezed as one moves away from the superconductor, should be readily observable and distinguishable from other features that are unrelated to the presence of the superconductor, such as scars of unstable periodic orbits [10]. Experimentally these regions might be observable using a scanning tunneling probe, which provides an energy and spatially resolved measurement of the electron density.

2.A Effective RMT

In this appendix we summarize the effective RMT calculation of Ref. [24]. Effective RMT is based on the hypothesis that the part of phase space with long trajectories can be quantized by a scattering matrix S_q in the circular ensemble of RMT, with a reduced dimensionality

$$N_{\rm eff} = N \int_{\tau_E}^{\infty} P(T)\, dT = N e^{-\tau_E/\tau_D}. \tag{2.13}$$

The energy dependence of $S_q(E)$ is that of a chaotic cavity with mean level spacing $\delta_{\rm eff}$, coupled to the superconductor by a long lead with $N_{\rm eff}$ propagating modes. (See Fig. 2.5.) The lead introduces a mode-independent delay time τ_E between Andreev reflections, to ensure that $P(T)$ is cut off for $T < \tau_E$. Because $P(T)$ is exponential $\propto \exp(-T/\tau_D)$, the mean time $\langle T\rangle_*$ between Andreev reflections in the accessible part of phase space is simply $\tau_E + \tau_D$. The effective level spacing in the chaotic cavity by itself (without the lead) is then determined by

$$\frac{2\pi\hbar}{N_{\rm eff}\delta_{\rm eff}} = \langle T\rangle_* - \tau_E = \tau_D. \tag{2.14}$$

It is convenient to separate the energy dependence due to the lead from that due to the cavity, by writing $S_q(E) = \exp(iE\tau_E/\hbar)S_0(E)$. The unitary symmetric matrix S_0 corresponds to a chaotic cavity with effective

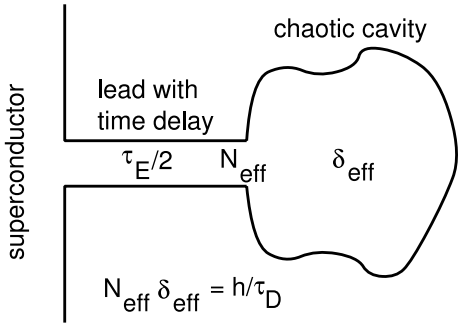

Figure 2.5: Pictorial representation of the effective RMT of an Andreev billiard. The part of phase space with time $T > \tau_E$ between Andreev reflections is represented by a chaotic cavity (mean level spacing $\delta_{\rm eff}$), connected to the superconductor by a long lead ($N_{\rm eff}$ propagating modes, one-way delay time $\tau_E/2$ for each mode). Between two Andreev reflections an electron or hole spends, on average, a time τ_E in the lead and a time τ_D in the cavity. The scattering matrix of lead plus cavity is $\exp(iE\tau_E/\hbar)S_0(E)$, with $S_0(E)$ distributed according to the circular ensemble of RMT (with effective parameters $N_{\rm eff}$, $\delta_{\rm eff}$). The complete excitation spectrum of the Andreev billiard consists of the levels of the effective RMT (periods $> \tau_E$) plus the levels obtained by adiabatic quantization (periods $< \tau_E$). Adapted from Ref. [24].

parameters $N_{\rm eff}$ and $\delta_{\rm eff}$ given by Eqs. (2.13) and (2.14). The mean dwell time associated with S_0 is τ_D. It has an energy dependence of the usual RMT form [28,29]

$$S_0(E) = 1 - 2\pi i W^T (E - H_0 + i\pi W W^T)^{-1} W, \tag{2.15}$$

in terms of the $M \times M$ Hamiltonian H_0 of the closed effective cavity and a $M \times N_{\rm eff}$ coupling matrix W. The matrix $W^T W$ has eigenvalues $w_n = M\delta_{\rm eff}/\pi^2$.

The discrete spectrum of an Andreev billiard with scattering matrix $S_q(E)$ is determined by the determinantal equation [30]

$$\mathrm{Det}\left[1 - \alpha(E)^2 S_q(E) S_q(-E)^*\right] = 0. \tag{2.16}$$

It takes the form

$$\mathrm{Det}\left[1 + e^{2iE\tau_E/\hbar} S_0(E) S_0(-E)^*\right] = 0. \tag{2.17}$$

We have replaced $\alpha(E) \equiv \exp[-i \arccos(E/\Delta)] \to -i$ (since $E \ll \Delta$), but the energy dependence of the phase factor $e^{2iE\tau_E/\hbar}$ can not be omitted. The calculation for $N_{\rm eff} \gg 1$ follows the method described in Ref. [12], modified as in Ref. [31] to account for the energy dependent phase factor in the determinant.

Using Eq. (2.15), we can write Eq. (2.17) in the Hamiltonian form

$$\mathrm{Det}\,[E - \mathcal{H}_{\rm eff}] = 0, \tag{2.18}$$

$$\mathcal{H}_{\rm eff} = \begin{pmatrix} H_0 & 0 \\ 0 & -H_0^* \end{pmatrix} - \mathcal{W}(E), \tag{2.19}$$

$$\mathcal{W}(E) = \frac{\pi}{\cos u} \begin{pmatrix} WW^T \sin u & WW^T \\ WW^T & WW^T \sin u \end{pmatrix}, \tag{2.20}$$

where we have abbreviated $u = E\tau_E/\hbar$. The ensemble averaged density of states is given by

$$\rho_{\rm eff}(E) = -\frac{1}{\pi} \mathrm{Im}\,\mathrm{Tr} \left(1 + \frac{d\mathcal{W}}{dE}\right) \langle (E + i0^+ - \mathcal{H}_{\rm eff})^{-1} \rangle. \tag{2.21}$$

In the presence of time-reversal symmetry the Hamiltonian H_0 of the isolated billiard is a real symmetric matrix. The appropriate RMT ensemble is the GOE, with distribution [32]

$$P(H) \propto \exp\left(-\frac{\pi^2}{4M\delta_{\rm eff}^2} \mathrm{Tr}\, H^2\right). \tag{2.22}$$

The ensemble average $\langle \cdots \rangle$ in Eq. 2.21 is an average over H_0 in the GOE at fixed coupling matrix W. Because of the block structure of $\mathcal{H}_{\rm eff}$, the ensemble averaged Green function $\mathcal{G}(E) = \langle (E - \mathcal{H}_{\rm eff})^{-1} \rangle$ consists of four $M \times M$ blocks $\mathcal{G}_{11}$, $\mathcal{G}_{12}$, $\mathcal{G}_{21}$, $\mathcal{G}_{22}$. By taking the trace of each block separately, one arrives at a 2×2 matrix Green function

$$G = \begin{pmatrix} G_{11} & G_{12} \\ G_{21} & G_{22} \end{pmatrix} = \frac{\delta}{\pi} \begin{pmatrix} \mathrm{Tr}\,\mathcal{G}_{11} & \mathrm{Tr}\,\mathcal{G}_{12} \\ \mathrm{Tr}\,\mathcal{G}_{21} & \mathrm{Tr}\,\mathcal{G}_{22} \end{pmatrix}. \tag{2.23}$$

(The factor δ/π is inserted for later convenience.)

The average over the distribution (2.22) can be done diagrammatically [33, 34]. To leading order in $1/M$ and for $E \gg \delta$ only simple (planar) diagrams need to be considered. Resummation of these diagrams leads to the selfconsistency equation [12, 31]

$$\mathcal{G} = [E + \mathcal{W} - (M\delta_{\rm eff}/\pi)\sigma_z G \sigma_z]^{-1}, \quad \sigma_z = \begin{pmatrix} 1 & 0 \\ 0 & -1 \end{pmatrix}. \tag{2.24}$$

After some algebra we find that $G_{22} = G_{11}$ and $G_{21} = G_{12}$ and there are two unknown functions to determine. For $M \gg N$ these satisfy

$$G_{12}^2 = 1 + G_{11}^2, \tag{2.25a}$$

$$G_{11} + G_{12} \sin u = -(\tau_D/\tau_E) u G_{12} \times (G_{12} + \cos u + G_{11} \sin u). \tag{2.25b}$$

and the density of states (2.21) is given by

$$\rho_{\text{eff}}(E) = -\frac{2}{\delta_{\text{eff}}} \operatorname{Im} \left(G_{11} - \frac{u}{\cos u} G_{12} \right). \tag{2.26}$$

The excitation gap corresponds to a square root singularity in $\rho_{\text{eff}}(E)$, which can be obtained by solving Eqs. (2.25a) and (2.25b) jointly with $dE/dG_{11} = 0$ for $u \in (0, \pi/2)$. The result is plotted in Fig. 2.4. The small- and large-τ_E asymptotes are given by Eqs. (2.11) and (2.12).

Bibliography

[1] P. Ehrenfest, Ann. Phys. (Leipzig) **51**, 327 (1916).

[2] C. C. Martens, R. L. Waterland, and W. P. Reinhardt, J. Chem. Phys. **90**, 2328 (1989).

[3] M. C. Gutzwiller, *Chaos in Classical and Quantum Mechanics* (Springer, Berlin, 1990).

[4] R. E. Prange, in *The Quantum Hall Effect*, edited by R. E. Prange and S. M. Girvin (Springer, New York, 1990).

[5] I. Kosztin, D. L. Maslov, and P. M. Goldbart, Phys. Rev. Lett. **75**, 1735 (1995).

[6] M. Stone, Phys. Rev. B **54**, 13222 (1996).

[7] A. V. Shytov, P. A. Lee, and L. S. Levitov, Phys. Uspekhi **41**, 207 (1998).

[8] İ. Adagideli and P. M. Goldbart, Phys. Rev. B **65**, 201306 (2002).

[9] J. Wiersig, Phys. Rev. E **65**, 036221 (2002).

[10] E. J. Heller, Phys. Rev. Lett. **53**, 1515 (1984).

[11] P. W. O'Connor, J. Gehlen, and E. Heller, Phys. Rev. Lett. **58**, 1296 (1987).

[12] J. A. Melsen, P. W. Brouwer, K. M. Frahm, and C. W. J. Beenakker, Europhys. Lett. **35**, 7 (1996).

[13] Isochronous contours are defined as $T(x, p_x) =$ constant at $E = 0$. We assume that the isochronous contours are closed. This is true if the

border $p_y = 0$ of the classically allowed region in the x, p_x section is itself an isochronous contour, which is the case if $\lim_{y\to 0} \partial V/\partial y \leq 0$. In this case the particle leaving the superconductor with infinitesimal p_y can not penetrate into the billiard.

[14] Adiabatic invariance is defined in the limit $E \to 0$ and is therefore distinct from invariance in the sense of Kolmogorov-Arnold-Moser (KAM), which would require a critical E^* such that a contour is exactly invariant for $E < E^*$. Numerical evidence [5] suggests that the KAM theorem does not apply to a chaotic Andreev billiard.

[15] In this chapter we assume that $p_W/p_F \simeq W/L$, which is typical of a smooth confining potential. In the case $W/L \ll p_W/p_F$, typical for a hard wall potential and for the computer simulations with the Andreev kicked rotator of Ref. [27], the area $O_{\max}$ is larger by a factor W/L (see chapter 5). Consequently the factor $\ln N$ in Eq. (2.8) should be replaced by $\ln(NW/L)$.

[16] K. P. Duncan and B. L. Györffy, Ann. Phys. (New York) **298**, 273 (2002).

[17] W. Bauer and G. F. Bertsch, Phys. Rev. Lett., **65**, 2213 (1990).

[18] H. Schomerus and C. W. J. Beenakker, Phys. Rev. Lett. **82**, 2951 (1999).

[19] W. Ihra, M. Leadbeater, J. L. Vega, and K. Richter, Europhys. J. B **21**, 425 (2001).

[20] J. Cserti, A. Kormányos, Z. Kaufmann, J Koltai, and C. J. Lambert, Phys. Rev. Lett. **89**, 057001 (2002).

[21] A. Lodder and Yu. V. Nazarov, Phys. Rev. B **58**, 5783 (1998).

[22] D. Taras-Semchuk and A. Altland, Phys. Rev. B **64**, 014512 (2001).

[23] İ. Adagideli and C. W. J. Beenakker, Phys. Rev. Lett. **89**, 237002 (2002).

[24] C. W. J. Beenakker, Lect. Notes Phys. **667**, 131 (2005); cond-mat/0406018.

[25] M. G. Vavilov and A. I. Larkin, Phys. Rev. B **67**, 115335 (2003).

[26] I. L. Aleiner and A. I. Larkin, Phys. Rev. B **55**, 1243 (1997).

[27] Ph. Jacquod, H. Schomerus, and C. W. J. Beenakker, Phys. Rev. Lett. **90**, 207004 (2003).

[28] T. Guhr, A. Müller-Groeling, and H. A. Weidenmüller, Phys. Rep. **299**, 189 (1998).

[29] C. W. J. Beenakker, Rev. Mod. Phys. **69**, 731 (1997).

[30] C. W. J. Beenakker, Phys. Rev. Lett. **67**, 3836 (1991); **68**, 1442(E) (1992).

[31] P. W. Brouwer and C. W. J. Beenakker, Chaos, Solitons & Fractals **8**, 1249 (1997).

[32] M. L. Mehta, *Random Matrices* (Academic, New York, 1991).

[33] A. Pandey, Ann. Phys. (N.Y.) **134**, 110 (1981).

[34] E. Brézin and A. Zee, Phys. Rev. E **49**, 2588 (1994).

Chapter 3

Quasiclassical fluctuations of the superconductor proximity gap in a chaotic system

The universality of statistical fluctuations is one of the most profound manifestations of quantum mechanics in mesoscopic systems [1]. Classically, the conductance g of a disordered metal (measured in the fundamental unit $2e^2/h$) would fluctuate from sample to sample by an amount of order $(l/L)^{3/2} \ll 1$, with l the mean free path and L the length of the conductor [2]. Quantum mechanical interference increases the fluctuations to order unity, independent of disorder or sample length. This is the phenomenon of universal conductance fluctuations [3, 4]. The same universality applies to a variety of other properties of disordered metals and superconductors, and random-matrix theory (RMT) provides a unified description [5].

Chaotic systems (for example, a quantum dot in the shape of a stadium) share much of the phenomenology of disordered systems: The same universality of sample-to-sample fluctuations exists [6–8]. What is different is the appearance of a new time scale, below which RMT breaks down [9, 10]. This time scale is the Ehrenfest time τ_E, which measures how long it takes for a wave packet of minimal size to expand over the entire available phase space. If τ_E is larger than the mean dwell time τ_D in the system (the reciprocal of the Thouless energy $E_T = \hbar/2\tau_D$), then interference effects are inoperative. A chaotic system with conductance

$g \times 2e^2/h$, level spacing δ, and Lyapunov exponent λ has $\tau_D = 2\pi\hbar/g\delta$ and $\tau_E = \lambda^{-1}\left[\ln\left(g\tau_0/\tau_D\right) + \mathcal{O}(1)\right]$, with τ_0 the time of flight across the system [11]. The defining characteristic of the Ehrenfest time is that it scales logarithmically with $\hbar$, or equivalently, logarithmically with the system size over Fermi wavelength [12].

The purpose of this chapter is to investigate what happens to mesoscopic fluctuations if the Ehrenfest time becomes comparable to, or larger than, the dwell time, so one enters a quasiclassical regime where RMT no longer holds. This quasiclassical regime has not yet been explored experimentally. The difficulty is that τ_E increases so slowly with system size that the averaging effects of inelastic scattering take over before the effect of a finite Ehrenfest time can be seen. In a computer simulation inelastic scattering can be excluded from the model by construction, so this seems a promising alternative to investigate the crossover from universal quantum fluctuations to nonuniversal quasiclassical fluctuations. Contrary to what one would expect from the disordered metal [2], where quasiclassical fluctuations are much smaller than the quantum value, we find that the breakdown of universality in the chaotic system is associated with an *enhancement* of the sample-to-sample fluctuations.

The quantity on which we choose to focus is the excitation gap E_0 of a chaotic system which is weakly coupled to a superconductor. We have two reasons for this choice: Firstly, there exists a model (the Andreev kicked rotator) which permits a computer simulation for systems large enough that $\tau_E \gtrsim \tau_D$. So far, such simulations, have confirmed the theory of Ref. [11] for the average gap $\langle E_0\rangle$ [13]. Secondly, the quasiclassical theory of chapter 2 can describe the effect of a finite Ehrenfest time on the excitation gap and its fluctuations. This allows us to achieve both a numerical and an analytical understanding of the mesoscopic fluctuations when RMT breaks down.

We summarize what is known from RMT for the gap fluctuations [14]. In RMT the gap distribution $P(E_0)$ is a universal function of the rescaled energy $(E_0 - E_{\rm gap})/\Delta_g$, where $E_{\rm gap} = 0.6\,E_T$ is the mean-field energy gap and $\Delta_g = 0.068\,g^{1/3}\,\delta$ determines the mean level spacing just above the gap. The distribution function has mean $\langle E_0\rangle = E_{\rm gap} + 1.21\,\Delta_g$ and standard deviation $\left(\langle E_0^2\rangle - \langle E_0\rangle^2\right)^{1/2} \equiv \delta E_0^{\rm RMT}$ given by

$$\delta E_0^{\rm RMT} = 1.27\Delta_g = 1.09\,E_T/g^{2/3}. \tag{3.1}$$

The RMT predictions for $P(E_0)$, in the regime $\tau_E \ll \tau_D$, were confirmed numerically in Ref. [13] using the Andreev kicked rotator.

We will use the same model, this time focusing on the gap fluctuations δE_0 in the regime $\tau_E \gtrsim \tau_D$. The Andreev kicked rotator provides a stroboscopic description (period τ_0) of the dynamics in a normal region of phase space (area $M\hbar_{\rm eff}$) coupled to a superconductor in a much smaller region (area $N\hbar_{\rm eff}$, $1 \ll N \ll M$). We refer to this coupling as a "lead". The effective Planck constant is $\hbar_{\rm eff} = 1/M$. The mean dwell time in the normal region (before entering the lead) is $\tau_D = M/N$ and the corresponding Thouless energy is $E_T = N/2M$. We have set τ_0 and $\hbar$ equal to 1. The dimensionless conductance of the lead is $g = N$. The product $\delta = 4\pi E_T/g = 2\pi/M$ is the mean spacing of the quasi-energies ε_m of the normal region without the coupling to the superconductor. The phase factors $e^{i\varepsilon_m}$ ($m = 1, 2, .., M$) are the eigenvalues of the Floquet operator F, which is the unitary matrix that describes the dynamics in the normal region. In the model of the kicked rotator the matrix elements of F in momentum representation are given by [15]

$$F_{nm} = e^{-(i\pi/2M)(n^2+m^2)}(UQU^\dagger)_{nm}, \tag{3.2a}$$

$$U_{nm} = M^{-1/2}e^{(2\pi i/M)nm}, \tag{3.2b}$$

$$Q_{nm} = \delta_{nm}e^{-(iMK/2\pi)\cos(2\pi n/M)}. \tag{3.2c}$$

The coupling to the superconductor doubles the dimension of the Floquet operator, to accomodate both electron and hole dynamics. The scattering from electron to hole, known as Andreev reflection, is described by the matrix

$$\mathcal{P} = \begin{pmatrix} 1 - P^TP & -iP^TP \\ -iP^TP & 1 - P^TP \end{pmatrix}, \tag{3.3}$$

with the projection operator

$$\left(P^TP\right)_{nm} = \delta_{nm} \times \begin{cases} 1 & \text{if } L_0 \le n \le L_0 + N - 1, \\ 0 & \text{otherwise.} \end{cases} \tag{3.4}$$

Since we work in momentum representation, the lead defined by Eq. (3.4) is a strip in phase space of width N parallel to the coordinate axis. The integer L_0 indicates the location of the lead. One could alternatively consider a lead parallel to the momentum axis, if one would work in coordinate

representation. We do not expect any significant differences between the two alternatives. Putting all this together we arrive at the Floquet operator of the Andreev kicked rotator [13],

$$\mathcal{F} = \mathcal{P}^{1/2} \begin{pmatrix} F & 0 \\ 0 & F^* \end{pmatrix} \mathcal{P}^{1/2}. \tag{3.5}$$

The matrix $\mathcal{F}$ can be diagonalized efficiently using the Lanczos technique in combination with the Fast-Fourier-Transform algorithm [16]. This makes it possible to calculate the quasi-energies ε_m and eigenfunctions ψ_m for systems of sizes up to $M = 5 \cdot 10^5$. The gap value $\varepsilon_0 \equiv E_0$ is given by the eigenphase of $\mathcal{F}$ closest to zero. (It is shown in Ref. [13] that the eigenvalue equation for the quasi-energies ε_m of the Andreev kicked rotator has the same form as the equation for the energy spectrum of an Andreev billiard).

The Floquet operator (3.5) provides a stroboscopic description of the electron and hole dynamics, which is believed to be equivalent to the true Hamiltonian dynamics on long time scales $t \gg \tau_0$. The support for this comes from two sides: (i) In the absence of superconductivity, and for varying parameters K and $\hbar_{\rm eff}$, the 1-D kicked rotator correctly reproduces properties of localized [17], diffusive [18], and even ballistic [19] quasiparticles in disordered media. (ii) In the presence of superconductivity, the kicked Andreev rotator, and extensions thereof, adequately describe quantum dots in contact with a superconductor [13], and give a proper description of quasiparticles in dirty d-wave superconductors [20].

Since we will be giving a classical interpretation of our results, we also describe the classical map corresponding to the Andreev kicked rotator. The map relates the dimensionless coordinate $x_n \in (0,1)$ and momentum $p_n \in (0,1)$ at time $(n+1)\tau_0$ to the values at time $n\tau_0$:

$$p_{n+1} = p_n \pm (K/2\pi)\sin[2\pi(x_n \pm \frac{p_n}{2})], \tag{3.6a}$$

$$x_{n+1} = x_n \pm \frac{p_n}{2} \pm \frac{p_{n+1}}{2}. \tag{3.6b}$$

The upper and lower sign correspond to electron and hole dynamics, respectively. Periodic boundary conditions hold both for x and p. The quasiparticle reaches the superconductor if $|p_{n+1} - p_{\rm lead}| < N/2M$, where $p_{\rm lead} = L_0/M$ is the center of the lead. At the next iteration the electron is converted into a hole and vice versa.

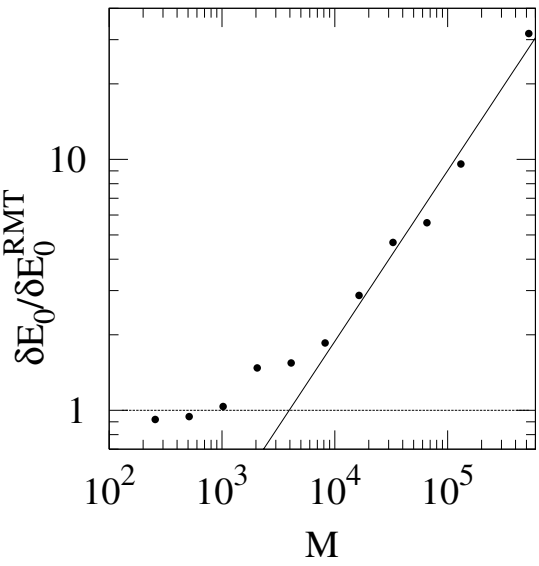

Figure 3.1: Root-mean-square value δE_0 of the gap divided by the RMT prediction $\delta E_0^{\mathrm{RMT}}$, as a function of the system size M for dwell time $M/N = 5$ and kicking strength $K = 14$. The data points result from the numerical simulation of the Andreev kicked rotator. The solid line has slope $2/3$, indicating that δE_0 depends only on M/N and not on M or N separately in the large-M regime.

We study a system with kicking strength $K = 14$ (fully chaotic, Lyapunov exponent $\lambda = 1.95$) and vary the level spacing $\delta = 2\pi/M$ at fixed dwell time $\tau_D = M/N = 5$. Sample-to-sample fluctuations are generated by varying the position p_{lead} of the lead over some 400 locations. The resulting M dependence of δE_0 is plotted in Fig. 3.1 on a double logarithmic scale. We have divided the value δE_0 resulting from the simulation by the RMT prediction $\delta E_0^{\mathrm{RMT}}$ from Eq. (3.1). The numerical data follows this prediction for $M \lesssim 10^3$, but for larger M the fluctuations are bigger than predicted by RMT. For $M \gtrsim 10^4$ the ratio $\delta E_0/\delta E_0^{\mathrm{RMT}}$ grows as $M^{2/3}$ (solid line). Since $\delta E_0^{\mathrm{RMT}} \propto M^{-2/3}$, this means that δE_0 is independent of the level spacing $\delta = 2\pi/M$ at fixed dwell time $\tau_D = M/N$. This suggests a quasiclassical explanation.

To relate the fluctuations of E_0 to the classical dynamics, we first exam-

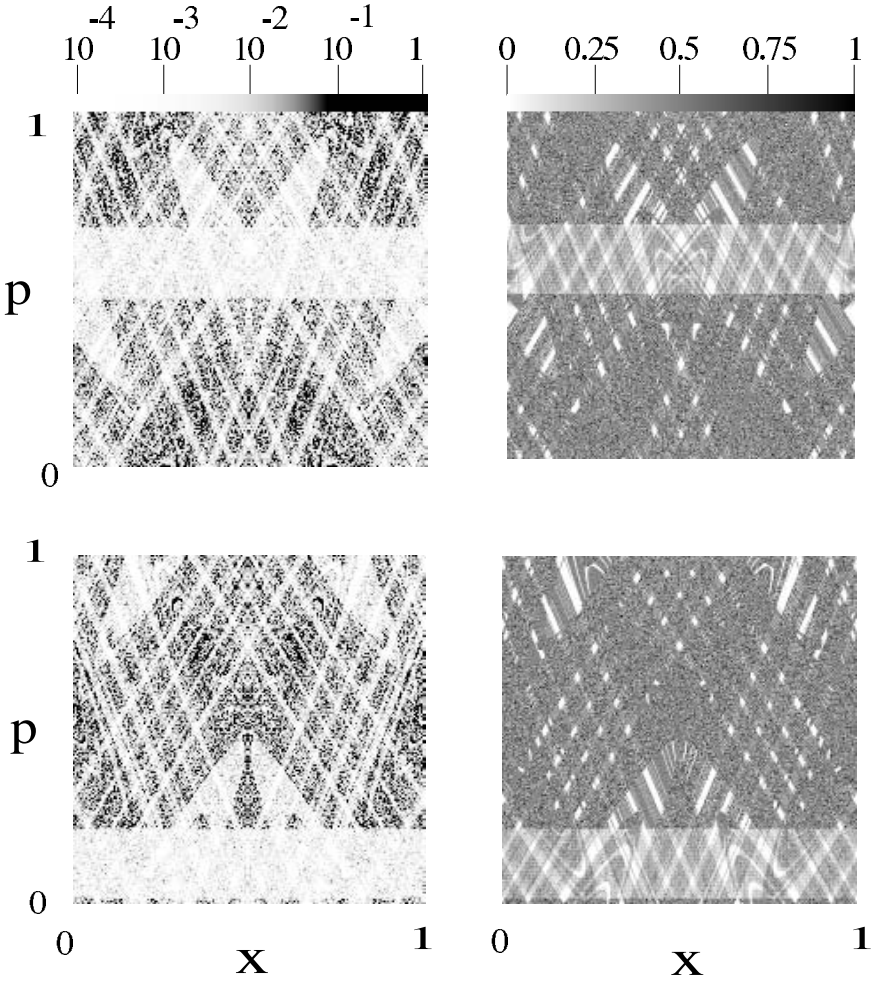

Figure 3.2: Left panels: Husimi function (3.7) for the electron component of the ground-state wavefunction ψ_0 of the Andreev kicked rotator, for two different positions of the lead. The parameters are $M = 131072$, $\tau_D = M/N = 5$, $K = 14$. The calculated values are scaled by a factor 0.019 (0.017) in the top (bottom) panel, so that they cover the range $(0, 1)$, indicated by the gray scale at the top. Right panels: The corresponding classical density plots of all trajectories which have a time $t > \tau_E = 4.4$ between Andreev reflections. The calculated values are rescaled by a factor 0.38 (0.39) in the top (bottom) panel.

ine the corresponding wavefunction ψ_0. In the RMT regime the wavefunctions are random and show no features of the classical trajectories. In the quasiclassical regime $\tau_E \gtrsim \tau_D$ we expect to see some classical features. Phase space portraits of the electron components ψ_m^e of the wavefunctions are given by the Husimi function

$$\mathcal{H}(n_x, n_p) = |\langle \psi_m^e | n_x, n_p \rangle|^2. \tag{3.7}$$

The state $|n_x, n_p\rangle$ is a Gaussian wave packet centered at $x = n_x/M$, $p = n_p/M$. In momentum representation it reads

$$\langle n | n_x, n_p \rangle \propto e^{-\pi(n-n_p)^2/M} e^{2\pi i n_x n/M}. \tag{3.8}$$

In Fig. 3.2, left panels, the Husimi function of ψ_0 is shown for two lead positions. Shown is a logarithmic gray scale density plot of the Husimi function, with light (dark) areas corresponding to low (high) density. The lead is visible as a light strip parallel to the x-axis. It is clear that these wavefunctions are not random. We expect that the structure that one sees corresponds to long classical trajectories, since the wavefunctions are for the excitation gap. To test this expectation, we show in the right panels (on a linear gray scale) the corresponding classical density plots for all trajectories with dwell time $t > \tau_E$. A total of $3 \cdot 10^5$ initial conditions (x_0, p_0) for these trajectories are chosen uniformly in the lead. Each new iteration of the map (3.6) gives a point (x_n, p_n) in phase space, which is kept if the time of return to the lead is greater than the Ehrenfest time $\tau_E \simeq \lambda^{-1} \ln(N^2/M) = 4.4$. There is a clear correspondence between the quantum mechanical Husimi function and the classical density plot. We conclude that the wavefunction of the lowest excitation covers predominantly that part of phase space where the longest dwell times occur.

To make this more quantitative we have done a quasiclassical calculation, based on the effective RMT of the previous chapter. Effective RMT is valid for the part of phase space containing the long trajectories, which have an average time between Andreev reflections

$$\langle T \rangle_* = \int_{\tau_E}^{\infty} T P(T) dT. \tag{3.9}$$

In the pictorial representation of effective RMT (cf. Fig. 2.5), there is a long lead with delay time $\tau_E/2$ and a chaotic cavity with dwell time

$$\tau_D = \langle T \rangle_* - \tau_E. \tag{3.10}$$

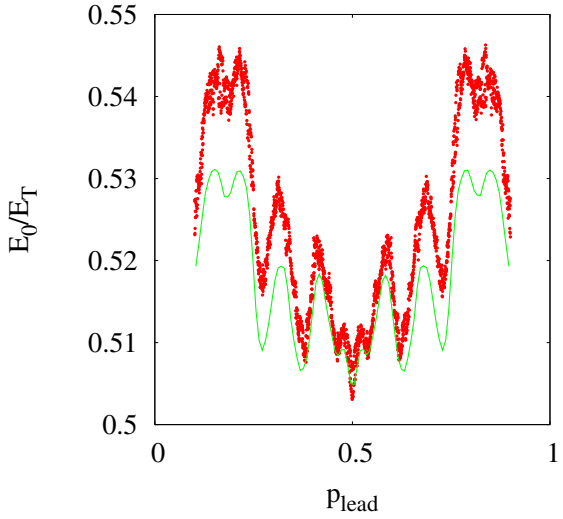

Figure 3.3: The data points are the quantum mechanical gap values E_0 of the Andreev kicked rotator as a function of the position $p_{\text{lead}} = L_0/M$ of the lead, for parameter values $M = 131072$, $\tau_D = M/N = 5$, $K = 14$. The solid line is the effective RMT prediction, relating the fluctuations in E_0 with the fluctuations in the average dwell time of long classical trajectories (with $T > \tau_E$).

We have determined $\langle T \rangle_*$ by a classical simulation of the Andreev kicked rotator for different lead positions. Eq. (3.10) relates the fluctuations in $\langle T \rangle_*$ to the fluctuations in τ_D (we assume that τ_E does not depend on the position of the lead). We obtained the gap by plugging this numerically obtained lead-position-dependent τ_D into the self-consistency equations (2.25a) and (2.25b), and by solving them jointly with $dE/dG_{11} = 0$. This resulted in the solid curve of Fig. 3.3. The data points are from the quantum simulation.

We see that the sample-to-sample fluctuations in the gap E_0 can be quite well described by the fluctuations in the sample-to-sample mean dwell time of long trajectories. While the theory of Ref. [11] has been found to be in good agreement with the average gap value $\langle E_0 \rangle$ [13], it is not clear how it compares to the data of Fig. 3.3.

In conclusion, we have investigated the transition from quantum mechanical to quasiclassical gap fluctuations in the superconductor proxim-

ity effect. The transition is accompanied by a loss of universality and a substantial enhancement of the fluctuations. Our numerical data provides support for the effective random-matrix theory in a reduced part of phase space of chapter 2, as is witnessed by the relationship which we have found between the value of the gap and the dwell time of long classical trajectories (see Fig. 3.3). Similar quasiclassical fluctuations of the conductance in a ballistic chaotic system have been found numerically and they can also be well described by effective RMT [22].

Bibliography

[1] Y. Imry, *Introduction to Mesoscopic Physics* (Oxford University, Oxford, 1997).

[2] Yu.M. Galperin and V.I. Kozub, Europhys. Lett. **15**, 631 (1991).

[3] B.L. Altshuler, JETP Lett. **41**, 648 (1985).

[4] P.A. Lee and A.D. Stone, Phys. Rev. Lett. **55**, 1622 (1985).

[5] C.W.J. Beenakker, Phys. Rev. B **47**, 15763 (1993).

[6] C.W.J. Beenakker, Rev. Mod. Phys. **69**, 731 (1997).

[7] T. Guhr, A. Müller-Groeling, and H. A. Weidenmüller, Phys. Rep. **299**, 189 (1998).

[8] Y. Alhassid, Rev. Mod. Phys. **72**, 895 (2000).

[9] A. Lodder and Yu. V. Nazarov, Phys. Rev. B **58**, 5783 (1998).

[10] I.L. Aleiner and A.I. Larkin, Phys. Rev. B **54**, 14423 (1996).

[11] M.G. Vavilov and A.I. Larkin, Phys. Rev. B **67**, 115335 (2003).

[12] G.M. Zaslavsky, Phys. Rep. **80**, 157 (1981).

[13] Ph. Jacquod, H. Schomerus, and C.W.J. Beenakker, Phys. Rev. Lett. **90**, 207004 (2003).

[14] M.G. Vavilov, P.W. Brouwer, V. Ambegaokar, and C.W.J. Beenakker, Phys. Rev. Lett. **86**, 874 (2001).

[15] F.M. Izrailev, Phys. Rep. **196**, 299 (1990).

[16] R. Ketzmerick, K. Kruse, and T. Geisel, Physica D **131**, 247 (1999).

[17] S. Fishman, D. R. Grempel, and R. E. Prange, Phys. Rev. Lett. **49**, 509 (1984).

[18] A. Altland and M. R. Zirnbauer, Phys. Rev. Lett. **77**, 4536 (1996).

[19] J. Tworzydło, A. Tajic, H. Schomerus, and C.W.J. Beenakker, Phys. Rev. B, 115313 (2003).

[20] İ. Adagideli and Ph. Jacquod, Phys. Rev. B **69**, 020503 (2004).

[21] C. W. J. Beenakker, Lect. Notes Phys. **667**, 131 (2005); cond-mat/0406018.

[22] J. Tworzydło, A. Tajic, and C. W. J. Beenakker, Phys. Rev. B **69**, 165318 (2004).

Chapter 4

Quantum-to-classical crossover for Andreev billiards in a magnetic field

4.1 Introduction

When a quantum dot is coupled to a superconductor via a point contact, the conversion of electron to hole excitations by Andreev reflection governs the low-energy spectrum. The density of states of such an Andreev billiard was calculated using random-matrix theory (RMT) [1]. If the classical dynamics in the isolated quantum dot is chaotic, a gap opens up in the spectrum. The excitation gap $E_{\rm gap}$ is of the order of the Thouless energy $\hbar/\tau_D$, with τ_D the average time between Andreev reflections. Although chaoticity of the dynamics is essential for the gap to open, the size of the gap in RMT is independent of the Lyapunov exponent λ of the chaotic dynamics.

If the size L of the quantum dot is much larger than the Fermi wavelength λ_F, a competing timescale $\tau_E \simeq \lambda^{-1} \ln (L/\lambda_F)$ appears, the Ehrenfest time, which causes the breakdown of RMT [2]. The gap becomes dependent on the Lyapunov exponent and for $\tau_E \gg \tau_D$ vanishes as $E_{\rm gap} \simeq \hbar/\tau_E$. The Ehrenfest time dependence of the gap has been investigated in chapter 2 and 3 and in several other works [3–7]. For a recent review, see Ref. [8].

A magnetic field breaks time-reversal symmetry, thereby reducing $E_{\rm gap}$. At a critical field B_c the gap closes. This was calculated using RMT in Ref.

[9], but the effect of a finite Ehrenfest time was not studied before. Here we extend the zero-field theory of chapter 2 to non-zero magnetic field. It is a quasiclassical theory, which relates the excitation spectrum to the classical dynamics in the billiard. The entire phase space is divided into two parts, depending on the time T between Andreev reflections. Times $T < \tau_E$ are quantized by identifying the adiabatic invariant, while times $T > \tau_E$ are quantized by an effective RMT with τ_E-dependent parameters.

There exists an alternative approach to quantization of the Andreev billiard, due to Vavilov and Larkin [5], which might also be extended to non-zero magnetic field. In zero magnetic field the two models have been shown to give similar results (see Fig. 2.4), so we restrict ourselves here to the approach of chapter 2.

The outline of the chapter is as follows. We start by describing the adiabatic levels in Sec. 4.2, followed by the effective RMT in Sec. 4.3. In Sec. 4.4 we compare our quasiclassical theory with fully quantum mechanical computer simulations. We conclude in Sec. 4.5.

4.2 Adiabatic quantization

We generalize the theory of adiabatic quantization of the Andreev billiard of chapter 2 to include the effect of a magnetic field. An example of the geometry of such a billiard is sketched in Fig. 4.1. The normal metal lies in the x-y plane and the boundary with the superconductor (NS boundary) is at $y = 0$. The classical mechanics of electrons and holes in such an Andreev billiard has been analyzed in Refs. [10–12]. We first summarize the results we need, then proceed to the identification of the adiabatic invariant, and finally present its quantization.

4.2.1 Classical mechanics

The classical equation of motion

$$\ddot{\mathbf{r}}(t) = -\frac{e}{m}\dot{\mathbf{r}} \times \mathbf{B} + \frac{e}{m}\nabla V(\mathbf{r}) \tag{4.1}$$

is the same for the electron and the hole because both charge e and mass m change sign. The vector $\mathbf{B}$ is the uniform magnetic field in the z-direction and $V(\mathbf{r})$ is the electrostatic potential in the plane of the billiard.

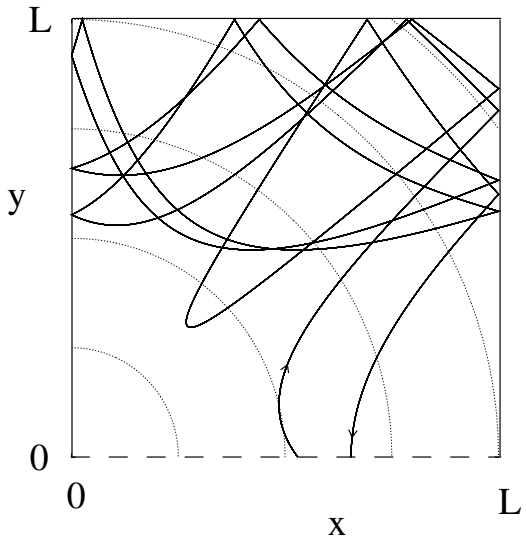

Figure 4.1: Classical trajectory in an Andreev billiard. Particles are deflected by the potential $V = \left[(r/L)^2 - 1\right]V_0$ for $r < L$, $V = \left[-4(r/L)^2 + 10(r/L) - 6\right]V_0$ for $r > L$, with $r^2 = x^2 + y^2$ (the dotted lines are equipotentials). At the insulating boundaries (solid lines) there is specular reflection, while the particles are Andreev reflected at the superconductor ($y = 0$, dashed line). Shown is the trajectory of an electron at the Fermi level ($E = 0$), for $B = 0$ and $E_F = 0.84\, eV_0$. The Andreev reflected hole will retrace this path.

The dots on $\mathbf{r} = (x, y)$ denote time derivatives. We follow the classical trajectory of an electron starting at the NS boundary position $(x, 0)$ with velocity (v_x, v_y). The electron is at an excitation energy E counted from the Fermi level. After a time T the electron returns to the superconductor and is retroreflected as a hole. Retroreflection means that $v_x \to -v_x$. The y-component v_y of the velocity also changes sign, but in addition it is slightly reduced in magnitude, $v_y^2 \to v_y^2 - 4E/m$, so that an electron at an energy E above the Fermi level becomes a hole at an energy E below the Fermi level.

This refraction is one reason why the hole does not precisely retrace

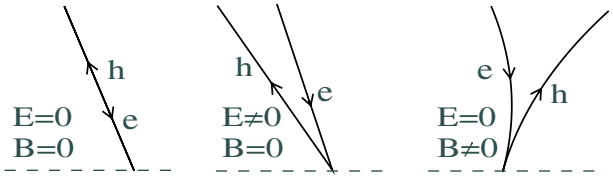

Figure 4.2: Andreev reflection at a NS boundary (dashed line) of an electron to a hole. The left panel shows the case of perfect retroreflection (zero excitation energy E and zero magnetic field B). The middle and right panels show that the hole does not precisely retrace the path of the electron if E or B are non-zero.

the path of the electron. A second reason is that a non-zero B will cause the hole trajectory to bend in the direction opposite to the electron trajectory (because the velocity has changed sign), see Fig. 4.2. It follows that if either E or B are non-zero, the hole will return to the NS boundary at a slightly different position and with a slightly different velocity. The resulting drift of the quasi-periodic motion is most easily visualized in a Poincaré surface of section, see Fig. 4.3. Each dot marks the position x and tangential velocity v_x of an electron leaving the NS boundary. At non-zero E or B, subsequent dots are slightly displaced, tracing out a contour in the (x, v_x) plane. In the limit $E, B \to 0$, the shape of these contours is determined by the adiabatic invariant of the classical dynamics. In chapter 2 it was shown that the contours in the Poincaré surface of section are *isochronous* for $B = 0$. This means that they are given by $T(x, v_x) = \text{const}$, with $T(x, v_x)$ the time it takes an electron at the Fermi level to return to the NS boundary, as a function of the starting point (x, v_x) on the boundary. In other words, for $B = 0$ the time between Andreev reflections is an adiabatic invariant in the limit $E \to 0$.

4.2.2 Adiabatic invariant

We generalize the construction of the adiabatic invariant of chapter 2 to $B \neq 0$. We start from the Poincaré invariant

$$\mathcal{I}(t) = \oint_{C(t)} \mathbf{p} \cdot d\mathbf{r} \tag{4.2}$$

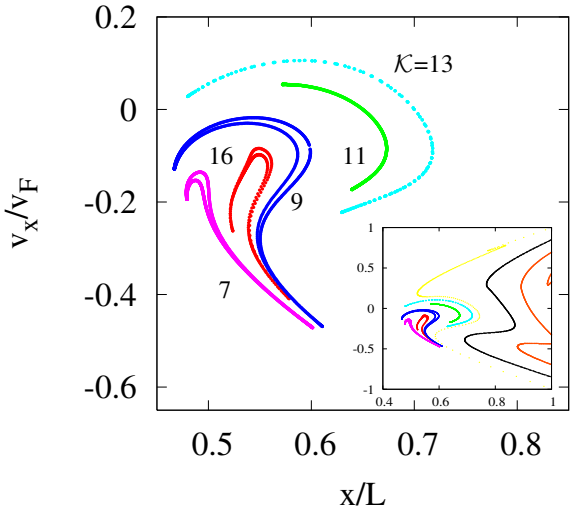

Figure 4.3: Poincaré map for the Andreev billiard of Fig. 4.1. Each dot marks the position x and tangential velocity v_x of an electron at the NS boundary. Subsequent dots are obtained by following the electron trajectory for $E, B \to 0$ at fixed ratio $B/E = \frac{1}{3}\sqrt{m/V_0 L^2 e^3}$. The inset shows the full surface of section of the Andreev billiard, while the main plot is an enlargement of the central region. The drift is along closed contours defined by $\mathcal{K}$ = constant [see Eq. (4.4)]. The value of the adiabatic invariant $\mathcal{K}$ (in units of $\sqrt{mL^2/eV_0}$) is indicated for several contours. All contours are closed loops, but for some contours the opening of the loop is not visible in the figure.

over a closed contour $C(t)$ in phase space that moves according to the classical equations of motion. The contour extends over two sheets of phase space, joined at the NS interface. In the electron sheet the canonical momentum is $\mathbf{p}_+ = m\mathbf{v}_+ - e\mathcal{A}$, while in the hole sheet it is $\mathbf{p}_- = -m\mathbf{v}_- + e\mathcal{A}$. Both the velocity $\mathbf{v}_\pm$, given in absolute value by $|\mathbf{v}_\pm| = (2/m)^{1/2}[E_F \pm E + eV(\mathbf{r})]^{1/2}$ and directed along the motion, as well as the vector potential $\mathcal{A} = \frac{1}{2}B\hat{z} \times \mathbf{r}$ are functions of the position $\mathbf{r}$ on the contour, determined, respectively, by the energy E and the magnetic field B. (Since the contour is closed, the Poincaré invariant is properly gauge invariant.)

Quite generally, $d\mathcal{I}/dt = 0$, meaning that $\mathcal{I}$ is a constant of the motion

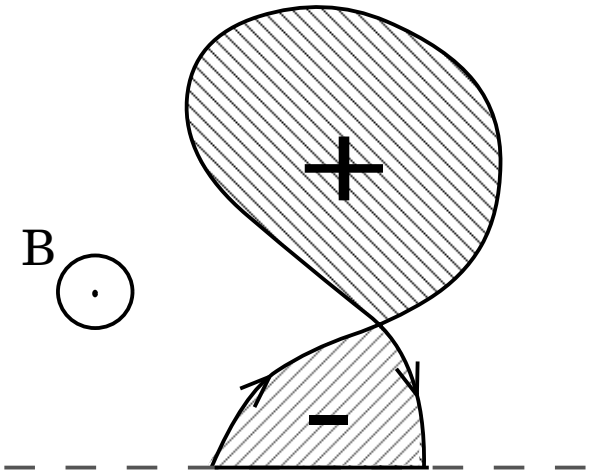

Figure 4.4: Directed area for a classical trajectory, consisting of the area enclosed by the trajectory after joining begin and end points along the NS boundary (dashed line). Different parts of the enclosed area have different signs because the boundary is circulated in a different direction.

[13]. For $E = B = 0$ we take $C(0)$ to be the self-retracing orbit from electron to hole and back to electron. It is obviously time-independent, with $\mathcal{I} = 0$ (because the contributions from electron and hole sheet cancel). For E or B non-zero, we construct $C(0)$ from the same closed trajectory in real space, but now with $\mathbf{p}_{\pm}(\mathbf{r})$ and $\mathcal{A}(\mathbf{r})$ calculated at the given values of E and B. Consequently, this contour $C(t)$ will drift in phase space, preserving $\mathcal{I}(t) = \mathcal{I}(0)$. The Poincaré invariant is of interest because it is closely related to the action integral

$$I = \oint_{O_{eh}} \mathbf{p} \cdot d\mathbf{r}. \tag{4.3}$$

The action integral is defined as an integral along the periodic electron-hole orbit O_{eh} followed by electrons and holes at $E, B = 0$. To every point (x, v_x) in the Poincaré surface of section corresponds an orbit O_{eh} and hence an action integral $I(x, v_x)$. We compare the contour $C(t)$ and the trajectory O_{eh} intersecting the Poincaré surface of section at the same point (x, v_x). At $t = 0$ they coincide and for sufficiently slow drifts they stay close and therefore the action integral $I = \mathcal{I}(0) + \mathcal{O}(t^2)$ is an adiabatic invariant of the motion in the Poincaré surface of section [13].

It remains to determine the adiabatic invariant I in terms of E and B and the chosen trajectory $C(0)$. To linear order in E, B we find

$$I = 2E\mathcal{K}, \quad \mathcal{K} \equiv T - eAB/E, \tag{4.4}$$

with $A = \frac{1}{2}\oint(\mathbf{r} \times d\mathbf{r}) \cdot \hat{z}$ the directed area (see Fig. 4.4) enclosed by the electron trajectory and the NS boundary. Both the time T and the area A are to be evaluated at $E = B = 0$. Because E is a constant of the motion, adiabatic invariance of I implies that $\mathcal{K} \equiv I/2E$ is an adiabatic invariant. At zero field this adiabatic invariant is simply the time T between Andreev reflections. At non-zero field the invariant time contains also an electromagnetic contribution $-eAB/E$, proportional to the enclosed flux.

Fig. 4.3 shows that, indeed, the drift in the Poincaré surface of section is along contours $C_{\mathcal{K}}$ of constant $\mathcal{K}$. In contrast to the zero-field case, the invariant contours in the surface of section are now no longer energy-independent. This will have consequences for the quantization, as we describe next.

4.2.3 Quantization

The two invariants E and $\mathcal{K}$ define a two-dimensional torus in four-dimensional phase space. The two topologically independent closed contours on this torus are formed by the periodic electron-hole orbit O_{eh} and the contour $C_{\mathcal{K}}$ in the Poincaré surface of section. The area they enclose is quantized following the prescription of Einstein-Brillouin-Keller [14, 15],

$$\oint_{O_{eh}} \mathbf{p} \cdot d\mathbf{r} = 2\pi\hbar(m + 1/2), \qquad m = 0, 1, 2, \ldots \tag{4.5a}$$

$$\oint_{C_{\mathcal{K}}} p_x dx = 2\pi\hbar(n + 1/2), \qquad n = 0, 1, 2, \ldots. \tag{4.5b}$$

The action integral (4.5a) can be evaluated explicitly, leading to

$$E\mathcal{K} = \pi\hbar(m + 1/2). \tag{4.6}$$

The second quantization condition (4.5b) gives a second relation between E and $\mathcal{K}$, so that one can eliminate $\mathcal{K}$ and obtain a ladder of levels E_{mn}. For $B = 0$ the quantization condition (4.5b) is independent of E, so one obtains separately a quantized time T_n and quantized energy $E_{mn} = (m + 1/2)\pi\hbar/T_n$. For $B \neq 0$ both $\mathcal{K}_{mn}$ and E_{mn} depend on the sets of integers m, n.

4.2.4 Lowest adiabatic level

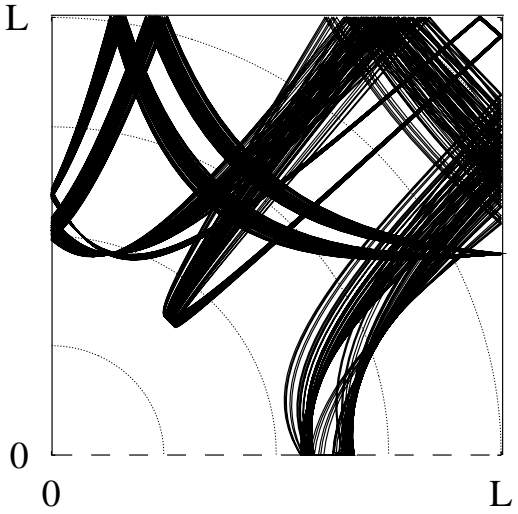

Figure 4.5: Illustration of a bunch of trajectories within a single scattering band in the billiard defined in Fig. 4.1. All trajectories in this figure have starting conditions in the band containing the contour with $\mathcal{K} = 11$ of Fig. 4.3. Both T and A vary only slightly from one trajectory to the other, so that the whole band can be characterized by a single $\bar{T}$ and $\bar{A}$, being the average of T and A over the scattering band.

The value E_{00} of the lowest adiabatic level follows from the pair of quantization conditions (4.5) with $m = n = 0$. To determine this value we need to determine the area $O(\mathcal{K}) = \oint_{C_\mathcal{K}} p_x dx$ enclosed by contours of constant $\mathcal{K}$, in the limit of large $\mathcal{K}$.

In chapter 2 the area $O(\mathcal{K})$ was determined in the case $B = 0$, when $\mathcal{K} = T$ and the contours are isochronous. It was found that

$$O(T) \lesssim O_0 \exp(-\lambda T), \tag{4.7}$$

with λ the Lyapunov exponent of the normal billiard without superconductor and O_0 a characteristic area that depends on the angular distribution of the beam of electrons entering the billiard (width L) from the narrow

contact to the superconductor (width W). For a collimated beam having a spread of velocities $|v_W/v_F| \lesssim W/L$ one has $O_0 = Nh$ (see chapter 2). For a non-collimated beam $O_0 = NhW/L$ (this will be explained in chapter 5). The integer N is the number of scattering channels connecting the billiard to the superconductor. The quantization requirement $O(T) \geq \pi\hbar$ gives the lowest adiabatic level in zero magnetic field,

$$E_{00}(B=0) = \frac{\pi\hbar}{2\tau_E}, \qquad \tau_E = \frac{1}{\lambda}\left[\ln\left(O_0/\pi\hbar\right) + \mathcal{O}(1)\right]. \tag{4.8}$$

The Ehrenfest time τ_E corresponds to a contour that encloses an area $\pi\hbar$.

In order to generalize Eq. (4.7) to $B \neq 0$, we discuss the concept of scattering bands, which will be discussed in chapter 5 for a normal billiard (where they are called transmission and reflection bands). Scattering bands are ordered phase space structures that appear in open systems, even if their closed counterparts are fully chaotic. These structures are characterized by regions in which the functions $T(x, v_x)$ and $A(x, v_x)$ vary slowly almost everywhere. Hence, they contain orbits of almost constant return time and directed area, that is, orbits returning by bunches. One such bunch is depicted in Fig. 4.5. The scattering bands are bounded by contours of diverging $T(x, v_x)$ and $A(x, v_x)$. The divergence is very slow ($\propto 1/\ln\epsilon$, with ϵ the distance from the contour [4]), so the mean return time $\bar{T}$ and mean directed area $\bar{A}$ in a scattering band remain finite and well defined [16].

The area O_{band} of a band depends on $\bar{T}$ as (see chapter 5)

$$O_{\text{band}}(\bar{T}) \simeq O_0 \exp\left(-\lambda\bar{T}\right). \tag{4.9}$$

Since an isochronous contour must lie within a single scattering band, Eq. (4.7) follows from Eq. (4.9) and from the fact that the distribution of return times is sharply peaked around the mean $\bar{T}$. Because contours of constant $\mathcal{K} = T - eAB/E$ must also lie within a single scattering band, the area $O(\mathcal{K})$ is bounded by the same function $O_{\text{band}}(\bar{T})$. We conclude that within a given scattering band the largest contour of constant T and the largest contour of constant $\mathcal{K}$ each have approximately the same area as the band itself,

$$O(T), O(\mathcal{K}) \lesssim O_{\text{band}}(\bar{T}) \simeq O_0 \exp(-\lambda\bar{T}). \tag{4.10}$$

We are now ready to determine the magnetic field dependence of the lowest adiabatic level $E_{00}(B)$. The corresponding contour $C_{\mathcal{K}}$ lies in a

band characterized by a mean return time $\bar{T} \simeq \lambda^{-1} \ln(O_0/\pi\hbar)$, according to Eqs. (4.5b) and (4.10). This is the same Ehrenfest time as Eq. (4.8) for $B = 0$ (assuming that the orbital effect of the magnetic field does not modify λ) . The energy of the lowest adiabatic level E_{00} is determined by the quantization condition (4.6),

$$E_{00}\mathcal{K} \simeq E_{00}\tau_E + eA_{\max}B = \pi\hbar/2. \tag{4.11}$$

The range of directed areas $-A_{\max} \lesssim \bar{A} \lesssim A_{\max}$ is the product of the area L^2 of the billiard and the maximum number of times $n_{\max} \approx \nu_F \bar{T}/L$ that a trajectory can encircle that area (clockwise or counterclockwise) in a time $\bar{T}$. Hence $A_{\max} = \nu_F \bar{T} L \lesssim \nu_F \tau_E L$ and we find

$$E_{00}(B) \equiv E_{\rm gap}^{\rm ad} \simeq \frac{\pi\hbar}{2\tau_E} - e\nu_F LB. \tag{4.12}$$

We conclude that a magnetic field shifts the lowest adiabatic level downward by an amount $e\nu_F LB$ which is independent of τ_E. Eq. (4.12) holds up to a field $B_c^{\rm ad}$ at which the lowest adiabatic level reaches the Fermi level,

$$B_c^{\rm ad} \simeq \frac{\pi\hbar}{2eA_{\max}} \simeq \frac{\pi\hbar}{2\tau_E e\nu_F L}. \tag{4.13}$$

We have added the label "ad", because the true critical field at which the gap closes may be smaller due to non-adiabatic levels below E_{00}. For $B = 0$, the ground state is never an adiabatic state (chapter 2). In the next section we study the effective RMT, in order to determine the contribution from non-adiabatic levels (return times $T > \tau_E$).

4.2.5 Density of states

The pair of quantization conditions (4.5) determines the individual energy levels with $T < \tau_E$ and $|A| < A_{\max} \simeq \nu_F \tau_E L$. For semiclassical systems with $L/\lambda_F \gg 1$ the level spacing δ of the isolated billiard is so small that individual levels are not resolved and it suffices to know the smoothed (or ensemble averaged) density of states $\rho_{\rm ad}(E)$. In view of Eq. (4.6) it is given by

$$\rho_{\rm ad}(E) = N \int_0^{\tau_E} dT \int_{-A_{\max}}^{A_{\max}} dA\, P(T,A) \times \sum_m \delta\left(E - \frac{\pi\hbar(m+1/2) + eAB}{T}\right), \tag{4.14}$$

in terms of the joint distribution function $P(T, A)$ of return time T and directed area A. In the limit $\tau_E \to \infty$ this formula reduces to the Bohr-Sommerfeld quantization rule of Ref. [1] for $B = 0$ and to the generalization of Ref. [17] for $B \neq 0$. The adiabatic density of states (4.14) vanishes for $E < E_{\rm gap}^{\rm ad}$. Its high energy asymptotics (meaning $E \gg E_{\rm gap}^{\rm ad}$, but still $E \ll \Delta$) can be estimated using $P(T, A) = P(A|T)P(T)$ with the conditional distribution $P(A|T)$ (which will be discussed in the next section) and the return time distribution $P(T) = \exp(-T/\tau_D)\tau_D^{-1}$. One gets

$$\lim_{\substack{E\to\infty \\ E\ll\Delta}} \rho_{\rm ad}(E) = \frac{2}{\delta}\left(1 - e^{-\tau_E/\tau_D}\left[1 + \frac{\tau_E}{\tau_D}\right]\right). \tag{4.15}$$

The limit (4.15) is less than the value $2/\delta$, which also contains the contribution from the non-adiabatic levels with $T > \tau_E$.

4.3 Effective random-matrix theory

The adiabatic quantization applies only to the part of phase space in which the return time T is less than the Ehrenfest time τ_E. To quantize the remainder, with $T > \tau_E$, we apply the effective random-matrix theory (RMT) of chapter 2. The existing formulation does not yet include a magnetic field, so we begin by extending it to non-zero B.

4.3.1 Effective cavity

The effective RMT is based on the decomposition of the scattering matrix in the time domain into two parts,

$$S(t) = \begin{cases} S_{cl}(t) & \text{if } t < \tau_E \\ S_q(t) & \text{if } t > \tau_E. \end{cases} \tag{4.16}$$

The classical, short-time part $S_{cl}(t)$ couples to N_{cl} scattering channels of return time $< \tau_E$, which can be quantized adiabatically as explained in the previous section. The remaining

$$N_q = N - N_{cl} = Ne^{-\tau_E/\tau_D} \equiv N_{\rm eff} \tag{4.17}$$

quantum channels, with return time $> \tau_E$, are quantized by RMT with effective τ_E-dependent parameters.

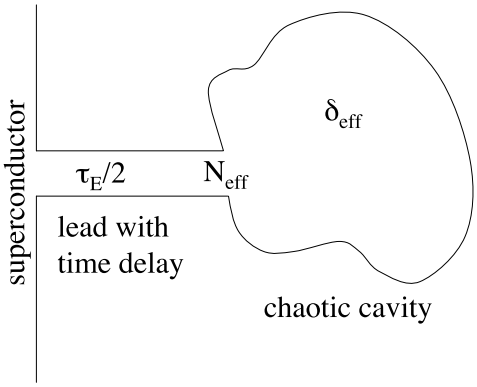

Figure 4.6: Pictorial representation of the effective RMT of an Andreev billiard. The part of phase space with long trajectories (return time $> \tau_E$) is represented by a *chaotic* cavity with level spacing $\delta_{\rm eff}$, connected to the superconductor via a *fictitious* ballistic lead with $N_{\rm eff}$ channels. The lead introduces a channel-independent delay time $\tau_E/2$ and a channel-dependent phase shift ϕ_n, which is different from the distribution of phase shifts in a real lead.

To describe the effective RMT ensemble from which S_q is drawn, we refer to the diagram of Fig. 4.6, following Ref. [8]. A wave packet of return time $t > \tau_E$ evolves along a classical trajectory for the initial $\tau_E/2$ and the final $\tau_E/2$ duration of its motion. This classical evolution is represented by a fictitious ballistic lead with delay time $\tau_E/2$, attached at one end to the superconductor. The transmission matrix of this lead is an $N_{\rm eff} \times N_{\rm eff}$ diagonal matrix of phase shifts $\exp[i\Phi(B)]$ (for transmission from left to right) and $\exp[i\Phi(-B)]$ (for transmission from right to left). The ballistic lead is attached at the other end to a chaotic cavity having an $N_{\rm eff} \times N_{\rm eff}$ scattering matrix S_0 with RMT distribution. The entire scattering matrix $S_q(t)$ of the effective cavity plus ballistic lead is, in the time domain,

$$S_q(t) = e^{i\Phi(-B)} S_0(t - \tau_E, B) e^{i\Phi(B)}, \tag{4.18}$$

and in the energy domain,

$$S_q(E) = e^{iE\tau_E/\hbar} e^{i\Phi(-B)} S_0(E, B) e^{i\Phi(B)}. \tag{4.19}$$

The level spacing $\delta_{\rm eff}$ of the effective cavity is increased according to

$$\delta_{\rm eff}/\delta = N/N_{\rm eff} = e^{\tau_E/\tau_D}, \tag{4.20}$$

to ensure that the mean dwell time $2\pi\hbar/N_{\rm eff}\delta_{\rm eff}$ remains equal to τ_D, independent of the Ehrenfest time.

For weak magnetic fields (such that the cyclotron radius $m\nu_F/eB \gg L$), the phase shifts $\Phi(B)$ are linear in B:

$$\Phi(B) \simeq \Phi(0) + B\Phi'(0) \equiv \Phi(0) + {\rm diag}\left[\phi_1, \phi_2 \ldots \phi_{N_{\rm eff}}\right]. \tag{4.21}$$

The phases ϕ_n are the channel-dependent, magnetic field induced phase shifts of classical trajectories spending a time $\tau_E/2$ in a chaotic cavity.

The conditional distribution of directed areas A for a given return time T is a truncated Gaussian [17,18],

$$\begin{aligned} P(A|T) &\propto \exp\left(-A^2/A_0^2\right)\theta(A_{\rm max} - |A|), \\ A_0^2 &\propto \nu_F T L^3, \end{aligned} \tag{4.22}$$

with $\theta(x)$ the unit step function. This implies that the distribution $P(\phi)$ of phase shifts $\phi = eAB/\hbar$ for $T = \tau_E/2$ is given by

$$P(\phi) \propto \exp\left[-\frac{\phi^2}{c}\frac{\tau_D}{\tau_E}\left(\frac{B_0}{B}\right)^2\right]\theta\left(\phi_{\rm max} - |\phi|\right), \tag{4.23}$$

$$\phi_{\rm max} = \frac{eA_{\rm max}B}{\hbar} \simeq \frac{B}{B_0}\sqrt{\frac{\nu_F\tau_E^2}{L\tau_D}}. \tag{4.24}$$

The constant c of order unity is determined by the billiard geometry and B_0 denotes the critical magnetic field of the Andreev billiard when $\tau_E \to 0$. Up to numerical coefficients of order unity, one has [9]

$$B_0 \simeq \frac{\hbar}{eL^2}\sqrt{\frac{L}{\nu_F\tau_D}}. \tag{4.25}$$

4.3.2 Density of states

The energy spectrum of an Andreev billiard, for energies well below the gap Δ of the bulk superconductor, is related to the scattering matrix by the determinantal equation [19]

$$\mathrm{Det}\left[1 + S(E)S^*(-E)\right] = 0. \tag{4.26}$$

Since S_{cl} and S_q couple to different channels, we may calculate separately the contribution to the spectrum from the effective cavity, governed by S_q. We substitute the expression (4.19) for S_q, to obtain

$$\mathrm{Det}\left[1 + e^{2iE\tau_E/\hbar} S_0(E,B)\Omega(B)S_0^*(-E,B)\Omega^*(B)\right] = 0, \tag{4.27}$$

$$\Omega(B) \equiv e^{i\Phi(B)-i\Phi(-B)} = \mathrm{diag}[e^{2i\phi_1}, e^{2i\phi_2} \ldots e^{2i\phi_{N_{\mathrm{eff}}}}]. \tag{4.28}$$

In chapter 2 the density of states was calculated from this equation for the case $B = 0$, when $\Omega = 1$. We generalize the calculation to $B \neq 0$. The technicalities are very similar to those of Ref. [20].

The scattering matrix $S_0(E,B)$ of the open effective cavity can be represented by [21,22]

$$S_0(E,B) = 1 - 2\pi i W^T \left[E - H_0(B) + i\pi W W^T\right]^{-1} W, \tag{4.29}$$

in terms of the Hamiltonian $H_0(B)$ of the closed effective cavity and a coupling matrix W. The dimension of H_0 is $M \times M$ and the dimension of W is $M \times N_{\mathrm{eff}}$. The matrix $W^T W$ has eigenvalues $M\delta_{\mathrm{eff}}/\pi^2$. The limit $M \to \infty$ at fixed level spacing δ_{eff} is taken at the end of the calculation. Substitution of Eq. (4.29) into the determinantal equation (4.27) gives a conventional eigenvalue equation [20],

$$\mathrm{Det}\left[E - H_{\mathrm{eff}}(B)\right] = 0, \tag{4.30}$$

$$H_{\mathrm{eff}}(B) = \begin{pmatrix} H_0(B) & 0 \\ 0 & -H_0^*(B) \end{pmatrix} - \mathcal{W}, \tag{4.31}$$

$$\mathcal{W} = \frac{\pi}{\cos u} \begin{pmatrix} WW^T \sin u & W\Omega(B)W^T \\ W\Omega^*(B)W^T & WW^T \sin u \end{pmatrix}. \tag{4.32}$$

We have abbreviated $u = E\tau_E/\hbar$.

The Hamiltonian $H_0(B)$ of the fictitious cavity has the Pandey-Mehta distribution [23],

$$P(H) \propto \exp\left(-\frac{\pi^2(1+b^2)}{4M\delta_{\mathrm{eff}}^2} \sum_{i,j=1}^{M} \left[(\mathrm{Re}H_{ij})^2 + b^{-2}(\mathrm{Im}H_{ij})^2\right]\right). \tag{4.33}$$

The parameter $b \in [0,1]$ measures the strength of the time-reversal symmetry breaking. It is related to the magnetic field by [9]

$$\frac{M}{N_{\rm eff}} b^2 = \frac{1}{8}(B/B_0)^2. \tag{4.34}$$

The ensemble averaged density of states $\rho_{\rm eff}(E)$ is obtained from the Green function,

$$\rho_{\rm eff}(E) = -\frac{1}{\pi}{\rm Im}{\rm Tr}\left(1 + \frac{d\mathcal{W}}{dE}\right)\mathcal{G}(E + i0^+), \tag{4.35}$$

$$\mathcal{G}(z) = \langle (z - H_{\rm eff})^{-1} \rangle, \tag{4.36}$$

where the average $\langle \cdots \rangle$ is taken with the distribution (4.33). Using the results of Refs. [9, 20] we obtain a self-consistency equation for the trace of the ensemble averaged Green function,

$$G = \begin{pmatrix} G_{11} & G_{12} \\ G_{21} & G_{22} \end{pmatrix} = \frac{\delta}{\pi} \begin{pmatrix} {\rm Tr}\,\mathcal{G}_{11} & {\rm Tr}\,\mathcal{G}_{12} \\ {\rm Tr}\,\mathcal{G}_{21} & {\rm Tr}\,\mathcal{G}_{22} \end{pmatrix}. \tag{4.37}$$

The four blocks refer to the block decomposition (4.31) of the effective Hamiltonian. The self-consistency equation reads

$$G_{11} = G_{22}, \qquad G_{12}G_{21} = 1 + G_{11}^2, \tag{4.38}$$

$$0 = N_{\rm eff}\left(\frac{E}{2E_T} - \left(\frac{B}{B_0}\right)^2 \frac{G_{11}}{2}\right) G_{12} + \sum_{j=1}^{N_{\rm eff}} \frac{e^{2i\phi_j} G_{11} + G_{12}\sin u}{\frac{1}{2}\left[e^{-2i\phi_j} G_{12} + e^{2i\phi_j} G_{21}\right] + \cos u + G_{11}\sin u}, \tag{4.39}$$

$$0 = N_{\rm eff}\left(\frac{E}{2E_T} - \left(\frac{B}{B_0}\right)^2 \frac{G_{11}}{2}\right) G_{21} + \sum_{j=1}^{N_{\rm eff}} \frac{e^{-2i\phi_j} G_{11} + G_{21}\sin u}{\frac{1}{2}\left[e^{-2i\phi_j} G_{12} + e^{2i\phi_j} G_{21}\right] + \cos u + G_{11}\sin u}, \tag{4.40}$$

with the Thouless energy $E_T = \hbar/2\tau_D$.

From Eq. (4.35) we find the density of states

$$\rho_{\rm eff}(E) = -\frac{2}{\delta_{\rm eff}}{\rm Im}\Big[G_{11} + \frac{\tau_E}{\tau_D \cos u} \times \sum_{j=1}^{N_{\rm eff}} \frac{G_{11} + \frac{1}{2}\sin u \left(G_{21} e^{2i\phi_j} + G_{12} e^{-2i\phi_j}\right)}{\cos u + G_{11}\sin u + \frac{1}{2} G_{12} e^{-2i\phi_j} + \frac{1}{2} G_{21} e^{2i\phi_j}} \Big]. \tag{4.41}$$

Because $N_{\rm eff} \gg 1$, we may replace in Eqs. (4.38–4.41) the sum $\sum_j f(\phi_j)$ by $\int d\phi\, P(\phi)$, with $P(\phi)$ given by Eq. (4.23). In the next section we will compare the density of states obtained from (4.38–4.41) with a fully quantum mechanical calculation. In this section we discuss the low and high energy asymptotics of the density of states.

In the limit $E \to \infty$, $E \ll \Delta$ we find from Eqs. (4.38–4.40) that $G_{12} = G_{21} \propto 1/E \to 0$ while $G_{11} \to -i$. Substituting this into Eq. (4.41) we obtain the high energy limit,

$$\lim_{\substack{E\to\infty \\ E\ll\Delta}} \rho_{\rm eff}(E) = \frac{2}{\delta_{\rm eff}}\left(1+\frac{\tau_E}{\tau_D}\right) = \frac{2}{\delta} e^{-\tau_E/\tau_D}\left(1+\frac{\tau_E}{\tau_D}\right). \tag{4.42}$$

This limit is larger than $2/\delta_{\rm eff}$ because of the contribution from states in the lead, cf. Fig. 4.6. Comparison with Eq. (4.15) shows that the total density of states,

$$\rho(E) = \rho_{\rm eff}(E) + \rho_{\rm ad}(E), \tag{4.43}$$

tends to $2/\delta$ for high energies, as it should be.

At low energies the density of states $\rho_{\rm eff}(E)$ obtained from the effective RMT vanishes for $E < E_{\rm gap}^{\rm eff}$. In the limit $\tau_E \gg \tau_D$ the lowest level in the effective cavity is determined by the fictitious lead with return time τ_E. This gives the same gap as for adiabatic quantization,

$$E_{\rm gap}^{\rm eff} = E_{\rm gap}^{\rm ad} = \frac{\hbar}{\tau_E}\left(\frac{\pi}{2} - 2\phi_{\max}\right) \approx \frac{\pi\hbar}{2\tau_E} - e\nu_F LB, \tag{4.44}$$

cf. Eq. (4.12). The two critical magnetic fields $B_c^{\rm eff}$ and $B_c^{\rm ad}$ coincide in this limit,

$$B_c^{\rm eff} = B_c^{\rm ad} \simeq \frac{\pi\hbar}{2\tau_E e\nu_F L} \simeq B_0\sqrt{\frac{\tau_D L}{\nu_F \tau_E^2}}, \text{ if } \tau_E \gg \tau_D, \tag{4.45}$$

cf. Eq. (4.13). In the opposite regime of small τ_E we find a critical field of

$$B_c^{\rm eff} = B_0\left(1 - \frac{c\tau_E}{8\tau_D}\right), \text{ if } \tau_E \ll \sqrt{L\tau_D/\nu_F}, \tag{4.46}$$

which is smaller than $B_c^{\rm ad}$ so $B_c = B_c^{\rm eff}$. In the intermediate regime $\sqrt{L\tau_D/\nu_F} \lesssim \tau_E \lesssim \tau_D$, the critical field B_c is given by

$$B_c = \min\left(B_c^{\rm eff}, B_c^{\rm ad}\right). \tag{4.47}$$

We do not have an analytical formula for $B_c^{\rm eff}$ in this intermediate regime, but we will show in the next section that $B_c^{\rm ad}$ drops below $B_c^{\rm eff}$ so that $B_c = B_c^{\rm ad}$.

4.4 Comparison with quantum mechanical model

In this section we compare our quasiclassical theory with a quantum mechanical model of the Andreev billiard. The model we use is the Andreev kicked rotator introduced in Ref. [6]. We include the magnetic field into the model using the three-kick representation of Ref. [24], to break time-reversal-symmetry at both the quantum mechanical and the classical level. The basic equations of the model are summarized in Appendix 4.A.

In Fig. 4.7 we show the ensemble averaged density of states of the Andreev kicked rotator and we compare it with the theoretical result (4.43). The Ehrenfest time is given by [5, 6]

$$\tau_E = \lambda^{-1}\left[\ln\left(N^2/M\right) + \mathcal{O}(1)\right], \tag{4.48}$$

with M the dimensionality of the Floquet matrix. We neglect the correction term of order unity. The mean dwell time is $\tau_D = (M/N)\tau_0$ and the level spacing is $\delta = (2\pi/M)\hbar/\tau_0$, with τ_0 the stroboscopic time. The relation between B/B_0 and the parameters of the kicked rotator is given by Eq. (4.60).

In Fig. 4.7a $\tau_E \ll \tau_D$ and we recover the RMT result of Ref. [9]. The density of states is featureless with a shallow maximum just above the gap. In Figs. 4.7b, c, d τ_E and τ_D are comparable. Now the spectrum consists of both adiabatic levels (return time $T < \tau_E$) as well as effective RMT levels (return time $T > \tau_E$). The adiabatic levels cluster in peaks, while the effective RMT forms the smooth background, with a pronounced bump above the gap.

The peaks in the excitation spectrum of the Andreev kicked rotator appear because the return time T in Eq. (4.14) is a multiple of the stroboscopic time τ_0 [6]. The peaks are broadened by the magnetic field and they acquire side peaks, due to the structure of the area distribution $P(A|T)$ for T a small multiple of τ_0. This is illustrated in Fig. 4.8 for the central peak of Fig. 4.7. The distribution was calculated from the classical map (4.61) associated with the quantum kicked rotator. The same map gave the coefficient $c = 0.55$ appearing in Eq. (4.23).

In Fig. 4.9 we have plotted the critical magnetic field B_c at which the gap closes, as a function of the Ehrenfest time. For $\tau_E \ll \tau_D$ the Andreev kicked rotator gives a value for B_c close to the prediction B_0 of RMT, cf. Eq. (4.60). With increasing τ_E we find that B_c decreases quite strongly. In

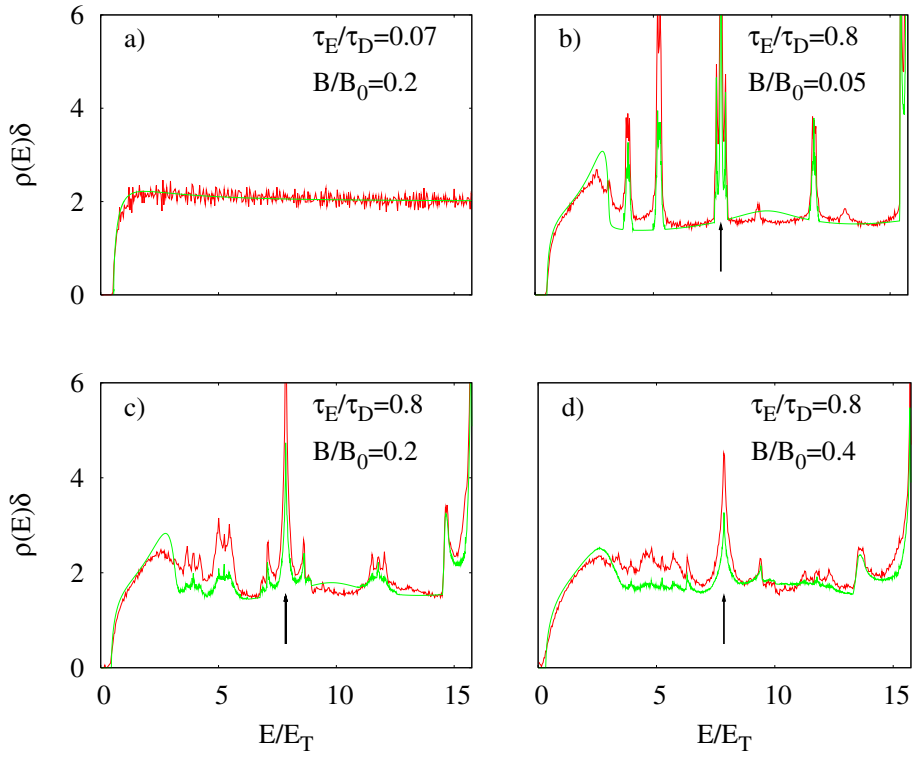

Figure 4.7: Ensemble averaged density of states $\rho(E)$ of the Andreev kicked rotator. The dark (red) curves show the numerical results from the fully quantum mechanical model, while the light (green) curves are obtained from Eq. (4.43) with input from the classical limit of the model. The energy is scaled by the Thouless energy $E_T = \hbar/2\tau_D$ and the density is scaled by the level spacing δ of the isolated billiard. The parameters of the kicked rotator are $M = 2048$, $N = 204$, $q = 0.2$, $K = 200$ in panel a and $M = 16384$, $N = 3246$, $q = 0.2$, $K = 14$ in panels b, c, d. The three-peak structure indicated by the arrow in panels b, c, d is explained in Fig. 4.8.

the figure we also show the critical magnetic fields $B_c^{\rm ad}$ for adiabatic levels and $B_c^{\rm eff}$ for effective RMT. The former follows from Eqs. (4.13) and (4.64),

$$B_c^{\rm ad} = \frac{\pi}{4} B_0 \sqrt{\frac{2\tau_D \tau_0}{\tau_E^2}}, \tag{4.49}$$

and the latter from solving Eqs. (4.38–4.40) numerically. As already an-

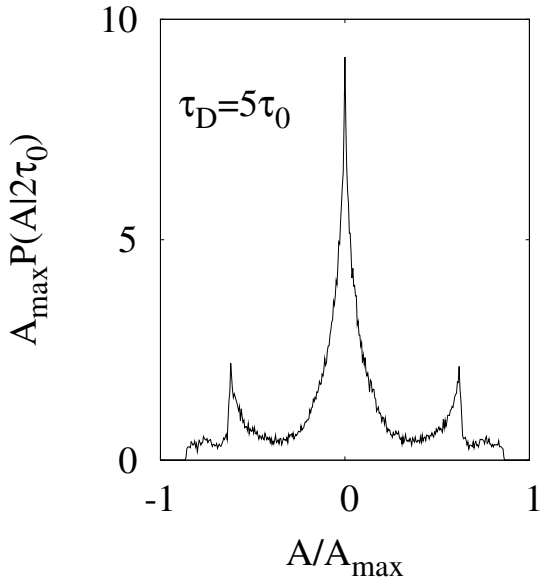

Figure 4.8: Conditional distribution $P(A|T)$ of directed areas A enclosed by classical trajectories with $T = 2\tau_0$, for $K = 14$, $q = 0.2$ and $\tau_D = 5\tau_0$. The distribution was obtained from the classical map (4.61) at $\gamma = 0$. Trajectories with $T = 2\tau_0$ give rise to a peak in the density of states centered around $E/E_T = (m + 1/2)\pi\hbar/2\tau_0$, cf. Eq. (4.14). On the energy scale of Fig. 4.7 only the peak with $m = 0$ can be seen, at $E/E_T = 2.5\,\pi \approx 7.9$. In a magnetic field this peak broadens and it obtains the side peaks of $P(A|2\tau_0)$.

nounced in the previous section, $B_c^{\rm ad}$ drops below $B_c^{\rm eff}$ with increasing τ_E, which means that the lowest level $E_{\rm gap}$ is an adiabatic level corresponding to a return time $T < \tau_E$. The critical magnetic field is the smallest value of $B_c^{\rm eff}$ and $B_c^{\rm ad}$, as indicated by the solid curve. The data of the Andreev kicked rotator follows the trend of the quasiclassical theory, although quite substantial discrepancies remain. Part of these discrepancies can be attributed to the correction term of order unity in Eq. (4.48), as shown by the open circles in Fig. 4.9.

In the regime of fully broken time-reversal-symmetry the distribution of eigenvalues is determined by the Laguerre unitary ensemble of RMT [25, 26]. The ensemble averaged density of states vanishes quadratically

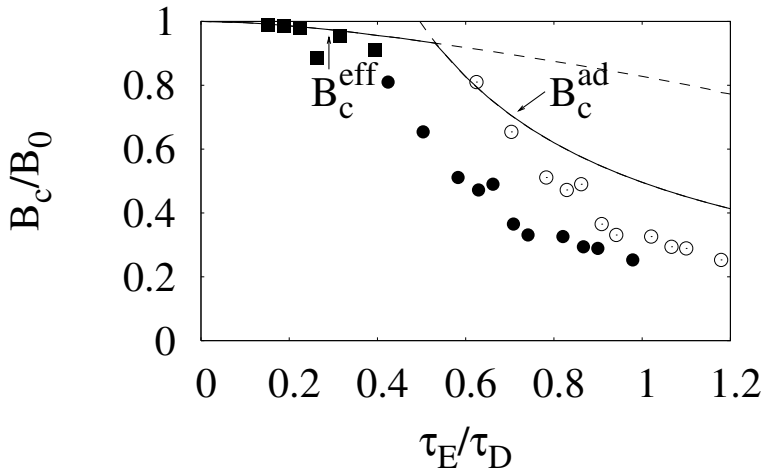

Figure 4.9: Critical magnetic field B_c of the Andreev kicked rotator as a function of the Ehrenfest time. The Ehrenfest time $\tau_E = \lambda^{-1} \ln(N^2/M)$ is changed by varying M and N while keeping $q = 0.2$ and $\tau_D/\tau_0 = M/N = 5$ constant. For the closed circles the kicking strength $K = 14$, while for the squares from left to right $K = 4000$, 1000, 400, 200, 100, 50. The solid curve is the quasiclassical prediction (4.47). The open circles are obtained from the closed circles by the transformation $\lambda\tau_E \to \lambda\tau_E + 1.75$, allowed by the terms of order unity in Eq. (4.48).

near zero energy, according to

$$\rho(E) = \frac{2}{\delta}\left(1 - \frac{\sin(4\pi E/\delta)}{4\pi E/\delta}\right). \tag{4.50}$$

In Fig. 4.10 we show the results for the Andreev kicked rotator in this regime and we find a good agreement with Eq. (4.50) for $\tau_E \ll \tau_D$. We did not investigate the τ_E dependence in this regime.

4.5 Conclusion

We have calculated the excitation spectrum of an Andreev billiard in a magnetic field, both using a quasiclassical and a fully quantum mechanical approach. The quasiclassical theory needs as input the classical dis-

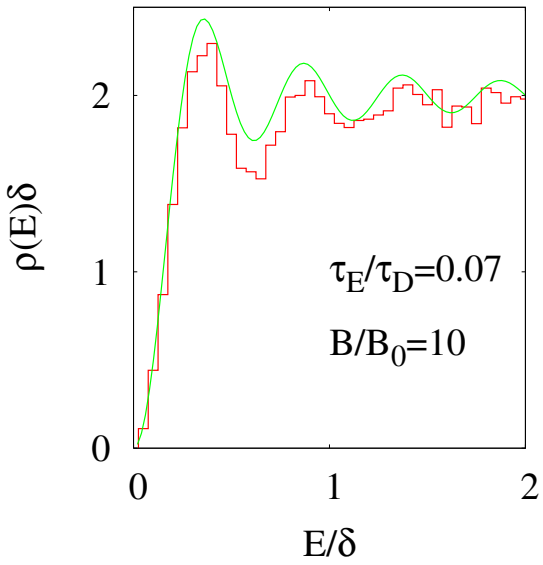

Figure 4.10: Ensemble averaged density of states of the Andreev kicked rotator for fully broken TRS. The histogram shows the numerical results, while the curve is the theoretical prediction (4.50) of the Laguerre unitary ensemble. Both the energy and the density of states are scaled by the level spacing δ of the isolated billiard. The parameters of the kicked rotator are $M = 2048$, $N = 204$, $q = 0.2$, while K was varied between 200 and 250 to obtain an ensemble average.

tribution of times T between Andreev reflections and directed areas A enclosed in that time T. Times T smaller than the Ehrenfest time τ_E are quantized via the adiabatic invariant and times $T > \tau_E$ are quantized by an effective random-matrix theory with τ_E-dependent parameters. This separation of phase space into two parts, introduced in chapter 2, has received much theoretical support in the context of transport, see chapter 5 and Refs. [24,27–31]. The present chapter shows that it can be succesfully used to describe the consequences of time-reversal symmetry breaking on the superconducting proximity effect.

The adiabatically quantized and effective RMT spectra each have an excitation gap which closes at different magnetic fields. The critical magnetic field B_c of the Andreev billiard is the smallest of the two values B_c^{ad}

and $B_c^{\rm eff}$. For relatively small Ehrenfest time $\tau_E \ll \tau_D$ the critical field $B_c^{\rm eff}$ from effective RMT is smaller than the critical field $B_c^{\rm ad}$ of the adiabatic levels, so $B_c = B_c^{\rm eff}$. This value $B_c^{\rm eff}$ is smaller than the value B_0 of conventional RMT [9], because of the τ_E dependence of the parameters in effective RMT. For $\tau_E \gg \tau_D$ the two fields $B_c^{\rm ad}$ and $B_c^{\rm eff}$ coincide, but in an intermediate regime of comparable τ_E and τ_D the adiabatic value $B_c^{\rm ad}$ drops below the effective RMT value $B_c^{\rm eff}$. This is indeed what we have found in the specific model that we have investigated, the Andreev kicked rotator [6]. The lowest level has $T \simeq \tau_E$ for sufficiently large τ_E and B. This is a novel feature of the Andreev billiard in a magnetic field: For unbroken time-reversal symmetry the lowest level always corresponds to longer trajectories $T > \tau_E$, and thus cannot be obtained by adiabatic quantization (chapter 2).

4.A Andreev kicked rotator in a magnetic field

The Andreev kicked rotator in zero magnetic field was introduced in Ref. [6]. Here we give the extension to non-zero magnetic field used in Sec. 4.4. We start from the kicked rotator with broken TRS but without the superconductor. The kicked rotator provides a stroboscopic description of scattering inside a quantum dot. The propagation of a state from time t to time $t+\tau_0$ is given by the $M \times M$ unitary Floquet operator F with matrix elements [24]

$$F_{mn} = \left(X\Pi Y^* \Pi Y \Pi X\right)_{mn}. \tag{4.51}$$

The three matrices X, Y, and Π are defined by

$$Y_{mn} = \delta_{mn} e^{i(M\gamma/6\pi)\cos(2\pi m/M)}, \tag{4.52}$$

$$X_{mn} = \delta_{mn} e^{-i(M/12\pi)V(2\pi m/M)}, \tag{4.53}$$

$$\Pi_{mn} = M^{-1/2} e^{-i\pi/4} \exp\left[i(\pi/M)(m-n)^2\right]. \tag{4.54}$$

The potential

$$V(\theta) = K\cos(\pi q/2)\cos(\theta) + \frac{K}{2}\sin(\pi q/2)\sin(2\theta) \tag{4.55}$$

breaks the parity symmetry for $q \neq 0$. Time-reversal symmetry is broken by the parameter γ. For kicking strengths $K \gtrsim 7$ the classical dynamics of the kicked rotator is chaotic.

The Floquet operator (4.51) describes electron excitations above the Fermi level. The hole excitations below the Fermi level are described by the Floquet operator F^*. Electrons and holes are coupled by Andreev reflection at the superconductor. The $N \times M$ matrix P, with elements

$$P_{nm} = \delta_{nm} \times \begin{cases} 1 \text{ if } L_0 \leq n \leq L_0 + N - 1 \\ 0 \text{ otherwise} \end{cases}, \tag{4.56}$$

projects onto the contact with the superconductor. The integer L_0 indicates the location of the contact and N is its width, in units of $\lambda_F/2$. We will perform ensemble averages by varying L_0. The process of Andreev reflection is described by the $2M \times 2M$ matrix

$$\mathcal{P} = \begin{pmatrix} 1 - P^T P & -iP^T P \\ -iP^T P & 1 - P^T P \end{pmatrix}. \tag{4.57}$$

The Floquet operator for the Andreev kicked rotator is constructed from the two matrices F and $\mathcal{P}$ [6],

$$\mathcal{F} = \mathcal{P}^{1/2} \begin{pmatrix} F & 0 \\ 0 & F^* \end{pmatrix} \mathcal{P}^{1/2}. \tag{4.58}$$

The $2M \times 2M$ unitary matrix $\mathcal{F}$ can be diagonalized efficiently using the Lanczos technique in combination with the fast-Fourier-transform algorithm [32]. The eigenvalues $e^{i\varepsilon_m}$ define the quasi-energies $\varepsilon_m \in [0, 2\pi]$. One gap is centered around $\varepsilon = 0$ and another gap around $\varepsilon = \pi$. For $N \ll M$ the two gaps are decoupled and we can study the gap around $\varepsilon = 0$ by itself.

The correspondence between the TRS-breaking parameter γ of the kicked rotator and the Pandey-Mehta parameter b for $K \ll 1$ is given by [24]

$$\lim_{K\to\infty} b\sqrt{M_H} = \frac{\gamma M^{3/2}}{12\pi}. \tag{4.59}$$

Here M_H is the size of the Pandey-Mehta Hamiltonian [23]. Comparison with Eq. (4.34) gives the relation between γ and the magnetic field B,

$$\frac{M^{3/2}}{N^{1/2}}\gamma = \sqrt{\frac{\tau_D}{\tau_0}} M\gamma = 3\pi\sqrt{2}\frac{B}{B_0}. \tag{4.60}$$

In RMT the gap closes when $B = B_0$, so when $\gamma = \gamma_0 = 3\pi M^{-1}\sqrt{2\tau_0/\tau_D}$.

For the quasiclassical theory we need the classical map associated with the Floquet operator (4.58). The classical phase space consists of the torus $0 \le \theta \le 2\pi$, $0 \le p \le 6\pi$. The classical map is described by a set of equations that map initial coordinates (θ, p) onto final coordinates (θ', p') after one period τ_0 [24],

$$\begin{aligned}
\theta_1 &= \theta \pm p/3 - V'(\theta)/6 - 2\pi\sigma_{\theta_1}, \\
p_1 &= p \mp \gamma \sin(\theta_1) \mp V'(\theta)/2 - 6\pi\sigma_{p_1}, \\
\theta_2 &= \theta_1 \pm p_1/3 - 2\pi\sigma_{\theta_2}, \\
p_2 &= p_1 - 6\pi\sigma_{p_2}, \\
\theta' &= \theta_2 \pm p_2/3 + \gamma \sin(\theta_2)/3 - 2\pi\sigma_{\theta'}, \\
p' &= p_2 \pm \gamma \sin(\theta_2) \mp V'(\theta')/2 - 6\pi\sigma'_p.
\end{aligned} \tag{4.61}$$

The upper/lower signs correspond to electron/hole dynamics and $V'(\theta) = dV/d\theta$. The integers σ_θ and σ_p are the winding numbers of a trajectory on the torus.

The directed area enclosed by a classical trajectory between Andreev reflections can be calculated from the difference in classical action between two trajectories related by TRS, one with $\gamma = 0$ and one with infinitesimal γ. To linear order in γ the action difference ΔS acquired after one period is given by [24]

$$\Delta S = \gamma (\cos\theta_1 - \cos\theta_2). \tag{4.62}$$

The effective Planck constant of the kicked rotator is $\hbar_{\rm eff} = 6\pi/M$, so we may obtain the increment in directed area ΔA corresponding to ΔS from

$$\frac{e}{\hbar} B \Delta A = \frac{\Delta S}{\hbar_{\rm eff}} = \frac{M}{6\pi} \gamma (\cos\theta_1 - \cos\theta_2). \tag{4.63}$$

Since $|\cos\theta_1 - \cos\theta_2| < 2$, the maximum directed area $A_{\rm max}$ acquired after T/τ_0 periods is

$$A_{\rm max} = 2 \frac{T}{\tau_0} \frac{\hbar}{eB_0} \sqrt{\frac{\tau_0}{2\tau_D}}. \tag{4.64}$$

Bibliography

[1] J. A. Melsen, P. W. Brouwer, K. M. Frahm, and C. W. J. Beenakker, Europhys. Lett. **35**, 7 (1996).

[2] A. Lodder and Yu. V. Nazarov, Phys. Rev. B **58**, 5783 (1998).

[3] D. Taras-Semchuk and A. Altland, Phys. Rev. B **64**, 014512 (2001).

[4] İ. Adagideli and C. W. J. Beenakker, Phys. Rev. Lett. **89**, 237002 (2002).

[5] M. G. Vavilov and A. I. Larkin, Phys. Rev. B **67**, 115335 (2003).

[6] Ph. Jacquod, H. Schomerus, and C. W. J. Beenakker, Phys. Rev. Lett. **90**, 207004 (2003).

[7] A. Kormányos, Z. Kaufmann, C. J. Lambert, and J. Cserti, Phys. Rev. B **70**, 052512 (2004).

[8] C. W. J. Beenakker, Lect. Notes Phys. **667**, 131 (2005); cond-mat/0406018.

[9] J. A. Melsen, P. W. Brouwer, K. M. Frahm, and C. W. J. Beenakker, Physica Scripta **69**, 223 (1997).

[10] I. Kosztin, D. L. Maslov, and P. M. Goldbart, Phys. Rev. Lett. **75**, 1735 (1995).

[11] J. Wiersig, Phys. Rev. E **65**, 036221 (2002).

[12] N. G. Fytas, F. K. Diakonos, P. Schmelcher, M. Scheid, A. Lassl, K. Richter, and G. Fagas, cond-mat/0504322.

[13] J. V. José and E. J. Saletan, *Classical Dynamics* (Cambridge University Press, Cambridge, 1998).

[14] M. C. Gutzwiller, *Chaos in Classical and Quantum Mechanics* (Springer, Berlin, 1990).

[15] The shift by $1/2$ in Eqs. (4.5a) and (4.5b) accounts for two phase shifts of $\pi/2$ incurred at each Andreev reflection and at each turning point, respectively; turning points do not contribute a net phase shift to Eq. (4.5a) because the phase shifts in the electron and hole sheets cancel.

[16] In chapter 5 the fluctuations of T around $\bar{T}$ within a single scattering band are estimated at $\delta T \simeq W/\nu_F \ll \tau_D$, and similarly we estimate that $\delta A \simeq WL \ll \nu_F \tau_D L$.

[17] W. Ihra, M. Leadbeater, J. L. Vega, and K. Richter, Eur. Phys. J. B **21**, 425 (2001).

[18] H. U. Baranger, R. A. Jalabert, and A. D. Stone, Chaos **3**, 665 (1993).

[19] C. W. J. Beenakker, Phys. Rev. Lett. **67**, 3836 (1991).

[20] P. W. Brouwer and C. W. J. Beenakker, Chaos, Solitons and Fractals **8**, 1249 (1997).

[21] T. Guhr, A. Müller-Groeling, and H. A. Weidenmüller, Phys. Rep. **299**, 189 (1998).

[22] C. W. J. Beenakker, Rev. Mod. Phys. **69**, 731 (1997).

[23] M. L. Mehta, *Random Matrices* (Academic, New York, 1991).

[24] J. Tworzydło, A. Tajic, and C. W. J. Beenakker, Phys. Rev. B **70**, 205324 (2004).

[25] A. Altland and M. R. Zirnbauer, Phys. Rev. Lett. **76**, 3420 (1996).

[26] K. M. Frahm, P. W. Brouwer, J. A. Melsen, and C. W. J. Beenakker, Phys. Rev. Lett. **76**, 2981 (1996).

[27] J. Tworzydło, A. Tajic, H. Schomerus, and C. W. J. Beenakker, Phys. Rev. B **68** 115313 (2003).

[28] J. Tworzydło, A. Tajic, and C. W. J. Beenakker, Phys. Rev. B **69**, 165318 (2004).

[29] Ph. Jacquod and E. V. Sukhorukov, Phys. Rev. Lett. **92**, 116801 (2004).

[30] J. Tworzydło, A. Tajic, H. Schomerus, P. W. Brouwer, and C. W. J. Beenakker, Phys. Rev. Lett. **93**, 186806 (2004).

[31] R. S. Whitney and Ph. Jacquod, Phys. Rev. Lett. **94**, 116801 (2005).

[32] R. Ketzmerick, K. Kruse, and T. Geisel, Physica D **131**, 247 (1999).

Chapter 5

Noiseless scattering states in a chaotic cavity

Shot noise can distinguish deterministic scattering, characteristic for particles, from stochastic scattering, characteristic for waves. Particle dynamics is deterministic: A given initial position and momentum fixes the entire trajectory. In particular, it fixes whether the particle will be transmitted or reflected, so the scattering is noiseless. Wave dynamics is stochastic: The quantum uncertainty in position and momentum introduces a probabilistic element into the dynamics, so it is noisy.

The suppression of shot noise in a conductor with deterministic scattering was predicted many years ago from this qualitative argument [1]. A better understanding, and a quantitative description, of how shot noise measures the transition from particle to wave dynamics in a chaotic quantum dot was put forward by Agam, Aleiner, and Larkin [2], and developed further in Ref. [3]. The key concept is the Ehrenfest time τ_E, which is the characteristic time scale of quantum chaos [4]. The noise power $S \propto \exp(-\tau_E/\tau_D)$ was predicted to vanish exponentially with the ratio of τ_E and the mean dwell time $\tau_D = \pi\hbar/N\delta$ in the quantum dot (with δ the level spacing and N the number of modes in each of the two point contacts through which the current is passed). A recent measurement of the N dependence of S is consistent with this prediction for $\tau_E < \tau_D$, although an alternative explanation in terms of short-range impurity scattering describes the data equally well [5].

The theory of Ref. [2] introduces the stochastic element by means of

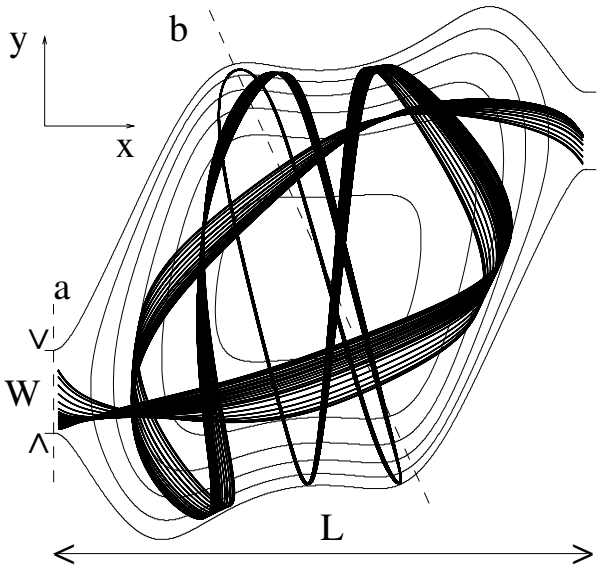

Figure 5.1: Selected equipotentials of the electron billiard. The outer equipotential is at E_F, the other equipotentials are at increments of $0.19\,E_F$. Dashed lines a and b show the sections described in the text. Also shown is a flux tube of transmitted trajectories, all originating from a single closed contour in a transmission band, representing the spatial extension of a fully transmitted scattering state. The flux tube is wide at the two openings and squeezed inside the billiard.

long-range impurity scattering and adjusts the scattering rate so as to mimic the effect of a finite Ehrenfest time. Here we take the alternative approach of explicitly constructing noiseless channels in a chaotic quantum dot. These are scattering states which are either fully transmitted or fully reflected in the semiclassical limit. They are not described by random-matrix theory [6]. By determining what fraction of the available channels is noiseless, we can deduce a precise upper bound for the shot noise power. A random-matrix conjecture for the remaining noisy channels gives an explicit form of $S(N)$. We find that the onset of the classical suppression of the noise is described not only by the Ehrenfest time, but by the difference of τ_E and the ergodic time $\tau_{\rm erg}$, which we introduce and calculate in this chapter. The resulting nonlinear dependence of $\ln S$ on N may help to distinguish between the competing explanations of the ex-

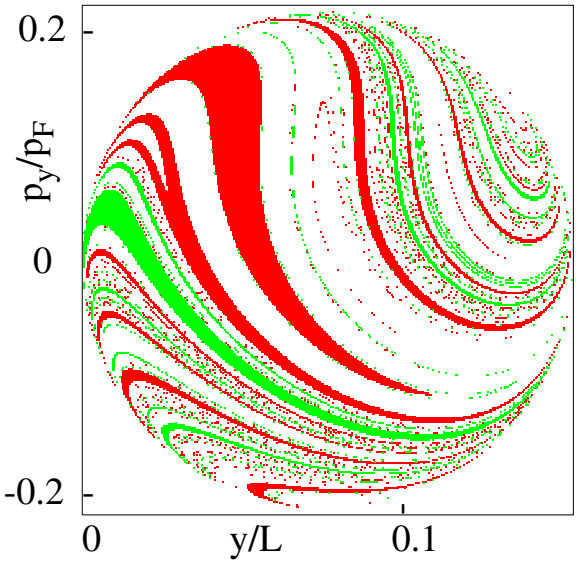

Figure 5.2: Section of phase space at $p_x = \sqrt{p_F^2 - p_y^2}$ and $x = 0$, corresponding to line a in Fig. 5.1. Each dot in this surface of section is the starting point of a classical trajectory that is transmitted through the lead at $x = L$ (black/red), or reflected back through $x = 0$ (gray/green). The points lie in narrow bands. Only the trajectories with dwell time $t < 12mL/p_F$ are shown.

perimental data [5].

We illustrate the construction of noiseless scattering states for the two-dimensional billiard with smooth confining potential $U(x, y)$ shown in Fig. 5.1. The outer equipotential defines the area in the $x - y$ plane which is classically accessible at the Fermi energy $E_F = p_F^2/2m$ (with $p_F = \hbar k_F$ the Fermi momentum). The motion in the closed billiard is chaotic with Lyapunov exponent λ. We assume the billiard to be connected at $x = 0$ and $x = L$ by two similar point contacts to leads of width W extended along the $\pm x$-direction.

The beam of electrons injected through a point contact into the billiard has cross-section W and transverse momenta in the range $(-p_W, p_W)$. The number of channels $N \simeq p_W W/\hbar$ in the lead is much smaller than the number of channels $M \simeq p_F L/\hbar$ supported by a typical cross-section of the

billiard. While $W/L \ll 1$ in general, the ratio p_W/p_F depends on details of the potential near the point contact. If $p_W/p_F \ll 1$ one speaks of a collimated beam. This is typical for a smooth potential, while a hard-wall potential typically has $p_W \simeq p_F$ (no collimation). We define $r_{\min} = \min(W/L, p_W/p_F)$ and $r_{\max} = \max(W/L, p_W/p_F)$.

The classical phase space is four-dimensional. By restricting the energy to E_F and taking $x = 0$ we obtain the two-dimensional section of phase space shown in Fig. 5.2. The accessible values of y and p_y lie in a disc-shaped region of area $O_{\rm tot} = Nh$ in this surface of section. Up to factors of order unity, the disk has width $r_{\min}$ and length $r_{\max}$ (if coordinate and momentum are measured in units of L and p_F, respectively). In Fig. 5.2 one has $r_{\min} \simeq r_{\max}$. Each point in the disc defines a classical trajectory that enters the billiard (for positive p_x) and then leaves the billiard either through the same lead (reflection) or through the other lead (transmission). The points lie in narrow bands, which we will refer to as "transmission bands" and "reflection bands".

It is evident from Fig. 5.2 that the area $O_{{\rm band},j}$ enclosed by a typical transmission (or reflection) band j is much less than $O_{\rm tot}$. For an estimate we consider the time $T(y, p_y)$ that elapses before transmission. Let $\bar{T}_j$ be the dwell time averaged over the starting points y, p_y in a single band. The fluctuations of T around the average are of the order of the time $T_W \simeq mW/p_W$ to cross the point contact, which is typically $\ll \bar{T}_j$. As we will see below, the area of the band decreases with $\bar{T}_j$ as

$$O_{{\rm band},j} \simeq O_0 \exp(-\lambda \bar{T}_j) \;\text{ if }\; \bar{T}_j \gg 1/\lambda, T_W. \tag{5.1}$$

The prefactor $O_0 = O_{\rm tot} r_{\min}/r_{\max}$ depends on the degree of collimation. In chapter 2 the symmetric case $r_{\min} = r_{\max}$ was assumed, when $O_0 = O_{\rm tot}$.

We now proceed to the construction of fully transmitted scattering states. To this end we consider a closed contour C within a transmission band j. The starting points on the contour define a family of trajectories that form a flux tube inside the billiard (see Fig. 5.1). The semiclassical wave function

$$\psi(x, y) = \sum_\sigma \sqrt{\rho_\sigma(x, y)}\, \exp[i S_\sigma(x, y)/\hbar] \tag{5.2}$$

is determined as usual from the action S_σ and density ρ_σ that solve the Hamilton-Jacobi and continuity equations

$$|\nabla S|^2 = 2m(E_F - U), \;\; \nabla \cdot (\rho \nabla S) = 0. \tag{5.3}$$

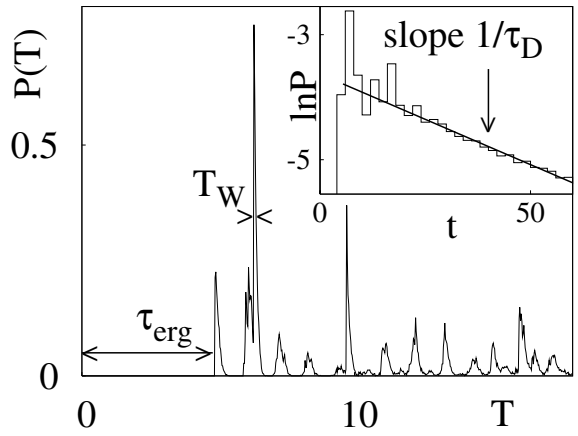

Figure 5.3: Dwell time distribution for the billiard of Fig. 5.1. Electrons at the Fermi energy are injected through the left lead. Time is in units of mL/p_F. Inset: the same data on a semilogarithmic scale with larger bin size of the histogram. Three characteristic time scales are seen: T_W, $\tau_{\rm erg}$, τ_D.

The action is multivalued and the index σ labels the different sheets. Typically, there are two sheets, one originating from the upper half of the contour C and one from the lower half.

The requirement that ψ is single-valued as one winds around the contour imposes a quantization condition on the enclosed area,

$$\oint_C p_y dy = (n + 1/2)h. \tag{5.4}$$

The increment $1/2$ accounts for the phase shift acquired at the two turning points on the contour. The quantum number $n = 0, 1, 2, \ldots$ is the channel index. The largest value of n occurs for a contour enclosing an area $O_{{\rm band},j}$. The number of transmission channels N_j within band j is therefore given by $O_{{\rm band},j}/h$, with an accuracy of order unity. In view of Eq. (5.1) we have

$$N_j \simeq (O_0/h)\exp(-\lambda \bar{T}_j), \quad \text{for } \bar{T}_j < \tau_E, \tag{5.5a}$$

$$N_j = 0, \quad \text{for } \bar{T}_j > \tau_E. \tag{5.5b}$$

The time

$$\tau_E = \lambda^{-1}\left[\ln(2O_0/h) + \mathcal{O}(1)\right] = \lambda^{-1}\left[\ln(N r_{\min}/r_{\max}) + \mathcal{O}(1)\right] \tag{5.6}$$

above which there are no fully transmitted channels is the Ehrenfest time of this problem.

By decomposing one of these N_j scattering states into a given basis of transverse modes in the lead one constructs an eigenvector of the transmission matrix product $tt^\dagger$. The corresponding eigenvalue $\mathcal{T}_{j,n}$ equals unity with exponential accuracy in the semiclassical limit $n \gg 1$. Because of the degeneracy of this eigenvalue any linear combination of eigenvectors is again an eigenvector. This manifests itself in our construction as an arbitrariness in the choice of C.

We observe in Fig. 5.1 that the spatial density profile $\rho(x, y)$ of a fully transmitted scattering state is highly non-uniform. The flux tube is broad (width of order W) at the two openings, but is squeezed down to very small width inside the billiard. A similar effect was noted in chapter 2 for the excited states of an Andreev billiard. Following the same argument we estimate the minimal width of the flux tube as $W_{\min} \simeq L\sqrt{N_j/k_F L}$.

The total number

$$N_{cl} = \sum_j N_j = N \int_0^{\tau_E} P(T)\,dT \tag{5.7}$$

of fully transmitted and reflected channels is determined by the dwell time distribution $P(T)$ [7]. Fig. 5.3 shows this distribution in our billiard. One sees three different time scales. The narrow peaks represent individual transmission (reflection) bands. They consist of an abrupt jump followed by an exponential decay with time constant T_W. These exponential tails correspond to the borders of the bands, where the trajectory bounces many times between the sides of the point contact. If we smooth $P(T)$ over such short time intervals, an exponential decay with time constant $\tau_D = \pi\hbar/N\delta$ is obtained (inset). The decay starts at the so called "ergodic time" $\tau_{\rm erg}$. There are no trajectories leaving the cavity for $T < \tau_{\rm erg}$. So the smoothed dwell time distribution has the form.

$$P(T) = \tau_D^{-1} \exp[(\tau_{\rm erg} - T)/\tau_D]\,\theta(T - \tau_{\rm erg}), \tag{5.8}$$

with $\theta(x)$ the unit step function.

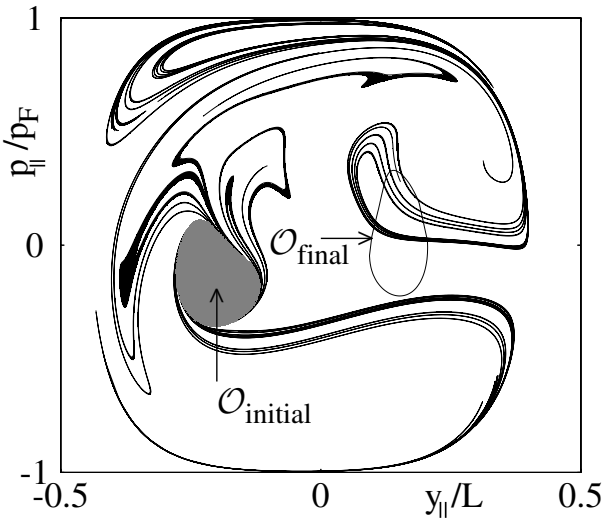

Figure 5.4: Section of phase space in the middle of the billiard, along line b in Fig. 5.1. The subscript $\|$ indicates the component of coordinate and momentum along this line. Elongated black areas $\mathcal{O}_j$ show the positions of the 5-th crossing of the injected beam with this surface of section. The area $\mathcal{O}_{\text{initial}}$ is the position of the first crossing. Points inside $\mathcal{O}_{\text{final}}$ leave the billiard without further crossing of line b. For times less than the ergodic time τ_{erg} there is no intersection between $\mathcal{O}_j$ and $\mathcal{O}_{\text{final}}$.

In order to find τ_{erg} we consider Fig. 5.4, where the section of phase space along a cut through the middle of the billiard is shown (line b in Fig. 5.1). It is convenient to measure the momentum and coordinate along b in units of p_F and L. The injected beam crosses the section for the first time over an area $\mathcal{O}_{\text{initial}}$ of size $r_{\max} \times r_{\min} = hN/p_F L$. (Fig. 5.4 has $r_{\min} \simeq r_{\max}$, but the estimates hold for any $r_{\min} < r_{\max} < 1$.) Further crossings consist of increasingly more elongated areas. The fifth crossing is shown in Fig. 5.4. The flux tube intersects line b in a few disjunct areas $\mathcal{O}_j$, of width $r_{\min} e^{-\lambda t}$ and total length $r_{\max} e^{\lambda t}$. (Due to conservation of the integral $\oint \mathbf{p} \cdot d\mathbf{r}$ enclosing the flux tube, the total area $\sum_j \mathcal{O}_j$ decreases only when particles leave the billiard.) The typical separation of adjacent areas is $(r_{\max} e^{\lambda t})^{-1}$. To leave the billiard (through the right contact) without further crossing of b a particle should pass through an area $\mathcal{O}_{\text{final}} \simeq r_{\max} \times$

$r_{\min}$. This is highly improbable [8] until the separation of the areas $\mathcal{O}_j$ becomes of order $r_{\max}$, leading to the ergodic time

$$\tau_{\rm erg} = \lambda^{-1} \ln r_{\max}^{-2}. \tag{5.9}$$

The ergodic time varies from $\tau_{\rm erg} \lesssim \lambda^{-1}$ for $r_{\max} \simeq 1$ to $\tau_{\rm erg} = \lambda^{-1} \ln(k_F L/N)$ for $r_{\min} \simeq r_{\max}$. The overlap of the areas $\mathcal{O}_j$ and $\mathcal{O}_{\rm final}$ is the mapping of the transmission band onto the surface of section b. It has an area $p_F L r_{\min}^2 e^{-\lambda t} = O_{\rm tot}(r_{\min}/r_{\max}) e^{-\lambda t}$, leading to Eq. (5.1).

Substituting Eq. (5.8) into Eq. (5.7) we arrive at the number N_{cl} of fully transmitted and reflected channels,

$$N_{cl} = N\theta(\tau_E - \tau_{\rm erg}) \left[1 - e^{(\tau_{\rm erg} - \tau_E)/\tau_{\rm D}}\right], \tag{5.10}$$

$$\tau_E - \tau_{\rm erg} \simeq \lambda^{-1} \ln(N^2/k_F L). \tag{5.11}$$

There are no fully transmitted or reflected channels if $\tau_E < \tau_{\rm erg}$, hence if $N < \sqrt{k_F L}$. Notice that the dependence of τ_E and $\tau_{\rm erg}$ separately on the degree of collimation drops out of the difference $\tau_E - \tau_{\rm erg}$. The number of noiseless channels is therefore insensitive to details of the confining potential. An Ehrenfest time $\propto \ln(N^2/k_F L)$ has appeared before in connection with the Andreev billiard [9], but the role of collimation (and the associated finite ergodic time) was not considered there.

Eqs. (5.5) and (5.8) imply that the majority of noiseless channels group in bands having $N_j \gg 1$, which justifies the semiclassical approximation. The total number of these noiseless bands is of the order of $(N - N_{cl})/\lambda\tau_D$, which is much less than both $N - N_{cl}$ and N_{cl}. Because of this inequality the relatively short trajectories contributing to the noiseless channels are well separated in phase space from other, longer trajectories (cf. Fig. 5.2).

The shot-noise power S is related to the transmission eigenvalues by [10]

$$S = 2e\bar{I} g^{-1} \sum_{k=1}^{N} \mathcal{T}_k(1 - \mathcal{T}_k), \tag{5.12}$$

with $\bar{I}$ the time-averaged current and $g = \sum_k \mathcal{T}_k$ the dimensionless conductance. The N_{cl} fully transmitted or reflected channels have $\mathcal{T}_k = 1$ or 0, hence they do not contribute to the noise. The remaining $N - N_{cl}$ channels contribute at most 1/4 per channel to $Sg/2e\bar{I}$. Using that $g = N/2$ for large N, we arrive at an upper bound for the noise power $S < e\bar{I}(1 - N_{cl}/N)$.

For a more quantitative description of the noise power we need to know the distribution $P(\mathcal{T})$ of the transmission eigenvalues for the $N-N_{cl}$ noisy channels, which can not be described semiclassically. We expect the distribution to have the same bimodal form $P(\mathcal{T}) = \pi^{-1}\mathcal{T}^{-1/2}(1-\mathcal{T})^{-1/2}$ as in the case $N_{cl} = 0$ [6]. This expectation is motivated by the earlier observation that the N_{cl} noiseless channels are well separated in phase space from the $N-N_{cl}$ noisy ones. Using this form of $P(\mathcal{T})$ we find that the contribution to $Sg/2e\bar{I}$ per noisy channel equals $\int_0^1 \mathcal{T}(1-\mathcal{T})P(\mathcal{T})d\mathcal{T} = 1/8$, half the maximum value. The Fano factor $F = S/2e\bar{I}$ is thus estimated as

$$F = \tfrac{1}{4}, \text{ for } N \lesssim \sqrt{k_F L}, \tag{5.13a}$$

$$F = \tfrac{1}{4}(k_F L/N^2)^{N\delta/\pi\hbar\lambda}, \text{ for } N \gtrsim \sqrt{k_F L}. \tag{5.13b}$$

This result should be compared with that of Ref. [2]: $F' = \frac{1}{4}(k_F L)^{-N\delta/\pi\hbar\lambda}$. The ratio $F'/F = \exp[(2N\delta/\pi\hbar\lambda)\ln(N/k_F L)]$ is always close to unity (because $N\delta/\pi\hbar\lambda \simeq N/k_F L \ll 1$). But $F - \frac{1}{4}$ and $F' - \frac{1}{4}$ are entirely different for $N \lesssim \sqrt{k_F L}$, which is the relevant regime in the experiment [5]. There the N dependence of the shot noise was fitted as $F = \frac{1}{4}(1 - t_Q/\tau_D) = \frac{1}{4}(1 - \text{constant} \times N)$, where t_Q is some N-independent time. Eq. (5.13) predicts a more complex N dependence, a plateau followed by a decrease as $\ln F \propto -N\ln(N^2/k_F L)$, which could be observable if the experiment extends over a larger range of N.

We mention two other experimentally observable features of the theory presented here. The reduction of the Fano factor described by Eq. (5.13) is the cumulative effect of many noiseless bands. The appearance of new bands with increasing N introduces a fine structure in $F(N)$, consisting of a series of cusps with a square-root singularity near the cusp. The second feature is the highly nonuniform spatial extension of open channels, evident in Fig. 5.1, which could be observed with the STM technique of Ref. [11]. From a more general perspective the noiseless channels constructed in this chapter show that the random-matrix approach may be used in ballistic systems only for sufficiently small openings: $N \lesssim \sqrt{k_F L}$ is required. For larger N the scattering becomes deterministic, rather than stochastic, and random-matrix theory starts to break down.

Bibliography

[1] C. W. J. Beenakker and H. van Houten, Phys. Rev. B **43**, 12066 (1991).

[2] O. Agam, I. Aleiner, and A. Larkin, Phys. Rev. Lett. **85**, 3153 (2000).

[3] H.-S. Sim, and H. Schomerus, Phys. Rev. Lett. **89**, 066801 (2002); R. G. Nazmitdinov, H.-S. Sim, H. Schomerus, and I. Rotter, Phys. Rev. B **66**, 241302(R) (2002).

[4] G. M. Zaslavsky, Phys. Rep. **80**, 157 (1981).

[5] S. Oberholzer, E. V. Sukhorukov, and C. Schönenberger, Nature **415**, 765 (2002).

[6] R. A. Jalabert, J.-L. Pichard, and C. W. J. Beenakker, Europhys. Lett. **27**, 255 (1994).

[7] The dwell time distribution is defined with a uniform measure in the surface of section of the lead, so that its integral is directly proportional to the number of channels. The mean dwell time $\tau_{\rm D} = \pi\hbar/N\delta$ was calculated by W. Bauer and G. F. Bertsch, Phys. Rev. Lett. **65**, 2213 (1990).

[8] Dwell times shorter than $\tau_{\rm erg}$ are improbable but they may exist for special positions of the two point contacts. The probability that a random position permits a transmitted (or reflected) trajectory of duration $T < \tau_{\rm erg}$ is $\exp[-\lambda(\tau_{\rm erg} - T)]$.

[9] M. G. Vavilov and A. I. Larkin, Phys. Rev. B **67**, 115335 (2003).

[10] M. Büttiker, Phys. Rev. Lett. **65**, 2901 (1990).

[11] M. A. Topinka *et. al.*, Nature **410**, 183 (2001).

Chapter 6

Spectroscopy of a driven solid-state qubit coupled to a structured environment

6.1 Introduction

Currently, we witness an impressive progress in realizing coherent quantum dynamics of macroscopic solid state devices [1–5]. Very recently, experimental results on the quantum dynamics of a superconducting flux qubit coupled to a read-out Superconducting Quantum Interference Device (SQUID) have been reported [6]. The flux qubit consists of a superconducting ring with three Josephson junctions and, in the proper parameter regime, it forms a quantum mechanical macroscopic two-state system (TSS). An external time-dependent driving force controls the state of the TSS. A SQUID couples inductively to the qubit and, together with an external shunt capacitance, it can be modeled as a harmonic oscillator (HO). Due to the coupling of the SQUID to the surrounding environment, the harmonic oscillator is (weakly) damped. The state of the qubit can be inferred from the state of the SQUID. The experiment provides spectroscopic data on the different transition frequencies of the coupled TSS-HO device. Moreover, Rabi oscillations involving different pairs of quantum states of the device have been revealed, including the so-termed red and blue sideband transitions between energy states of the coupled TSS-HO system.

Heading for a comprehensive detailed understanding, a quantitative

modeling which includes the effects of time-dependent driving, decoherence and dissipation is required. In this chapter we give a description which goes beyond the well-known Jaynes-Cummings model [7], by avoiding the strong rotating-wave approximation and by including a microscopic model for the environment. A generic theoretical model for studying the environmental effects on a driven TSS is the driven spin-boson model [8,9]. The environment is characterized by a spectral density $J(\omega)$. The widest used form is that of an Ohmic spectral density, where $J(\omega)$ is proportional to the frequency ω. It mimics the effects of an unstructured Ohmic electromagnetic environment. In the classical limit this leads to white noise and all transitions in the system are damped equally. However, if the environment for the qubit is formed by a quantum measuring device which itself is damped by Ohmic fluctuations, the simple description as an Ohmic environment might become inappropriate. In particular, the SQUID-detector being well described as a HO can equally well be considered as a (broadened) localized mode of the environment influencing the qubit as the central quantum system. In this picture, the plasma resonance at frequency Ω_p of the SQUID gives rise to a non-Ohmic effective spectral density $J_{\rm eff}(\omega)$ for the qubit with a Lorentzian peak at the plasma frequency of the detector [10].

The effects of such a structured spectral density on decoherence have been investigated in several theoretical works in various limits. The role of the external driving being in resonance with the symmetric TSS at zero temperature has been studied in Ref. [11] within a Bloch-Redfield formalism being equivalent to a perturbative approach in $J_{\rm eff}$. Smirnov's analysis [12] is based on the assumption of weak interaction between the TSS and the HO being equivalent to a perturbative approach in $J_{\rm eff}$ as well. Moreover, a rotating-wave approximation is used. The first assumption, however, might become problematic if the driven TSS is in resonance with the HO. The results presented in Refs. [13, 14] reveal in fact, for the undriven case, that a perturbative approach in $J_{\rm eff}$ breaks down for strong qubit-detector coupling, and when the qubit and detector frequencies are comparable. Dephasing times at zero temperature have been determined for the undriven spin-boson model with a structured environment in Ref. [15] within a numerical flow equation method.

As shown in the experiment of Ref. [6], the interplay between the external driving and the dynamics of the coupled TSS-HO system yields to

additional multi-photon transitions, which can be explained only by considering the spectrum of the coupled system. In contrast, if the time-scale of the HO does not play a role, the multi-photon resonances occur in the driven qubit solely, which happens when the driving frequency (or integer multiples of it) matches the characteristic energy scales of the qubit [9]. Such multiphoton resonances can be experimentally detected in an ac-driven flux qubit by measuring the asymptotic occupation probabilities of the qubit, as the dc-field is varied [16]. These qubit resonances, which have also been theoretically investigated within a Bloch equation formalism in Ref. [17], could be explained in terms of intrinsic transitions in a driven spin-boson system with an unstructured environment.

In this chapter, we provide a comprehensive theoretical description of the driven spin-boson system in the presence of a structured environment with one localized mode. Upon making use of the equivalence of this generic model with the model of a driven TSS coupled to an Ohmically damped HO, we first consider the experimentally most interesting case of low temperature and weak damping of the HO while the coupling between the TSS and the HO is kept arbitrary. In this regime, a Floquet-Born-Markov master equation can be established for the driven TSS-HO system. A restriction to the most relevant energy states allows the analytic calculation of the asymptotic TSS time-averaged population P_∞, including the explicit shape of the resonance peaks and dips. We furthermore consider the case of strong damping and/or high temperature which is the complementary parameter regime. An analytic real-time path-integral approach within the non-interacting blip approximation for the driven TSS with the Lorentzian-shaped spectral density allows to analytically determine P_∞ as well. We compare the results obtained from closed analytic expressions with those of numerically exact real-time QUAPI calculations in both parameter regimes and find a very good agreement validating our analytical approaches. Finally, we consider the weakly damped TSS with the localized mode in the limit of large HO frequencies. Then, the localized mode acts as a high-frequency cutoff and the usual Ohmically damped driven TSS is recovered. For this case, we employ an approximation valid for large driving frequencies and obtain a simple expression for the resonance line shapes for multi-photon transitions. Most importantly, we find that the width of the n-photon resonance scales with the n-th ordinary Bessel function.

The chapter is organized as follows: In Sec. 6.2, we present the theo-

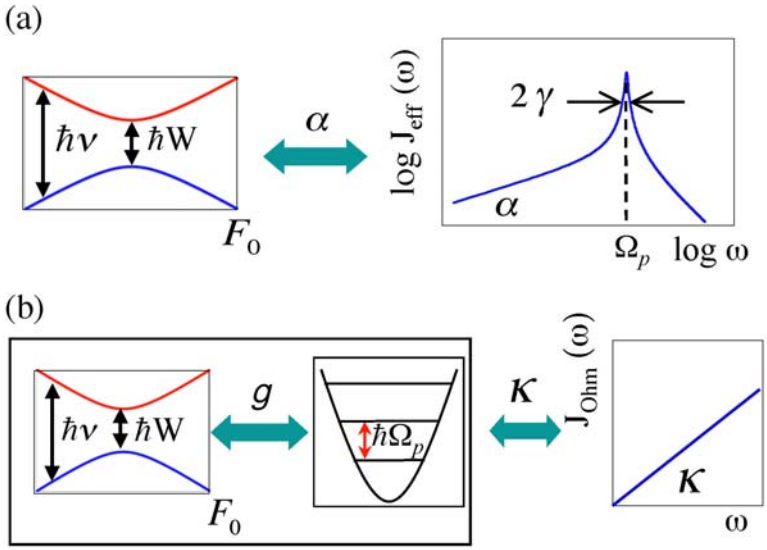

Figure 6.1: Schematic picture of the models we use. In (*a*) the TSS is coupled to an environment which has a peaked spectral density $J_{\rm eff}(\omega)$. In (*b*) the system is shown as a two-level system coupled to a harmonic oscillator which is itself coupled to an Ohmic environment with spectral density $J_{\rm Ohm}(\omega)$.

retical model. Then, we treat the regime of weak damping and low temperatures in Sec. 6.3. The complementary regime of strong damping is investigated in Sec. 6.4. The subsequent Sec. 6.5 contains the limit when the localized mode provides a high-frequency cut-off for the bath, and Sec. 6.6 the discussion of the results and the conclusions. Details of the specific evaluation of rate coefficients are presented in Appendix 6.A. In Appendix 6.B an expansion used in the strong coupling regime is elaborated in detail.

6.2 The driven qubit coupled to a macroscopic detector

The driven TSS is described by the Hamiltonian

$$H_Q(t) = -\frac{\hbar W}{2}\sigma_x - \frac{\hbar F(t)}{2}\sigma_z\,, \tag{6.1}$$

where σ_i are Pauli matrices, $\hbar W$ is the tunnel splitting, and $F(t) = F_0 + s\cos(\Omega t)$ describes the combined effects of a time-dependent driving and the static bias F_0. In the absence of ac-driving ($s = 0$), the level splitting of the isolated TSS is given by

$$\hbar\nu = \hbar\sqrt{F_0^2 + W^2}\,. \tag{6.2}$$

The detector can be associated as part of the TSS environment as a localized mode. This gives the spin-boson Hamiltonian H_{SB} reading [8,9,11–15]

$$H_{SB}(t) \;=\; H_Q(t) + \frac{1}{2}\sigma_z\hbar\sum_k \tilde{\lambda}_k(\tilde{b}_k^\dagger + \tilde{b}_k) + \sum_k \hbar\tilde{\omega}_k\tilde{b}_k^\dagger\tilde{b}_k. \tag{6.3}$$

Here $\tilde{b}_k$ and $\tilde{b}_k^\dagger$ are annihilation and creation operators of the $k-$th bath mode with frequency $\tilde{\omega}_k$. The presence of the detector determines the shape of the spectral density. Following Ref. [10], the dc-SQUID can be modeled as an effective inductance which is shunted with an on-chip capacitance. This gives rise to the effective spectral density

$$J_{\rm eff}(\omega) = \sum_k \tilde{\lambda}_k^2\delta(\omega - \tilde{\omega}_k) = \frac{2\alpha\omega\Omega_p^4}{(\Omega_p^2 - \omega^2)^2 + (2\pi\kappa\omega\Omega_p)^2} \tag{6.4}$$

of the bath having a Lorentzian peak of width $\gamma = 2\pi\kappa\Omega_p$ at the characteristic detector frequency Ω_p. It behaves Ohmically at low frequencies with the dimensionless coupling strength $\alpha = \lim_{\omega\to 0} J_{\rm eff}(\omega)/2\omega$. The qubit dynamics is described by the reduced density operator $\rho(t)$ obtained by tracing out the bath degrees of freedom. The relevant observable which corresponds to the experimentally measured switching probability of the SQUID bias current is the population difference $P(t) := \langle\sigma_z\rangle(t) = {\rm Tr}[\rho(t)\sigma_z]$ between the two localized states of the qubit. We focus on the asymptotic value averaged over one period of the external driving field, i.e., $P_\infty = \lim_{t\to\infty}\langle P(t)\rangle_\Omega$.

In the following, it will become clear that it is convenient to exploit the exact one-to-one mapping [18] of the Hamiltonian (6.3) onto that of a driven TSS coupled to a single harmonic oscillator mode with frequency

Ω_p with interaction strength g. The HO itself interacts with a set of mutually non-interacting harmonic oscillators. The corresponding total Hamiltonian is then

$$H_{QOB}(t) = H_{QO}(t) + H_{OB} \tag{6.5}$$

with

$$\begin{aligned} H_{QO}(t) &= H_Q(t) + \hbar g \sigma_z (B^\dagger + B) + \hbar \Omega_p B^\dagger B\,, \\ H_{OB} &= (B^\dagger + B) \sum_k \hbar \nu_k (b_k^\dagger + b_k) + \sum_k \hbar \omega_k b_k^\dagger b_k + (B^\dagger + B)^2 \sum_k \hbar \frac{\nu_k^2}{\omega_k}\,, \end{aligned} \tag{6.6}$$

where we have omitted the zero-point constant energy terms. Here, B and $B^\dagger$ are the annihilation and creation operators of the localized HO mode, while b_k and $b_k^\dagger$ are the corresponding bath mode operators. The spectral density of the continuous bath modes is now Ohmic with dimensionless damping strength κ, i.e.,

$$J_{\rm Ohm}(\omega) = \sum_k \nu_k^2 \delta(\omega - \omega_k) = \kappa \omega \frac{\omega_D^2}{\omega^2 + \omega_D^2}\,, \tag{6.7}$$

where we have introduced a high-frequency Drude cut-off at frequency ω_D. If ω_D is larger than all other energy scales the particular choice of cut-off does not influence the results at long times. The relation between g and α follows as $g = \Omega_p \sqrt{\alpha/(8\kappa)}$. Fig. 6.1 illustrates a sketch of the two equivalent descriptions of the system. Fig. 6.1a shows the viewpoint where the localized mode is part of the environmental modes, while Fig. 6.1b depicts the perspective of the localized mode being part of the "central" quantum system which itself is coupled to an Ohmic environment. The equivalence of both standpoints has first been pointed out by Garg *et al.* [18] in the context of electron transfer in chemical physics. As shown below, the first way is more convenient for the description in terms of analytic real-time path-integrals (Sec. 6.4), while the second viewpoint is more appropriate for the regime of weak-coupling and for the numerical treatment with QUAPI (see below). Note that the TSS reduced density operator $\rho(t)$ is obtained after tracing out the degrees of freedom of the bath and of the HO. Further progress relies on approximations which depend on the choice of the various parameters.

6.3 Weak coupling: Floquet-Born-Markov master equation

If the coupling between the HO and the bath is weak, i.e., $\kappa \ll 1$, we can choose an approach in terms of a Born-Markov master equation in an extended Floquet description [9, 19, 20]. For a self-contained discussion, we shortly introduce below the required formalism of the Floquet theory. The interested reader can find more details in the review in Ref. [9].

6.3.1 Floquet formalism and Floquet-Born-Markovian master equation

For systems with periodic driving it is convenient to use the Floquet formalism that allows to treat periodic forces of arbitrary strength and frequency [19]. It is based on the fact that the eigenstates of a periodic Hamiltonian $H_{QO}(t) = H_{QO}(t + 2\pi/\Omega)$ are of the form

$$\begin{aligned} |\psi(t)\rangle &= e^{-i\varepsilon_\alpha t/\hbar}|\phi_\alpha(t)\rangle\,, \\ |\phi_\alpha(t)\rangle &= |\phi_\alpha(t + 2\pi/\Omega)\rangle\,, \end{aligned} \tag{6.8}$$

with the Floquet states $|\phi_\alpha(t)\rangle$ being periodic in time (as is the Hamiltonian) and ε_α are called the Floquet or quasi-energies. They can be obtained from the eigenvalue equation

$$\left(H_{QO}(t) - i\hbar\frac{\partial}{\partial t}\right)|\phi_\alpha(t)\rangle = \varepsilon_\alpha|\phi_\alpha(t)\rangle. \tag{6.9}$$

If the quasi-energy ε_α is an eigenvalue with Floquet state $|\phi_\alpha(t)\rangle$, so is $\varepsilon_\alpha + n\hbar\Omega$ with Floquet state $\exp(in\Omega t)|\phi_\alpha(t)\rangle$. Both Floquet states correspond to the same physical state. Because of their periodicity both the Floquet states and the Hamiltonian can be written as a Fourier series, i.e.,

$$\begin{aligned} |\phi_\alpha(t)\rangle &= \sum_n |\phi_\alpha^{(n)}\rangle \exp(in\Omega t)\,, \\ H_{QO}(t) &= \sum_n H_{QO}^{(n)} \exp(in\Omega t). \end{aligned} \tag{6.10}$$

Substituting these Fourier decompositions in the eigenvalue equation (6.9) gives [21]

$$\sum_k (H_{QO}^{(n-k)} + n\hbar\Omega\delta_{kn})\phi_\alpha^{(k)} = \varepsilon_\alpha \phi_\alpha^{(n)} . \tag{6.11}$$

This allows us to define the Floquet Hamiltonian $\mathcal{H}_{QO} \equiv H_{QO}(t) - i\hbar\frac{\partial}{\partial t}$ in matrix form with the matrix elements

$$\langle an|\mathcal{H}_{QO}|bm\rangle = (H_{QO}^{(n-m)})_{ab} + n\hbar\Omega\delta_{ab}\delta_{nm}. \tag{6.12}$$

In the notation $|an\rangle$, a refers to a basis in which to express the Hamiltonian $H_{QO}(t)$, while n refers to the Fourier coefficient. The eigenvectors of $\mathcal{H}_{QO}$ are the coefficients $\phi_\alpha^{(n)}$.

The dynamics of the system coupled to a harmonic bath is described by an equation of motion for the density matrix ρ. Driving effects can be captured in an elegant way by formulating the equation of motion in the basis of Floquet states defined in Eq. (6.8). For weak coupling to the environment, it is sufficient to include dissipative effects to lowest order in κ. Within this approximation, a Floquet-Born-Markov master equation has been established [9, 19, 20]. We average the $2\pi/\Omega$-periodic coefficients of the master equation over one period of the driving, assuming that dissipative effects are relevant only on timescales much larger than $2\pi/\Omega$. This yields equations of motion for the reduced density matrix $\rho_{\alpha\beta}(t) = \langle\phi_\alpha(t)|\rho(t)|\phi_\beta(t)\rangle$ of the form

$$\dot{\rho}_{\alpha\beta}(t) = -\frac{i}{\hbar}(\varepsilon_\alpha - \varepsilon_\beta)\rho_{\alpha\beta}(t) + \sum_{\alpha'\beta'} L_{\alpha\beta,\alpha'\beta'}\rho_{\alpha'\beta'}(t), \tag{6.13}$$

with the dissipative transition rates

$$\begin{aligned} L_{\alpha\beta,\alpha'\beta'} &= \sum_n (N_{\alpha\alpha',n} + N_{\beta\beta',n})X_{\alpha\alpha',n}X_{\beta'\beta,-n} \\ &\quad -\delta_{\beta\beta'}\sum_{\beta'',n} N_{\beta''\alpha',n}X_{\alpha\beta'',-n}X_{\beta''\alpha',n} \\ &\quad -\delta_{\alpha\alpha'}\sum_{\alpha'',n} N_{\alpha''\beta',n}X_{\beta'\alpha'',-n}X_{\alpha''\beta,n}. \end{aligned} \tag{6.14}$$

Here, we have defined

$$\begin{aligned} X_{\alpha\beta,n} &= \sum_k \langle\phi_\alpha^{(k)}|B + B^\dagger|\phi_\beta^{(k+n)}\rangle, \\ N_{\alpha\beta,n} &= N(\varepsilon_{\alpha,\beta,n}) = N(\varepsilon_\alpha - \varepsilon_\beta + n\hbar\Omega), \\ N(\varepsilon) &= \frac{\kappa\varepsilon}{2\hbar}\left(\coth\left(\frac{\varepsilon}{2k_BT}\right) - 1\right). \end{aligned} \tag{6.15}$$

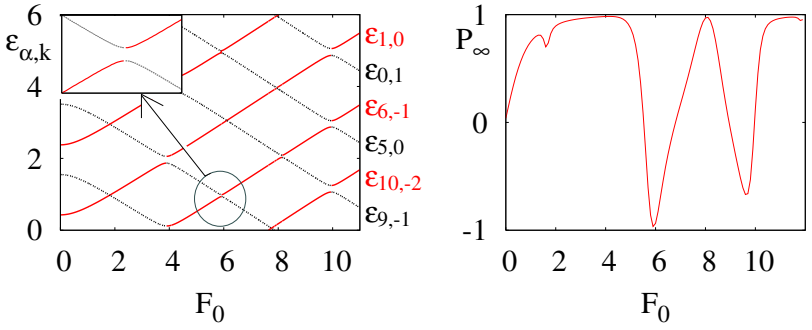

Figure 6.2: Left: Quasi-energy spectrum $\varepsilon_{\alpha,k}$ of the driven TSS+HO system as a function of the dc-bias F_0 (in units of W). The quasi-energies are defined up to an integer multiple of $\hbar\Omega$, i.e., $\varepsilon_{\alpha,k} = \varepsilon_\alpha + k\hbar\Omega$. Inset: Zoom of an anti-crossing. Right: P_∞ exhibits resonance dips corresponding to quasi-energy level anti-crossings. Parameters are $\Omega = 10W, s = 4W, g = 0.4W, \Omega_p = 4W, \kappa = 0.014$ and $k_B T = 0.1\hbar W$.

We have neglected the weak quasi-energy shifts, which are of first order in the coupling to the environment. In the sequel, we will see from a comparison with exact numerical results that this approximation is well justified. In order to be able to solve Eq. (6.13), it is necessary to determine the Floquet quasi-energies ε_α and Floquet states $|\phi_\alpha^{(n)}\rangle$. How they can be determined perturbatively, is shown in the following subsection.

6.3.2 Van Vleck perturbation theory

First, we have to specify the basis for the Floquet Hamiltonian according to Eq. (6.12). For the TSS+HO Hamiltonian H_{QO}, we use the basis $|an\rangle$ defined via the single particle product state $|a\rangle = |g/e\, m\rangle$ with $|g/e\rangle$ being the ground/excited state of the qubit, $|m\rangle$ the HO eigenstate, and n the corresponding Fourier index. In detail, this implies that we can divide the Hamiltonian into a diagonal part

$$\begin{aligned} (\mathcal{H}_{QO})_{gmn,gmn} &= \hbar[-\nu/2 + m\Omega_p + n\Omega]\,, \\ (\mathcal{H}_{QO})_{emn,emn} &= \hbar[\nu/2 + m\Omega_p + n\Omega]\,, \end{aligned} \tag{6.16}$$

and an off-diagonal part

$$(\mathcal{H}_{QO})_{an,bk} = V_{an,bk}\,, \quad \text{for } a \neq b, n \neq k\,, \tag{6.17}$$

which has non-zero elements. They read

$$\begin{aligned}
V_{g(e)ln,g(e)mn} &= +(-)\frac{(\sqrt{m+1}\delta_{l,m+1}+\sqrt{l+1}\delta_{l+1,m})\hbar g F_0}{\nu}\,,\\
V_{g(e)ln,e(g)mn} &= -\frac{(\sqrt{m+1}\delta_{l,m+1}+\sqrt{l+1}\delta_{l+1,m})\hbar g W}{\nu}\,,\\
V_{g(e)mn,g(e)mk} &= -(+)\frac{(\delta_{k,n+1}+\delta_{k+1,n})\hbar s F_0}{4\nu}\,,\\
V_{g(e)mn,e(g)mk} &= \frac{(\delta_{k,n+1}+\delta_{k+1,n})\hbar s W}{4\nu}\,.
\end{aligned} \tag{6.18}$$

In the remainder of this section we will assume that the elements of V are small compared to the diagonal elements of $\mathcal{H}_{QO}$, which is justified if the coupling g between TSS and HO and the driving amplitude s are small compared to the other energy scales, i.e., $s, g \ll \Omega, \nu, \Omega_p$. This is the case in realistic experimental devices [6, 13]. The Fourier index n ranges from $-\infty$ to ∞ and m from 0 to ∞. The eigenvalues of the Floquet Hamiltonian following from Eqs. (6.17) and (6.18) have to be calculated numerically for a particular cut-off n_{max} and m_{max}. In Fig. 6.2, the numerically obtained quasi-energy spectrum is shown as a function of the static bias F_0 for the case $m_{\max} = 4$ and $|n_{\max}| = 8$. We find that for some values of the bias F_0 avoided crossings of the quasi-energy levels occur when two diagonal elements of $\mathcal{H}_{QO}$ have approximately the same values, i.e., when the condition

$$E_{an,bm} := (\mathcal{H}_{QO})_{an,an} - (\mathcal{H}_{QO})_{bm,bm} = 0 + \mathcal{O}(V^2) \tag{6.19}$$

is fulfilled. It follows from Eq. (6.17) that this happens when at least one of the two conditions

$$\begin{aligned}
\nu &= n\Omega \pm m\Omega_p + \mathcal{O}(V^2)\,,\\
n\Omega &= m\Omega_p + \mathcal{O}(V^2)\,,
\end{aligned} \tag{6.20}$$

is fulfilled. At these avoided crossings the Floquet spectrum has quasi-degeneracies and as a consequence there are transitions between the different Floquet states. As it turns out below, this results in resonant peaks/dips in the stationary averaged population difference P_∞, cf. Fig. 6.2.

Since we are interested in describing the resonance line shape for P_∞, we have to determine the quasi-energies and Floquet states around a resonance, i.e., around an avoided crossing. For this, we use an approach which

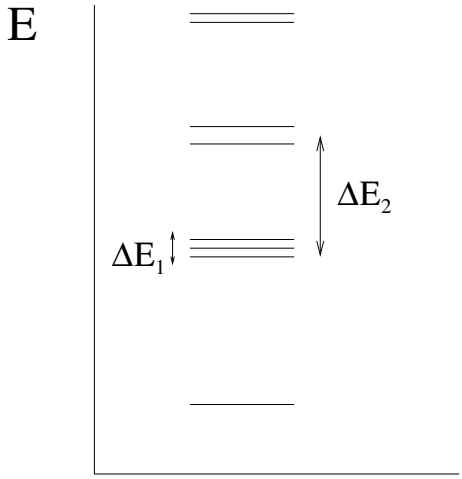

Figure 6.3: Typical energy spectrum suited for the Van Vleck perturbation theory: Different groups of (nearly) degenerate levels of eigenenergies are well separated in energy (i.e., $\Delta E_1 \ll \Delta E_2$).

is perturbative in V. The unperturbed Hamiltonian is diagonal and, close to an avoided crossing, (nearly) degenerate. An appropriate perturbative method is the Van Vleck perturbation theory [7,22] suitable for Hamiltonians for which the unperturbed spectrum has groups of (nearly) degenerate eigenvalues, well separated in energy space. An example of such a spectrum is shown in Fig. 6.3. This method defines a unitary transformation which transforms the Hamiltonian into an effective block-diagonal one. The effective Hamiltonian then has the same eigenvalues as the original Hamiltonian, with the quasi-degenerate eigenvalues in one common block.

The effective Hamiltonian can be written as

$$\mathcal{H}_{\text{eff}} = e^{iS}\mathcal{H}_{QQ}e^{-iS}. \tag{6.21}$$

In Ref. [7] it is shown how to obtain S systematically for every order in the perturbation. The small parameter is $V/\Delta E_2$ (see Fig. 6.3). Eigenvalues within one block can be arbitrarily close. This means that we can also use the expansion at resonance. We derive the expressions up to the second order in the perturbation. Two different cases are relevant: For the case

when $(\mathcal{H}_{QO})_{an,an}$ and $(\mathcal{H}_{QO})_{bm,bm}$ are not nearly degenerate we find

$$\begin{aligned} iS^{(1)}_{an,bm} &= \frac{V_{an,bm}}{E_{an,bm}}, \\ iS^{(2)}_{an,bm} &= \sum_{c,k} \frac{V_{an,ck}V_{ck,bm}}{2E_{bm,an}} \left(\frac{1}{E_{ck,an}} + \frac{1}{E_{ck,bm}} \right), \end{aligned} \tag{6.22}$$

where the superscript indicates the order of perturbation theory. For the second case when $(\mathcal{H}_{QO})_{an,an}$ and $(\mathcal{H}_{QO})_{bm,bm}$ are nearly degenerate, we find $iS^{(1)}_{an,bm} = iS^{(2)}_{an,bm} = 0$.

Inserting the expressions for $S_{an,bm}$ into Eq. (6.21), the matrix elements of the n-th order term $\mathcal{H}^{(n)}_{\text{eff}}$ of the effective Hamiltonian can be calculated, again for both cases. When $(\mathcal{H}_{QO})_{an,an}$ and $(\mathcal{H}_{QO})_{bm,bm}$ are not nearly degenerate, we find $(\mathcal{H}_{\text{eff}})^{(1)}_{an,bm} = (\mathcal{H}_{\text{eff}})^{(2)}_{an,bm} = 0$. For the second case, when $(\mathcal{H}_{QO})_{an,an}$ and $(\mathcal{H}_{QO})_{bm,bm}$ are nearly degenerate, one finds

$$\begin{aligned} (\mathcal{H}_{\text{eff}})^{(1)}_{an,bm} &= V_{an,bm}, \\ (\mathcal{H}_{\text{eff}})^{(2)}_{an,bm} &= \frac{1}{2} \sum_{c,k} V_{an,ck}V_{ck,bm} \left(\frac{1}{E_{an,ck}} + \frac{1}{E_{bm,ck}} \right). \end{aligned} \tag{6.23}$$

Since the effective block-diagonal Hamiltonian consequently only has 2×2 blocks (we assume that resonances do not overlap), it is easy to diagonalize it. To obtain the eigenvectors of the original Floquet Hamiltonian (see Eqs. (6.16), (6.17) and (6.18)), the inverse of the transformation defined in Eq. (6.21) has to be performed on the eigenvectors. There is an infinite number of quasi-energy levels and Floquet states. However, because the eigenvalues ε_α and $\varepsilon_\alpha + n\hbar\Omega$ represent the same physical state, only one of them has to be considered. Still there is an infinite number of levels because the Hilbert space of the HO Hamiltonian is infinite dimensional. Nevertheless, for practical calculations, only the relevant HO levels have to be taken into account. When there is a resonance between the states $|e/g, 0, n\rangle$ and $|e/g, l, n+k\rangle$, then at least the first l levels of the HO play a role. Higher levels can be omitted if one is interested in low temperatures (which is commonly the case), since for low temperatures their occupation number will be very small.

6.3.3 Line shape of the resonant peak/dip

To obtain the line shape of the resonant peak/dip in P_∞, we have to determine the stationary solution of Eq. (6.13). Depending on the number n_{max} of Floquet states taken into consideration, this might be considerably difficult. One facilitation might arise due to symmetries, i.e., elements of $L_{\alpha\beta,\alpha'\beta'}$ being of the same size. Another possibility appropriate at low temperatures might be to neglect some of the dissipative transition rates. Moreover, a further possible approximation can be applied for $\rho_{\alpha\beta}(\infty)$, if ε_α and ε_β are not nearly-degenerate eigenvalues. In that case $\varepsilon_\alpha - \varepsilon_\beta$ in Eq. (6.13) is much larger than the coefficients $L_{\alpha\beta\alpha'\beta'}$, since the coupling to the Ohmic environment is assumed to be weak. This, in turn, allows to make the partial secular approximation by setting $\rho_{\alpha\beta}(\infty) = 0$. After the reduced density matrix in the Floquet basis is known, it is straightforward to calculate P_∞.

6.3.4 Example: The first blue sideband

As an example we will derive an analytical expression for the resonant dip at $\nu \approx \Omega - \Omega_p$ which is called the first blue sideband. For this case, the matrix elements $(\mathcal{H}_{QO})_{g0\,n+1,g0\,n+1}$ and $(\mathcal{H}_{QO})_{e1n,e1n}$ are nearly degenerate, i.e.,

$$-\nu/2 + (n+1)\Omega \approx \nu/2 + \Omega_p + n\Omega\,. \tag{6.24}$$

As the resonance occurs between two states which differ only by one oscillator quantum, we only take into account one excited level of the oscillator. We expect that this is a reasonable approximation for not too strong driving and low temperatures. The validity of this approximation will be checked against numerically exact results in the end. The elements of the transformation matrix S follow as $S_{g0\,n+1,e1n} = S_{e1n,g0\,n+1} = 0$, while the remaining elements can be calculated straightforwardly using Eq. (6.22) and they will not be given here explicitly.

Since we include one HO excited energy level, we have four physically different eigenstates. Hence, we can express $\mathcal{H}_{QO}$ in the basis $\{|e,1,-1\rangle$, $|g,0,0\rangle, |g,1,0\rangle, |e,0,0\rangle\}$. Performing the transformation defined in Eq. (6.21), we obtain the effective Hamiltonian in this basis as

$$\mathcal{H}_{\rm eff} = \hbar \begin{pmatrix} \frac{\nu}{2} + \Omega_p - \Omega + \Delta_1 & -\tilde{W} & 0 & 0 \\ -\tilde{W} & -\frac{\nu}{2} + \Delta_2 & 0 & 0 \\ 0 & 0 & -\frac{\nu}{2} + \Omega_p + \Delta_3 & 0 \\ 0 & 0 & 0 & \frac{\nu}{2} + \Delta_4 \end{pmatrix}. \tag{6.25}$$

The matrix elements are calculated using Eq. (6.23). They read

$$\begin{aligned} \tilde{W} &= \frac{W F_0 g s \left[\Omega^2 + \Omega_p^2 + \nu(-\Omega + \Omega_p)\right]}{4\nu(\Omega - \nu)\Omega\,\Omega_p(\nu + \Omega_p)}, \\ \Delta_1 &= -\Delta_2 = \frac{F_0^2 g^2}{\nu^2 \Omega_p} + \frac{W^2 g^2}{\nu^2(\nu + \Omega_p)} + \frac{W^2 s^2}{8\nu(\nu^2 - \Omega^2)}, \\ \Delta_3 &= -\Delta_4 = \frac{F_0^2 g^2}{\nu^2 \Omega_p} - \frac{W^2 g^2}{\nu^2(\nu - \Omega_p)} - \frac{W^2 s^2}{8\nu(\nu^2 - \Omega^2)}. \end{aligned} \tag{6.26}$$

The eigenvalues of the Hamiltonian (6.25) are the relevant quasi-energies, and they are readily obtained by diagonalization as

$$\begin{aligned} \frac{\varepsilon_{1/2}}{\hbar} &= -\frac{\nu}{2} + \frac{\delta F}{2}\left(1 \mp \sqrt{1 + \frac{\tilde{W}^2}{\delta F^2}}\right) - \Delta_1, \\ \frac{\varepsilon_3}{\hbar} &= -\frac{\nu}{2} + \Omega_p + \Delta_3, \\ \frac{\varepsilon_4}{\hbar} &= \frac{\nu}{2} + \Delta_4. \end{aligned} \tag{6.27}$$

From these formulas it follows that $\delta F = \nu - \Omega + \Omega_p + 2\Delta_1$ is a measure of how far the system is off resonance. For $\delta F = 0$, the quasi-energies ε_1 and ε_2 show an avoided crossing of size $\hbar\tilde{W}$. Note that Eq. (6.13) implies that $\tilde{W}$ is the Rabi frequency at the blue sideband.

The eigenvectors, which are the Floquet states, of the 4×4 effective block-diagonal matrix in Eq. (6.25) are easily obtained by performing the corresponding inverse transformation. We find, with $\tan\theta = 2|\tilde{W}|/\delta F$, the eigenstates

$$\begin{aligned} |\phi_1\rangle &= e^{-iS}[\sin(\theta/2)e^{-i\Omega t}|e,1\rangle + \cos(\theta/2)|g,0\rangle], \\ |\phi_2\rangle &= e^{-iS}[\cos(\theta/2)e^{-i\Omega t}|e,1\rangle - \sin(\theta/2)|g,0\rangle], \\ |\phi_{3/4}\rangle &= e^{-iS}|g/e,1/0\rangle. \end{aligned} \tag{6.28}$$

We have used the inverse transformation of Eq. (6.10) to illustrate the time dependence explicitly. Next, we calculate the rates given in Eq. (6.14) up to second order in V.

Only the quasi-energies ε_1 and ε_2 are quasi-degenerate. Therefore, we assume a *partial secular approximation*: We set almost all off-diagonal elements of ρ to zero but keep $\rho_{12}(\infty)$ and $\rho_{21}(\infty) = \rho_{12}^*(\infty)$ different from zero. This allows to simplify the master equation (6.13). The stationary solutions are determined by the conditions

$$\begin{aligned} 0 &= \sum_\beta L_{\alpha\alpha,\beta\beta}\rho_{\beta\beta}(\infty) + (L_{\alpha\alpha,12} + L_{\alpha\alpha,21})\mathrm{Re}[\rho_{12}(\infty)], \\ 0 &= -\frac{i}{\hbar}(\varepsilon_1 - \varepsilon_2)\rho_{12}(\infty) + \sum_\alpha L_{12,\alpha\alpha}\rho_{\alpha\alpha}(\infty) \\ &\quad + L_{12,12}\rho_{12}(\infty) + L_{12,21}\rho_{12}^*(\infty). \end{aligned} \tag{6.29}$$

It is most convenient to use the symmetry properties of the corresponding rates which are specified for this particular example in Eq. (6.58) in Appendix 6.A. In turn, there are eight independent rates associated to all possible transitions. They are explicitly given in Eq. (6.59).

First we consider the rates exactly at resonance $\delta F = 0$. Since then $\sin^2(\theta/2) = \cos^2(\theta/2) = 1/2$, all rates contain a term which is of zeroth order in V. If we neglect the small second order terms, we find

$$\begin{aligned} L_{22,44} &= L_{11,44} = L_{33,22} = L_{33,11} = -L_{33,21} = L_{21,44} = N(\hbar\Omega_p)\,, \\ L_{22,33} &= L_{11,33} = L_{44,22} = L_{44,11} = L_{44,21} = -L_{21,33} = N(-\hbar\Omega_p)\,, \\ L_{11,21} &= L_{22,21} = L_{21,22} = L_{21,11} = \frac{1}{2}[N(\hbar\Omega_p) - N(-\hbar\Omega_p)]\,, \\ L_{12,12} &= -N(-\hbar\Omega_p) - N(\hbar\Omega_p)\,. \end{aligned} \tag{6.30}$$

Solving Eq. (6.29) together with (6.30) finally yields

$$\begin{aligned} \rho_{11}(\infty) &= \rho_{22}(\infty) = \frac{N(-\hbar\Omega_p)N(\hbar\Omega_p)}{[N(-\hbar\Omega_p) + N(\hbar\Omega_p)]^2}\,, \\ \rho_{33}(\infty) &= \frac{N(\hbar\Omega_p)^2}{[N(-\hbar\Omega_p) + N(\hbar\Omega_p)]^2}\,, \\ \rho_{44}(\infty) &= \frac{N(-\hbar\Omega_p)^2}{[N(-\hbar\Omega_p) + N(\hbar\Omega_p)]^2}\,, \\ \rho_{12}(\infty) &= 0\,. \end{aligned} \tag{6.31}$$

Eventually, this gives the simple result at resonance, $\delta F = 0$,

$$P_\infty = -\frac{F_0}{\nu}\tanh\left(\frac{\hbar\Omega_p}{2k_BT}\right) + \mathcal{O}\left(V^2\right) , \tag{6.32}$$

which implies a complete inversion of population at low temperatures! We will discuss the physics behind it in section 6.3.5. Note that no further assumption on the temperature was made while deriving this formula.

Next we will derive an expression for the peak shape around the resonance. For this, we assume low temperatures, i.e., $k_BT/\hbar \ll \Omega_p, \Omega, \nu$. This allows us to set $N(\hbar\Omega_p) = N(\hbar\Omega) = N(\hbar\nu) = 0$. Far enough away from resonance, it is appropriate to assume that $\rho_{12}(\infty) \approx \rho_{21}(\infty) \approx 0$, and $\sin(\theta/2) \approx \theta/2$. Thus, it follows from Eq. (6.58) that there are only four independent rates in this case, namely $L_{44,22}, L_{22,44}, L_{44,11}$ and $L_{11,44}$. Within our approximations, we find that $L_{22,44} = \mathcal{O}(V^3)$. So only three rates are relevant which read

$$\begin{aligned} L_{44,22} &= 2\cos^2(\theta/2) \approx 2\,, \\ L_{11,44} &= 2L_{\mathrm{q}}(\varepsilon_{1,4,0})\cos^2(\theta/2) \approx \frac{8W^2g^2\Omega_p^2}{(\nu^3-\nu\Omega_p^2)^2}\,, \\ L_{44,11} &= 2\sin^2(\theta/2) \approx \theta^2/2 \approx 2\tilde{W}^2/\delta F^2\,, \end{aligned} \tag{6.33}$$

where the quantity L_{q} is given in Appendix 6.A. Note that $L_{44,22} \gg L_{44,11}$, $L_{11,44}$. In this limit we find for the asymptotic density matrix elements

$$\begin{aligned} \rho_{11}(\infty) &= \frac{L_{11,44}}{L_{11,44}+L_{44,11}}\,, \\ \rho_{22}(\infty) &= \rho_{33}(\infty) = 0\,, \\ \rho_{44}(\infty) &= 1-\rho_{11}(\infty)\,, \end{aligned} \tag{6.34}$$

which gives the central result

$$\begin{aligned} P_\infty &= \frac{F_0}{\nu}\frac{L_{11,44}-L_{44,11}}{L_{11,44}+L_{44,11}} + \mathcal{O}\left(V^2\right) \\ &\simeq \frac{F_0}{\nu}\left(1-\frac{2\tilde{W}^2\nu^2(\nu^2-\Omega_p^2)^2}{\tilde{W}^2\nu^2(\nu^2-\Omega_p^2)^2+4W^2g^2\Omega_p^2\delta F^2}\right). \end{aligned} \tag{6.35}$$

A comparison between the result of this formula and different numerical results, including those of an exact numerical ab-initio real-time QUAPI calculation [23–25], is shown in Fig. 6.4. For the QUAPI-simulations, we

have used the optimized parameters [25] $\Delta t = 0.23/W, M = 12$ and $K = 1$. Moreover, we have applied an exponential cut-off for the Ohmic bath with a cut-off frequency $\omega_c = 10W$ (since we are considering long-time stationary results, the explicit shape of the cut-off is irrelevant). Note that the picture of the TSS+HO being the central quantum system which is coupled to an Ohmic environment is particularly suited for QUAPI since the coherent dynamics of the central quantum system is treated exactly. A very good agreement, even near resonance, is found among all the used numerical schemes.

6.3.5 Results and discussion

We will now try to give a more physical insight into the nature of the first blue sideband. First consider the case when $T = 0$ and we are exactly at resonance. The driving induces transitions from $|g,0\rangle$ to $|e,1\rangle$ while the direct coupling of the HO to the environment will cause a fast decay of the population from $|e,1\rangle$ to $|e,0\rangle$. This transition from $|g,0\rangle$ to $|e,0\rangle$ via driving and decay has to compete with the decay from $|e,0\rangle$ to $|g,0\rangle$, but the last process is much slower because the TSS is not directly coupled to the environment. So all the population is in $|e,0\rangle$ and there is a complete inversion of population (cf. Eq. (6.32)). For $T \neq 0$ there will be a thermal equilibrium between ground and excited state of the oscillator.

When the system is not exactly at resonance the driving induced transitions are much slower $\propto g^2$ and the decay of the oscillator is still fast. This means that the transition from $|g,0\rangle$ to $|e,0\rangle$ is slower than at resonance. The time associated with the decay from $|e,0\rangle$ to $|g,0\rangle$ is also $\propto g^2$ and the ratio of the time scales of the two processes gives the ratio of the populations of $|e,0\rangle$ and $|g,0\rangle$ (at $T = 0$, for higher T the states $|g/e,1\rangle$ are also populated). This ratio is independent of g and so is P_∞ (given in Eq. (6.35)).

A similar analysis can be performed for the first red sideband at $\nu = \Omega + \Omega_p$. At resonance it yields $P_\infty = \frac{F_0}{\nu} \tanh(\frac{\hbar\Omega_p}{2k_BT}) + \mathcal{O}(V^2)$, which is very close to thermal equilibrium for low T.

For the resonance at $\nu = \Omega_p$, only the oscillator is excited. After having traced it out, we expect just thermal equilibrium given by $P_\infty = \frac{F_0}{\nu} \tanh(\frac{\hbar\nu}{2k_BT})$.

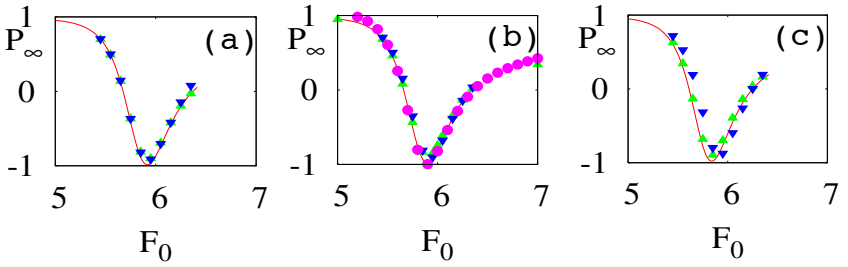

Figure 6.4: P_∞ as a function of the dc-bias F_0 (in units of W) around the peak at $\nu = \Omega - \Omega_p$. The solid lines are the analytical prediction (6.35) for (a) $g = 0.05W$, (b) $g = 0.2W$, (c) $g = 0.4W$. The triangles are the results of a Floquet-Bloch-Redfield simulation, cf. Eq. (6.13), with one (upward triangles) and two (downward triangles) HO levels taken into account. The circles in (b) are the results from a QUAPI simulation with six HO levels (see text). We choose $s = 2W$, $\Omega = 10W$, $\kappa = 0.014$, $k_BT = 0.1\hbar W$.

6.4 Strong coupling: NIBA

In the complementary regime of large environmental coupling and/or high temperature it is convenient to employ model (a), and it is appropriate to treat the system's dynamics within the noninteracting-blip approximation (NIBA) [8]. The NIBA is non-perturbative in the coupling α but perturbative in the tunneling splitting W. It is a good approximation for sufficiently high temperatures and/or dissipative strength, or for symmetric systems. Within the NIBA and in the limit of large driving frequencies $\Omega \gg W$, one finds [9]

$$P_\infty = \frac{k_0^-(0)}{k_0^+(0)}\,. \tag{6.36}$$

Here,

$$\begin{aligned} k_0^-(0) &= W^2 \int_0^\infty dt h^-(t) \sin(F_0 t) J_0\left(\frac{2s}{\Omega}\sin\frac{\Omega t}{2}\right), \\ k_0^+(0) &= W^2 \int_0^\infty dt h^+(t) \cos(F_0 t) J_0\left(\frac{2s}{\Omega}\sin\frac{\Omega t}{2}\right), \end{aligned} \tag{6.37}$$

with J_0 being the zeroth order Bessel function. Dissipative effects of the environment are captured by the terms

$$\begin{aligned} h^+(t) &= e^{-Q'(t)}\cos[Q''(t)]\,, \\ h^-(t) &= e^{-Q'(t)}\sin[Q''(t)]\,. \end{aligned} \tag{6.38}$$

Here, $Q'(t)$ and $Q''(t)$ are the real and imaginary parts of the bath correlation function

$$Q(t) = \int_0^\infty d\omega \frac{J(\omega)}{\omega^2}\,\frac{\cosh(\omega\beta/2) - \cosh[\omega(\beta/2 - it)]}{\sinh(\omega\beta/2)}\,.$$

For the peaked spectral density given in Eq. (6.4) one finds

$$\begin{aligned} Q'(t) &= Q_1'(t) - e^{-\Gamma t}[Y_1\cos(\bar{\Omega}_p t) + Y_2\sin(\bar{\Omega}_p t)]\,, \\ Q''(t) &= A_1 - e^{-\Gamma t}[A_1\cos(\bar{\Omega}_p t) + A_2\sin(\bar{\Omega}_p t)]\,. \end{aligned} \tag{6.39}$$

Here, $\beta = \hbar/k_B T, \Gamma = \pi\kappa\Omega_p$, $\bar{\Omega}_p^2 = \Omega_p^2 - \Gamma^2$ and

$$\begin{aligned} Q_1'(t) &= Y_1 + \pi\alpha\Omega_p^2\left[\frac{\sinh(\beta\bar{\Omega}_p)t}{2C\bar{\Omega}_p} + \frac{\sin(\beta\Gamma)t}{2C\Gamma}\right. \\ &\quad \left. -\frac{4\Omega_p^2}{\beta}\sum_{n=1}^{\infty}\frac{\frac{1}{\nu_n}[e^{-\nu_n t}-1]+t}{(\Omega_p^2+\nu_n^2)^2 - 4\Gamma^2\nu_n^2}\right], \end{aligned} \tag{6.40}$$

where $\nu_n = 2\pi n/\beta$. Moreover, $C = \cosh(\beta\bar{\Omega}_p) - \cos(\beta\Gamma)$, $A_2 = \alpha\pi(\Gamma^2 - \bar{\Omega}_p^2)/(2\Gamma\bar{\Omega}_p)$, $A_1 = \pi\alpha$, $CY_{1/2} = \mp A_{2/1}\sinh(\beta\bar{\Omega}_p) - A_{1/2}\sin(\beta\Gamma)$. As follows from Eq. (6.39), Q' and Q'' display damped oscillations with frequency $\bar{\Omega}_p$ (cf. Fig. 6.5b) which are not present for a pure Ohmic spectrum. It is the interplay between these oscillations and the driving field which induces the extra resonances in P_∞.

To proceed, we rewrite the kernels $k_0^{\pm}(0)$ in a more convenient form. In the integrand of Eq. (6.37) the functions $\cos[Q''(t)]$, $\sin[Q''(t)]$ and $e^{-Q'(t)+Q_1'(t)}$ oscillate with frequency $\bar{\Omega}_p$ and we can expand them as

$$\begin{aligned} \cos[Q''(t)] &= \sum_{m=-\infty}^{\infty}\left[D_m\cos(m\bar{\Omega}_p t) + E_m\sin(m\bar{\Omega}_p t)\right], \\ \sin[Q''(t)] &= \sum_{m=-\infty}^{\infty}\left[F_m\cos(m\bar{\Omega}_p t) + G_m\sin(m\bar{\Omega}_p t)\right], \\ e^{-Q'(t)+Q_1'(t)} &= \sum_{m=-\infty}^{\infty}\left[H_m\cos(m\bar{\Omega}_p t) + K_m\sin(m\bar{\Omega}_p t)\right]. \end{aligned} \tag{6.41}$$

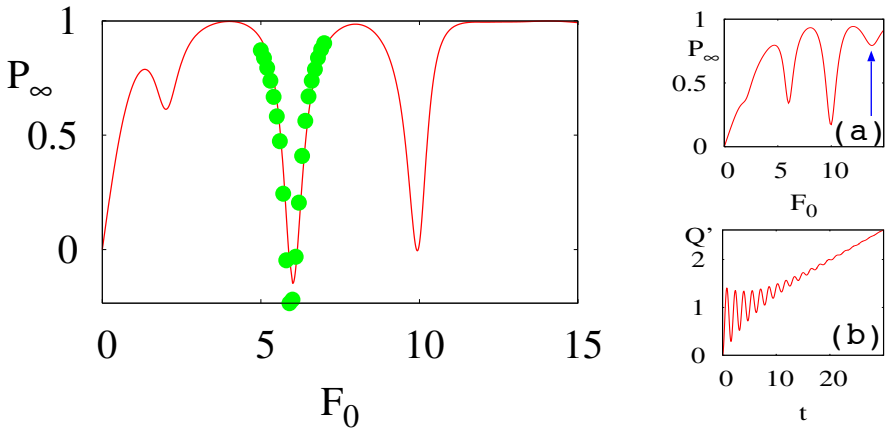

Figure 6.5: P_∞ as a function of the dc-bias F_0 (in units of W). The solid line is the NIBA prediction, while the circles are from a QUAPI simulation with 6 HO levels ($g = 3W$, $s = 4W$, $\Omega = 10W$, $\kappa = 0.014$, $k_BT = 0.5\hbar W$, $\Omega_p = 4W$). Inset (a): NIBA result for $k_BT = 2\hbar W$. The arrow indicates the first red sideband at $\nu = \Omega + \Omega_p$. Inset (b): $Q'(t)$ shows damped oscillations.

The coefficients D_m, E_m, F_m, G_m, H_m and K_m are time-dependent and they are given in Appendix 6.B. Inserting these expansions into Eq. (6.37), and also using the Fourier representation of $J_0\left(\frac{2s}{\Omega}\sin\frac{\Omega t}{2}\right)$, we find

$$k_0^{\pm}(0) = \sum_{m=-\infty}^{\infty}\sum_{n=-\infty}^{\infty} W^2 \int_0^{\infty} dt e^{-Q_1'(t)} f_{mn}^{\pm}(t)\,. \tag{6.42}$$

Here, $F_{mn} = F_0 - m\bar{\Omega}_p - n\Omega$, and

$$\begin{aligned} f_{mn}^{\pm}(t) &= \begin{matrix}\mathrm{Re}\\ \mathrm{Im}\end{matrix}\left[c_{mn}^{\pm}(t)\cos(F_{mn}t) \pm c_{mn}^{\mp}(t)\sin(F_{mn}t)\right], \\ c_{mn}^{+} &= J_n^2\left(\frac{s}{\Omega}\right) J_m(e^{-\Gamma t}\omega_1)\cos(m\phi)(-i)^m e^{-iA_1}, \\ c_{mn}^{-} &= J_n^2\left(\frac{s}{\Omega}\right) J_m(e^{-\Gamma t}\omega_1)\sin(m\phi)(-i)^m e^{-iA_1}, \end{aligned} \tag{6.43}$$

with J_n being a Bessel function of order n, and

$$\begin{aligned} \omega_1 &= \sqrt{(A_1 - iY_1)^2 + (A_2 - iY_2)^2}\,, \\ \tan\phi &= -\frac{A_2 - iY_2}{A_1 - iY_1}\,. \end{aligned} \tag{6.44}$$

Thus, from Eq. (6.43), we expect resonances when $F_{nm} = 0$.

In the limit $\Gamma/\Omega_p \ll 1$ and for not too large T (i.e., $\cos(\beta\Gamma) \ll \cosh(\beta\Omega_p)$), we find that

$$\tan(m\phi) \approx i \tanh\left(\frac{m\beta\Omega_p}{2}\right). \tag{6.45}$$

Inserting this into Eq. (6.43), we obtain

$$i \tanh\left(\frac{m\beta\Omega_p}{2}\right) c^+_{mn} = c^-_{mn}. \tag{6.46}$$

If the environmental mode is enough localized (i.e., the integrand of Eq. (6.37) is only damped after several oscillations), we expect that the sum in Eq. (6.42) is dominated by the coefficient of $\cos(F_{nm}t)$ if $F_{mn} = 0$. This means that

$$\begin{aligned} f^+_{mn}(t) &\approx \mathrm{Re}[c^+_{mn}(t)] \\ f^-_{mn}(t) &\approx \tanh\left(\frac{m\beta\Omega_p}{2}\right) \mathrm{Re}[c^+_{mn}(t)], \end{aligned} \tag{6.47}$$

which leads to

$$P_\infty = \tanh\left(\frac{m\beta\Omega_p}{2}\right). \tag{6.48}$$

Without driving we only have terms with $n = 0$, and $F_{m0} = 0$ implies that $F_0 = m\Omega_p$. In that case Eq. (6.48) gives the NIBA thermal equilibrium value. Hence, in order to find resonances we need to apply driving. For "conventional" resonances at $F_0 = n\Omega$, we put m to zero and we find $P_\infty \approx 0$, as predicted for unstructured environments [17, 26]. Finally, for $F_0 = n\Omega \pm m\Omega_p$, we recover $P_\infty \approx \pm\tanh(m\beta\Omega_p/2)$, as was also found within the Floquet-Born-Markov approach, cf. Eq. (6.32). Results of a numerical evaluation of P_∞ are shown in Fig. 6.5, using the NIBA result (6.43), as well as the exact ab-initio real-time QUAPI method [23–25]. Resonance dips are observed at $F_0 = \Omega$, $F_0 = \Omega - \Omega_p$ and $F_0 = \Omega - 2\Omega_p$. For $k_BT \sim \hbar\Omega_p$, we also find the first red sideband at $F_0 = \Omega + \Omega_p$, see inset (a).

6.5 Limit $\Omega_p \gg \nu$

In the limit when the frequency Ω_p of the HO is much larger than the effective TSS level splitting ν, the peak in the spectral density at Ω_p acts as

a high-frequency cut-off for an effective Ohmic bath, see Eq. (6.4). In other words, the oscillations in the correlation functions, see Sec. 6.4 which occur on a time-scale Ω_p^{-1} are very fast and can be averaged out when only the long-time dynamics is of interest and short-time effects are not considered. In this limit, the standard driven and Ohmically damped spin-boson model [8, 9] is recovered. In the regime of weak damping $\alpha \ll 1$, the stationary population difference P_∞ has been determined within the assumption of large driving frequencies ($\Omega \gg W, \nu$ and Ω much larger than the decay rate) upon using analytic real-time path integral methods in Ref. [26]. In this Section, we use this high-frequency approximation of Ref. [26] as a starting point, and derive a closed simple analytic expression for the peak shape of the "common" multi-photon resonance. Most importantly, we find the scaling of the width of the n-photon resonance as the n-th Bessel function $J_n(s/\Omega)$. This scaling behavior has been observed experimentally in superconducting flux qubit devices [16].

The central issue in finding a closed analytic expression for P_∞ is to find the roots ϑ_n of the pole equation [26]

$$\prod_{n=-\infty}^{+\infty} \left(F_n^2 - \vartheta^2\right) + \sum_{n=0}^{+\infty} W_n^2 \prod_{m=-\infty, m\neq n}^{+\infty} \left(F_m^2 - \vartheta^2\right) = 0\,. \tag{6.49}$$

Here, $F_n = F_0 - n\Omega$ is the photon-induced bias and $W_n = |J_n(s/\Omega)|W$ is the field-dressed tunneling splitting of the TSS, where $J_n(x)$ is the n-th ordinary Bessel function. Considering the n-photon resonance, we numerically find that, up to extremely high numerical precision, the roots of Eq. (6.49) are given by

$$\begin{aligned} \vartheta_0 &= \sqrt{F_0^2 + W_0^2}\,, \\ \vartheta_{n\neq 0} &= \sqrt{F_n^2 + W_n^2}\,, \\ \vartheta_{k\neq n,0} &= F_k\,. \end{aligned} \tag{6.50}$$

Plugging Eqs. (6.50) in the expressions for P_∞ given in Ref. [26], see Eqs. (6) and (7) therein, we find the closed expression for the lineshape of the n-photon resonance to be

$$P_\infty^{(n)}(F_0) = \frac{F_0 F_n^2 W_0^2 (F_0^2 + W_0^2 - F_n^2)\frac{J_{\rm Ohm}(\vartheta_0)}{\vartheta_0} + F_0^2 |F_n| W_n^2 (F_n^2 + W_n^2 - F_0^2)\frac{J_{\rm Ohm}(\vartheta_n)}{\vartheta_n}}{Z_{0n} + Z_{n0}} \tag{6.51}$$

$$Z_{ij} = W_i^2 F_j^2 (F_i^2 + W_i^2 - F_j^2) J_{\rm Ohm}(\vartheta_i) \coth \frac{\hbar \vartheta_i}{2k_B T}. \tag{6.52}$$

This result can be simplified upon observing that the second term in the numerator is small if the driving is not too large, since then $W_n^2 \ll W_0^2$. Moreover, we are interested in the regime $F_0 \gg W$ which is the saturation regime implying that $\nu \approx F_0$ and in low temperatures. Then, away from the resonance point at $n\Omega \approx F_0$, the second term in the denominator in Eq. (6.52) can be neglected and one recovers the standard result, if one uses that $W_0 \approx W$ which is fulfilled for weak driving. It reads

$$P_\infty^{(n)}(F_0) = \frac{F_0}{\sqrt{F_0^2 + W^2}} \tanh \frac{\sqrt{F_0^2 + W^2}}{2k_B T}, \tag{6.53}$$

which gives the correct result away from any n-photon resonance. For the case at the n-photon resonance at $n\Omega \approx F_0$, one finds a Lorentzian line shape, i.e.,

$$P_\infty^{(n)}(F_0) = \frac{W_0^2 (F_0 - n\Omega)^2}{W_0^2 (F_0 - n\Omega)^2 + 2F_0^2 W_n^2 k_B T/\hbar}, \tag{6.54}$$

where we have expanded the second coth term in the denominator (see Eq. (6.52)) up to lowest order in the argument, which is appropriate since ϑ_n is small at resonance. The linewidth of the Lorentzian peak can be calculated as the full width at half maximum (FWHM)

$$\Delta F^{(n)} = 2\sqrt{2n\Omega \left(\frac{W_n}{W_0}\right)^2 \frac{k_B T}{\hbar} + \left(\frac{W_n}{W_0}\right)^4 \left(\frac{k_B T}{\hbar}\right)^2}. \tag{6.55}$$

Note that this result obtained from the high-frequency approximation is independent of the damping constant. Moreover, the leading term is the first term under the square root in Eq. (6.55). Note furthermore that for the case of infinitesimal driving, the FWHM is not correctly reproduced by Eq. (6.55) since it would approach zero. However, as it is known from NMR

within a treatment in terms of the Bloch equation, in this case, the FWHM is dominated by the dephasing [17], i.e.,

$$\Delta F^{(1)}_{\mathrm{Bloch}} = 2\sqrt{\Gamma_\phi^2 + \Omega_R^2 \Gamma_\phi/\Gamma_R}\,, \tag{6.56}$$

where $\Gamma_R = \pi\alpha \coth(\hbar\nu/2k_BT)W^2/\nu$ is the relaxation rate and $\Gamma_\phi = \Gamma_R/2 + 2\pi\alpha(F_0^2/\nu^2)k_BT/\hbar$ [8]. Both rates are of first order in the damping strength α. Moreover, Ω_R is the (single-photon) Rabi frequency. Hence, we have to include the dephasing rate Γ_ϕ^2 in Eq. (6.54), since it cannot be reproduced by our weak-coupling approach which is only of first order in α. This finally yields in leading order in the driving strength

$$\Delta F^{(n)} = 2\sqrt{\Gamma_\phi^2 + \left(\frac{W_n}{W_0}\right)^2 2n\Omega\frac{k_BT}{\hbar}}\,. \tag{6.57}$$

As follows from Eq. (6.57), the FWHM of the n-photon resonance scales with the n-th ordinary Bessel function, i.e., $\Delta F^{(n)} \sim J_n(s/\Omega)$ as also confirmed by experiments [16].

6.6 Conclusions

In conclusion we have investigated the problem of a quantum mechanical driven two-state system being coupled to a structured environment which has a localized mode at a frequency Ω_p but behaves Ohmically at low frequencies. We have studied two complementary parameter regimes of weak and strong coupling to the environment. The interplay of the driving and the localized mode gives additional features like resonant peaks/dips in the asymptotic averaged population difference P_∞. We have calculated analytically the lineshape of the resonances in various parameter regimes and have obtained simple closed expressions for the particular example of the first blue sideband. We also include the discussion of how the results are generalized for any sideband. Moreover, we have elaborated the limit when the localized mode acts as a high-frequency cut-off. Then, the full width at half maximum of the n-photon resonance has been shown to scale with the n-th ordinary Bessel function.

Our model finds as well applications in the field of cavity quantum electrodynamics (CQED) with solid state structures [27]. Most interestingly,

the strong coupling limit of CQED could be reached in superconducting electrical circuits, with perspective applications ahead.

Finally, we note that a related experiment has been reported recently by Wallraff *et al.* [28]. There, a qubit was realized in the form of a Cooper pair box which couples to a single mode of a cavity which is damped. The properties of the TSS-HO were probed spectroscopically by measuring the transmission of the resonator. In other words, a *driven* HO was considered while the TSS was kept static. In contrast to that system, here, the TSS was time-dependent while the HO is treated as static.

6.A Symmetry properties for the dissipative rates for the first blue sideband

In order to evaluate the stationary averaged population difference P_∞, the rate coefficients $L_{\alpha\beta,\alpha'\beta'}$ have to be determined explicitly. For the example of the resonance at $\nu \approx \Omega - \Omega_p$ (first blue sideband) considered in this work, we find that the rate coefficients fulfill the symmetry relations

$$
\begin{aligned}
L_{11,22} &= L_{22,11} = L_{33,44} = L_{44,33} = 0, & L_{11,11} &= -(L_{33,11} + L_{44,11}),\\
L_{22,22} &= -(L_{33,22} + L_{44,22}), & L_{33,33} &= -(L_{11,33} + L_{44,33}),\\
L_{44,44} &= -(L_{11,44} + L_{22,44}), & L_{12,12} &= (L_{22,22} + L_{11,11})/2,\\
L_{11,33} &= L_{44,22}, \quad L_{22,33} = L_{44,11}, & L_{33,22} &= L_{11,44},\\
L_{33,11} &= L_{22,44}, \quad L_{22,21} = L_{21,11}, & L_{11,21} &= L_{21,22},\\
L_{44,21} &= -L_{21,33}, \quad L_{33,21} = -L_{21,44}, & L_{22,12} &= L_{22,21},\\
L_{11,12} &= L_{11,21}, \quad L_{44,12} = L_{44,21}, & L_{33,21} &= L_{33,12},\\
L_{12,21} &= 0.
\end{aligned}
\tag{6.58}
$$

As a consequence, there are eight independent rates given by

$$
\begin{aligned}
L_{44,22} &= 2L_{\rm osc}(\varepsilon_{4,2,-1})\cos^2\left(\tfrac{\theta}{2}\right) + 2L_{\rm q}(\varepsilon_{4,2,0})\sin^2\left(\tfrac{\theta}{2}\right) \\
&\quad -L_{\rm q,osc}(\varepsilon_{4,2,-1})\sin\theta\,, \\
L_{22,44} &= 2L_{\rm osc}(\varepsilon_{2,4,1})\cos^2\left(\tfrac{\theta}{2}\right) + 2L_{\rm q}(\varepsilon_{2,4,0})\sin^2\left(\tfrac{\theta}{2}\right) \\
&\quad -L_{\rm q,osc}(\varepsilon_{2,4,1})\sin\theta\,, \\
L_{44,11} &= 2L_{\rm osc}(\varepsilon_{4,1,-1})\sin^2\left(\tfrac{\theta}{2}\right) + 2L_{\rm q}(\varepsilon_{4,1,0})\cos^2\left(\tfrac{\theta}{2}\right) \\
&\quad +L_{\rm q,osc}(\varepsilon_{4,1,-1})\sin\theta\,, \\
L_{11,44} &= 2L_{\rm osc}(\varepsilon_{1,4,1})\sin^2\left(\tfrac{\theta}{2}\right) + 2L_{\rm q}(\varepsilon_{1,4,0})\cos^2\left(\tfrac{\theta}{2}\right) \\
&\quad +L_{\rm q,osc}(\varepsilon_{1,4,1})\sin\theta\,, \\
L_{21,22} &= \tfrac{1}{2}\left(L_{\rm osc}(\varepsilon_{3,2,0}) - L_{\rm q}(\varepsilon_{3,2,-1}) - L_{\rm osc}(\varepsilon_{4,2,-1}) + L_{\rm q}(\varepsilon_{4,2,0})\right)\sin\theta \\
&\quad +\tfrac{1}{2}(L_{\rm q,osc}(\varepsilon_{3,2,0}) - L_{\rm q,osc}(\varepsilon_{4,2,-1}))\cos\theta\,, \\
L_{21,11} &= \tfrac{1}{2}\left(L_{\rm osc}(\varepsilon_{3,1,0}) - L_{\rm q}(\varepsilon_{3,1,-1}) - L_{\rm osc}(\varepsilon_{4,1,-1}) + L_{\rm q}(\varepsilon_{4,1,0})\right)\sin\theta \\
&\quad +\tfrac{1}{2}(L_{\rm q,osc}(\varepsilon_{3,1,0}) - L_{\rm q,osc}(\varepsilon_{4,1,-1}))\cos\theta\,, \\
L_{21,44} &= \tfrac{1}{2}\left(L_{\rm osc}(\varepsilon_{1,4,1}) + L_{\rm osc}(\varepsilon_{2,4,1}) - L_{\rm q}(\varepsilon_{1,4,0}) - L_{\rm q}(\varepsilon_{2,4,0})\right)\sin\theta \\
&\quad +\tfrac{1}{2}(L_{\rm q,osc}(\varepsilon_{1,4,1}) + L_{\rm q,osc}(\varepsilon_{2,4,1}))\cos\theta\,, \\
L_{21,33} &= \tfrac{1}{2}\left(L_{\rm q}(\varepsilon_{1,3,1}) + L_{\rm q}(\varepsilon_{2,3,1}) - L_{\rm osc}(\varepsilon_{1,3,0}) - L_{\rm osc}(\varepsilon_{2,3,0})\right)\sin\theta \\
&\quad -\tfrac{1}{2}(L_{\rm q,osc}(\varepsilon_{1,3,0}) + L_{\rm q,osc}(\varepsilon_{2,3,0}))\cos\theta\,,
\end{aligned}
$$

with

$$
\begin{aligned}
L_{\rm q}(\varepsilon_{klm}) &= \langle e,1,0|e^{iS}Xe^{-iS}|g,1,0\rangle^2 N(\varepsilon_{klm}) \\
&= \langle e,0,0|e^{iS}Xe^{-iS}|g,0,0\rangle^2 N(\varepsilon_{klm}) \\
&= \frac{4g^2W^2\Omega_p^2 N(\varepsilon_{klm})}{\nu^2(\nu^2-\Omega_p^2)^2}\,, \\
L_{\rm osc}(\varepsilon_{klm}) &= \langle g,1,0|e^{iS}Xe^{-iS}|g,0,0\rangle^2 N(\varepsilon_{klm}) \\
&= \langle e,1,0|e^{iS}Xe^{-iS}|e,0,0\rangle^2 N(\varepsilon_{klm}) \\
&= \left(\frac{4g^2(W^2(\nu^2-2\Omega_p^2)-(\nu^2-\Omega_p^2)^2)}{\Omega_p^2(\nu^2-\Omega_p^2)^2}+1\right)N(\varepsilon_{klm})\,, \\
\frac{L_{\rm q,osc}(\varepsilon_{klm})}{N(\varepsilon_{klm})} &= -2\langle e,1,-1|e^{iS}Xe^{-iS}|g,1,0\rangle\langle g,1,0|e^{iS}Xe^{-iS}|g,0,0\rangle \\
&= 2\langle g,0,1|e^{iS}Xe^{-iS}|e,0,0\rangle\langle e,0,0|e^{iS}Xe^{-iS}|e,1,0\rangle \\
&= \frac{WF_0gs((\Omega+\Omega_p)^2+2\Omega_p^2+\nu(-\Omega+\Omega_p))}{2\nu(\nu-\Omega)\Omega(\nu-\Omega-\Omega_p)\Omega_p(\nu+\Omega_p)}\,, \\
N(\varepsilon_{klm}) &= N(\varepsilon_k-\varepsilon_l+m\Omega)\,. \qquad (6.59)
\end{aligned}
$$

Note that $L_{\rm osc}$ is the rate containing the zeroth order term in g and s. It is related to the transition between two states differing by one oscillator

quantum. This decay is of zeroth order (hence fast) because the oscillator is coupled directly to the environment. Moreover, L_{q} gives the rate for transitions between the excited and ground state of the TSS with the HO remaining in the same state, and $L_{\mathrm{q,osc}}$ is related to the transition where both the qubit and the oscillator exchange energy with the environment. Note that this transition is induced by the driving and involves one photon.

6.B Coefficients for the kernels $k_0^{\pm}(0)$

In Sec. 6.4, we have introduced an expansion of the oscillating functions given in Eq. (6.41). In this appendix we summarize the corresponding coefficients for completeness.

For the expansion of $\cos[Q''(t)]$, we find

$$\begin{aligned} D_{2m+1} &= (-1)^m \sin(A_1) J_{2m+1}(A) \cos[(2m+1)X], \\ D_{2m} &= (-1)^m \cos(A_1) J_{2m}(A) \cos(2mX), \\ E_{2m+1} &= (-1)^m \sin(A_1) J_{2m+1}(A) \sin[(2m+1)X], \\ E_{2m} &= (-1)^m \cos(A_1) J_{2m}(A) \sin(2mX), \end{aligned} \tag{6.60}$$

where we have introduced

$$\begin{aligned} A &= e^{-\Gamma t}\sqrt{A_1^2 + A_2^2}, \\ \sin X &= A_2/\sqrt{A_1^2 + A_2^2}. \end{aligned} \tag{6.61}$$

In the same way, the expansion of $\sin[Q''(t)]$ gives

$$\begin{aligned} F_{2m+1} &= (-1)^{m+1} \cos(A_1) J_{2m+1}(A) \cos[(2m+1)X], \\ F_{2m} &= (-1)^m \sin(A_1) J_{2m}(A) \cos[2mX], \\ G_{2m+1} &= (-1)^{m+1} \cos(A_1) J_{2m+1}(A) \sin([2m+1)X], \\ G_{2m} &= (-1)^m \sin(A_1) J_{2m}(A) \sin[2mX]. \end{aligned} \tag{6.62}$$

Finally, we find for the coefficients of $\exp[Q(t) - Q_1(t)]$

$$\begin{aligned} H_m &= I_m(Y) \cos(mV), \\ K_m &= I_m(Y) \sin(mV), \end{aligned} \tag{6.63}$$

where we have introduced

$$\begin{aligned} Y &= e^{-\Gamma t}\sqrt{Y_1^2 + Y_2^2}\,, \\ \tan V &= \frac{Y_2}{Y_1}\,. \end{aligned} \tag{6.64}$$

Here, I_m is the modified Bessel function of the first kind of order m.

Bibliography

[1] Y. Nakamura, Yu. A. Pashkin, and J. S. Tsai, Nature **398**, 786 (1999).

[2] J. M. Martinis, S. Nam, J. Aumentado, and C. Urbina, Phys. Rev. Lett. **89**, 117901 (2002).

[3] Yu. A. Pashkin, T. Yamamoto, O. Astafiev, Y. Nakamura, D. V. Averin, and J. S. Tsai, Nature **421**, 823 (2003).

[4] D. Vion, A. Aassime, A. Cottet, P. Joyez, H. Pothier, C. Urbina, D. Esteve, and M. H. Devoret, Science **296**, 886 (2002).

[5] I. Chiorescu, Y. Nakamura, C. J. P. M. Harmans, and J. E. Mooij, Science **299**, 1869 (2003).

[6] I. Chiorescu, P. Bertet, K. Semba, Y. Nakamura, C. J. P. M. Harmans, and J. E. Mooij, Nature **431**, 159 (2004).

[7] C. Cohen-Tannoudji, J. Dupont-Roc and G. Grynberg, *Atom-Photon Interactions* (Wiley, New York, 1992).

[8] U. Weiss, *Quantum Dissipative Systems* (World Scientific, Singapore, 1999).

[9] M. Grifoni and P. Hänggi, Phys. Rep. **304**, 229 (1998).

[10] L. Tian, S. Lloyd, and T.P. Orlando, Phys. Rev. B **65**, 144516 (2002).

[11] M. Thorwart, L. Hartmann, I. Goychuk, and P. Hänggi, J. Mod. Opt. **47**, 2905 (2000).

[12] A. Yu. Smirnov, Phys. Rev. B **67**, 155104 (2003).

[13] M. Thorwart, E. Paladino and M. Grifoni, Chem. Phys. **296**, 333 (2004).

[14] F. K. Wilhelm, S. Kleff and J. von Delft, Chem. Phys. **296**, 345 (2004).

[15] S. Kleff, S. Kehrein, and J. von Delft, Phys. Rev. B **70**, 014516 (2004).

[16] S. Saito, M. Thorwart, H. Tanaka, M. Ueda, H. Nakano, K. Semba, and H. Takayanagi, Phys. Rev. Lett. **93**, 037001 (2004).

[17] M. C. Goorden and F. K. Wilhelm, Phys. Rev. B **68**, 012508 (2003).

[18] A. Garg, J. N. Onuchic and V. Ambegaokar, J. Chem. Phys. **83**, 4491 (1985).

[19] R. Blümel, R. Graham, L. Sirko, U. Smilansky, H. Walther, and K. Yamada, Phys. Rev. Lett. **62**, 341 (1989).

[20] S. Kohler, T. Dittrich, and P. Hänggi, Phys. Rev. E **55**, 300 (1997).

[21] J.H. Shirley, Phys. Rev. **138**, B979 (1965).

[22] I. Shavit and L. T. Redmon, J. Chem. Phys. **73**, 5711 (1980).

[23] N. Makri and D.E. Makarov, J. Chem. Phys. **102**, 4600 (1995).

[24] M. Thorwart, P. Reimann, P. Jung, and R. F. Fox, Chem. Phys. **235**, 61 (1998).

[25] M. Thorwart, P. Reimann, and P. Hänggi, Phys. Rev. E **62**, 5808 (2000).

[26] L. Hartmann, I. Goychuk, M. Grifoni, and P. Hänggi, Phys. Rev. E **61**, R4687 (2000).

[27] S. M. Girvin, R.-S. Huang, A. Blais, A. Wallraff, and R. J. Schoelkopf, in *Proceedings of Les Houches Summer School*, Session LXXIX, Quantum Entanglement and Information Processing (2003); see also cond-mat/0310670.

[28] A. Wallraff, D. I. Schuster, A. Blais, L. Frunzio, R.-S. Huang, J. Majer, S. Kumar, S. M. Girvin, and R. J. Schoelkopf, Nature **431**, 162 (2004).

Samenvatting

Andreevreflectie vindt plaats aan het grensvlak tussen een normaal metaal en een supergeleider. Bij dit bijzondere reflectiemechanisme wordt een elektron gereflecteerd als een gat. Wanneer het elektron op het Ferminiveau is, keert het gat precies terug langs het pad van het elektron. Andreevreflectie speelt een belangrijke rol in een Andreevbiljart. Een Andreevbiljart bestaat uit een zogenaamde "quantum dot" die via een quantumpuntcontact gekoppeld is aan een supergeleider. De quantum dot zelf is te vergelijken met een biljart, gemaakt in een tweedimensionaal elektronengas. Aangezien er in de quantum dot geen verontreinigingen zijn, vindt alle reflectie plaats aan de wanden. Wij beschouwen quantum dots met een zodanige vorm dat de klassieke beweging van een elektron (of gat) in de dot chaotisch is.

De beweging van elektronen en gaten in een Andreevbiljart wordt beschreven door de quantummechanica. Volgens de stelling van Ehrenfest is de beweging aanvankelijk langs een klassiek pad. Naarmate de tijd vordert zijn de positie en de snelheid steeds minder goed gedefinieerd. Na een bepaalde tijd is de onzekerheid in de positie van het elektron of gat even groot als de afmeting van het Andreevbiljart. Dit is de Ehrenfesttijd τ_E. De Ehrenfesttijd karakteriseert de overgang van klassieke mechanica naar quantummechanica.

Als de Ehrenfesttijd veel langer is dan de gemiddelde tijd τ_D tussen Andreevreflecties, is een beschrijving in termen van klassieke paden geoorloofd. Andreevreflectie maakt alle paden (bij benadering) periodiek, dus quantisatie volgens de Bohr-Sommerfeld methode is mogelijk. In de tegenovergestelde limiet $\tau_E \ll \tau_D$ geeft toevalsmatrixtheorie een goede beschrijving. Terwijl toevalsmatrixtheorie voorspelt dat de toestandsdichtheid in een chaotisch Andreevbiljart identiek nul wordt voor lage ener-

gieën (d.w.z. er ontstaat een "gat"), geeft quantisatie van periodieke paden slechts een geleidelijke afname van de toestandsdichtheid zonder een echt "gat". In dit proefschrift wordt een nieuwe theorie gegeven die beide eerdere theorieën met elkaar verbindt.

Het idee achter onze theorie is eenvoudig. We quantiseren alle klassieke paden met een verblijftijd T in de quantum dot, die korter is dan de Ehrenfesttijd door middel van de Bohr-Sommerfeld methode. Het overige gedeelte van de faseruimte wordt gequantiseerd via toevalsmatrixtheorie met effectieve parameters. De theorie wordt uitgewerkt in het tweede tot en met het vijfde hoofdstuk.

Hoofdstuk twee vormt de basis voor de rest van het proefschrift. Voor een beschrijving van de paden met $T < \tau_E$ is een precieze kennis van de klassieke beweging vereist. We beschouwen de beweging van een elektron met een energie E boven het Ferminiveau. Het Andreev gereflecteerde gat keert niet precies terug langs het pad van het elektron, daarom is het pad niet precies gesloten maar drijft af in de faseruimte. We hebben gevonden dat de tijd T tussen opeenvolgende Andreevreflecties een adiabatisch behouden grootheid is. Met deze kennis is het mogelijk een uitdrukking te vinden voor de energieniveaus behorend bij de korte paden. Onze quasiklassieke theorie is niet toepasbaar voor lange paden met $T > \tau_E$. We nemen aan dat het gedeelte van de faseruimte met lange paden kan worden beschreven door effectieve toevalsmatrixtheorie.

Een computersimulatie is een goede methode om onze theorie te testen. Een zeer effectief model is de "Andreev kicked rotator", dat een stroboscopische beschrijving geeft van een Andreevbiljart. In het derde hoofdstuk gebruiken we dit stroboscopisch model om de fluctuaties van het laagste energie niveau te bepalen. De fluctuaties ontstaan omdat we de positie van de supergeleider veranderen. We vinden dat de amplitude van de fluctuaties groeit met toenemende verhouding τ_E/τ_D. Effectieve toevalsmatrixtheorie geeft een goede beschrijving van de fluctuaties.

In hoofdstuk vier breiden we onze quasiklassieke theorie uit door de toevoeging van een zwak magneetveld, dat loodrecht op het Andreevbiljart staat. De adiabatisch behouden grootheid van de klassieke beweging is nu niet meer de tijd T maar heeft ook een elektromagnetische component. We vinden dat een magneetveld het laagste adiabatische niveau verlaagt met een hoeveelheid die onafhankelijk is van de Ehrenfesttijd. Het magneetveld veroorzaakt ook een afname van het laagste niveau van de effectieve

toevalsmatrixtheorie. Het gat in de toestandsdichtheid verdwijnt bij een kritisch magneetveld dat afneemt met toenemende Ehrenfesttijd. Onze bevindingen komen goed overeen met computersimulaties.

In het vijfde hoofdstuk laten we zien dat onze theorie ook kan worden toegepast op een quantum dot die niet gekoppeld is aan een supergeleider, maar aan twee elektronenreservoirs. Door dit systeem kan een stroom lopen. Omdat de stroom bestaat uit elektronen met een discrete lading, is er zelfs bij zeer lage temperaturen ruis. Deze zogenaamde hagelruis neemt af met toenemende Ehrenfesttijd. Onze theorie voorspelt deze afname en is in staat deze te relateren aan de specifieke klassieke eigenschappen van een bepaald systeem.

Het zesde hoofdstuk behandelt een geheel ander systeem, de Josephson-junctie-qubit. De qubit bestaat uit een supergeleidende ring met drie Josephsonjuncties en kan in een superpositie zijn van een rechtsomdraaiende en linksomdraaiende stroom. De qubit wordt gemeten door een quantummechanisch meetinstrument, dat extra resonanties kan veroorzaken. Dit is onlangs gemeten en wij geven een kwantitatieve beschrijving van het experiment.

List of publications

- *Optical imaging of contrast agent microbubbles in an ultrasound field with a 100-MHz camera*, N. de Jong, P. J. A. Frinking, A. Bouakaz, M. C. Goorden, T. Schuurmans, J. P. Xu, and F. Mastik, Ultrasound in Medicine and Biology **26**, 487–492 (2000).

- *Adiabatic quantization of Andreev quantum billiard levels*, P. G. Silvestrov, M. C. Goorden, and C. W. J. Beenakker, Physical Review Letters **90**, 116801 (2003). [Chapter 2]

- *Noiseless scattering states in a chaotic cavity*, P. G. Silvestrov, M. C. Goorden, and C. W. J. Beenakker, Physical Review B **67**, 241301(R) (2003). [Chapter 5]

- *Quasiclassical fluctuations of the superconductor proximity gap in a chaotic system*, M. C. Goorden, Ph. Jacquod, and C. W. J. Beenakker, Physical Review B **68**, 220501(R) (2003). [Chapter 3]

- *Theoretical analysis of continuously driven dissipative solid-state qubits*, M. C. Goorden and F. K. Wilhelm, Physical Review B **68**, 012508 (2003).

- *Entanglement spectroscopy of a driven solid-state qubit and its detector*, M. C. Goorden, M. Thorwart, and M. Grifoni, Physical Review Letters **93**, 267005 (2004).

- *Spectroscopy of a driven solid-state qubit coupled to a structured environment*, M. C. Goorden, M. Thorwart, and M. Grifoni, European Physical Journal B **45**, 405 (2005). [Chapter 6]

- *Quantum-to-classical crossover for Andreev billiards in a magnetic field*, M. C. Goorden, Ph. Jacquod, and C. W. J. Beenakker, to be published in Physical Review B. [Chapter 4]

Curriculum Vitæ

Ik ben geboren op 26 december 1976 te Sittard. Ik bezocht daar de Basisschool “Onder de Kastanje”. Ik genoot middelbaar onderwijs aan het Gertrudislyceum in Roosendaal, waar ik in 1995 mijn VWO diploma behaalde. In datzelfde jaar begon ik met mijn studie Technische Natuurkunde aan de TU Delft. In 2000 bracht ik een half jaar door bij NTT Basic Research Laboratories in Japan in de groep van Prof. dr. H. Takayanagi, waar ik experimenteel werk deed op het gebied van Josephsonjunctie-qubits. In 2002 studeerde ik af in de groep van Prof. dr. ir. J. E. Mooij, onder directe begeleiding van Dr. F. K. Wilhelm. De titel van mijn afstudeerscriptie is “Theory of Josephson persistent-current qubits with driving and dissipation”.

In april 2002 trad ik in dienst van de Stichting voor Fundamenteel Onderzoek der Materie als Onderzoeker in Opleiding. Ik deed mijn promotieonderzoek aan het Instituut–Lorentz van het Leids Instituut voor Onderzoek in de Natuurkunde aan de Universiteit Leiden in de groep van Prof. dr. C. W. J. Beenakker. De belangrijkste resultaten worden beschreven in dit proefschrift. Tijdens mijn promotie heb ik geassisteerd bij de colleges Statistische Fysica I en Statistische en Thermische Fysica II. Tijdens mijn aanstelling presenteerde ik mijn werk in Mallorca, Genève, Regensburg en Delft. Daarnaast woonde ik conferenties bij in Bad Honnef en Delft en bezocht ik een zomerschool in Wittenberg.

Per september 2005 zal ik werkzaam zijn als postdoc in de groep van Prof. dr. M. Büttiker aan de universiteit van Genève.

Dankwoord

Ik kijk met veel plezier terug op mijn tijd aan het Instituut–Lorentz. Ik had het genoegen samen te werken met veel verschillende mensen, zowel binnen als buiten het instituut. Peter het werk in mijn eerste jaar met jou legde de basis voor mijn proefschrift, Philippe en Milena: bedankt voor de gastvrijheid in Genève en Regensburg. Ook buiten het werk was de atmosfeer op het instituut erg goed, ik kijk met veel plezier terug op de gezamenlijke koffiepauzes en lunches en de jaarlijkse instituutsuitjes.

Daarnaast wil ik familie en vrienden bedanken voor alle steun en afleiding de afgelopen jaren. Noor en Eelke, bedankt dat jullie mijn paranymphen willen zijn. En tot slot, Herman ik jou ook ...

Stellingen

behorende bij het proefschrift

On Superconductivity in nanostructures:
Andreev billiards and Josephson junction qubits

1. De tijd tussen opeenvolgende Andreevreflecties is een adiabatische constante van de beweging. Hoofdstuk 2

2. Het aloude resultaat dat het energiegat van een Josephsonjunctie gegeven wordt door de constante van Planck maal een klassieke grootheid gaat niet op voor een Andreevbiljart. Hoofdstuk 2

3. Elektronen die korter dan de Ehrenfesttijd in een quantum dot verblijven zijn ruisloos. Hoofdstuk 5

4. Het theoretische spin-boson model vindt een realistische toepassing in de beschrijving van een supergeleidende ring die gekoppeld is aan een gevoelig meetinstrument. Hoofdstuk 6

5. In het stroboscopische model voor een quantum dot (de "open kicked rotator") kan spin-baan koppeling worden ingevoerd, mits de opening in de faseruimte 90° wordt gedraaid.

6. Indien een verstrengeld elektron-gat paar vervalt in een paar fotonen, dan zullen de fotonen zelf niet meer verstrengeld zijn, zelfs indien spin-baan koppeling een correlatie tussen de elektronspin en de fotonpolarisatie veroorzaakt.

7. De verschuiving van de resonantiepiek van een spin in een lineair oscillerend magneetveld is in het algemeen groter dan de Bloch-Siegert verschuiving.

   F. Bloch and A. Siegert, Phys. Rev. **57**, *522 (1940).*

8. De gangbare opvatting, dat grootschalige destillatieapparatuur tijdsonafhankelijk moet opereren, dient herzien te worden: cyclisch variërende condities kunnen het nadelige effect van terugmenging op de drijvende kracht van stoftransport beperken.

9. Het verdient aanbeveling bij het schoolvak Algemene Natuurwetenschappen een populair-wetenschappelijke boekenlijst te verplichten.

Marlies Goorden
15 september 2005